12-2021

Design of a 300cm2 PEMFC stack with force and CFD simulation to optimize flow channels, gasket design, and clamping forces.

Robert M. Ench
University of Louisville

Design of a 300cm^2 PEMFC stack with force and CFD simulation to optimize flow channels, gasket design, and clamping forces

By Robert Michael Ench

A Thesis
Submitted to the Faculty of the
University of Louisville
J. B. Speed School of Engineering
as Partial Fulfillment of the
Requirements for the Professional
Degree

MASTER OF ENGINEERING

Department of Mechanical Engineering

December 2021

Design of a 300cm^2 PEMFC stack with force and CFD simulation to optimize flow channels, gasket design, and clamping forces

Submitted by: 

Robert Michael Ench

A Thesis Approved On

1/5/2022

(Date)

by the Following Reading and Examination Committee:

Sam D. Park, Thesis Director

Dr. Ellen Brehob

Dr. Young Hoon Kim

DEDICATION

This thesis is dedicated to my father John Robert Ench Jr that passed away on my last year of my bachelor's degree. He was supportive of my educational plan as he was a graduate of the University of Louisville Speed School of Engineering.

ACKNOWLEDGEMENTS

I would like to thank Dr. Sam Park for his guidance and support of this thesis. I also acknowledge that my understanding of hydrogen fuel cells comes from my 2 years working with Dr. Sam Park on other projects. I also want to thank Dr. Young Hoon Kim and Dr. Ellen Brehob for being on my committee and for the knowledge I obtained in their classes.

I would also like to thank my wife Julia and my daughter Lily for their patience and support as I worked on my degree and this thesis.

ABSTRACT

Design of a 300cm^2 PEMFC Stack with Force and CFD simulation to optimize flow channels, gasket design, and clamping forces.

Robert Michael Ench

April 10, 2021

Proton exchange membrane fuel cells are important to the future of green energy as hydrogen can be made with green technologies and store energy for later use. Fuel cells can efficiently convert the hydrogen to electricity as needed. This study uses Solidworks simulation to make design improvements to the fuel cell before the prototype build stage of testing; this saves money and time by reducing the prototype builds needed.

In this study, a multi-channel serpentine design with two outlets versus a single outlet is evaluated using CFD to investigate pressure drop. Lower pressure drops are desirable as less energy input is required to operate the fuel cell. A problem with the clamping of fuel cell end plates is that the forces are not evenly spread throughout the cell. To improve the clamping force problem, a two-piece end plate with embossments is designed and forces simulated. In the FEA, the embossments provided a more uniform force distribution.

The findings show that the two-outlet bi-polar plate greatly reduces the pressure drop, which at same inlet pressure of 5 psi increases the mass flowrate by 54% . The

analysis of the endplates with embossments shows an improvement in the uniformity of the forces applied to the fuel cell. This is visible by the stress contour plots of each design, which shows that the forces move from the edges of the cell to the inner area of the cell.

This study demonstrates that Solidworks can be used to evaluate a PEMFC and that the design changes used in this study have promising possibilities in future PEMFC designs.

TABLE OF CONTENTS

DEDICATION iv
ACKNOWLEDGEMENTS v
ABSTRACT vi
LIST OF FIGURES x
LIST OF TABLES xiii
ABBREVIATIONS xiv
CHAPTER 1: INTRODUCTION 1
CHAPTER 2: OBJECTIVE AND INTELLECTUAL MERIT 6
CHAPTER 3: BI-POLAR PLATE REVIEW 8
3.1 Background 8
3.2 Review 9
3.3 Relation to this project 11
3.4 PEMFC Design Overview 12
CHAPTER 4: CLAMPING FORCE 15
4.1 Background 15
4.2 Review 16
4.3 Relation to this project 17
CHAPTER 5: PEMFC DESIGN 18
5.1 Bipolar Plate Design 18
5.2 Gasket Design 22
5.3 Clamping Bracket Design 29
Chapter 6: Bi-polar Plate Simulation 31
6.1 Flow Channel Length Simulation 31
6.2 Radius Simulation for Gas Channels 37
6.3 Cooling Channel Simulation 38

CHAPTER 7: Gasket Compression Calculations 47
7.1 Calculating Forces on Gaskets 47
7.2 Material Thickness 53
7.3 Clamping Forces 54
CHAPTER 8: Clamping Bracket Force Simulation 56
8.1 Clamping Bracket Simulation Setup 56
8.2 Embossments in clamping bracket 59
CONCLUSIONS 78
RECOMMENDATIONS 80
REFERENCES 81
APPENDIX 84
A.1 CFD how it works 84
A.2 Part Drawings 88
CURRICULUM VITA 108

LIST OF FIGURES

FIGURES PAGE

Figure 1 The Components of one PEM fuel cell 2
Figure 2 Pin bipolar design (left), Cascade bipolar design (right) 8
Figure 3 Parallel bipolar design (left), Serpentine bipolar design (right) 9
Figure 4 Illustrated PEMFC reaction 12
Figure 5 Parts of a PEMFC Stack 13
Figure 6 The PEMFC Stack inputs and Outputs 14
Figure 7 The forces on the end plate with the curvature 15
Figure 8 A 12 channel serpentine design bipolar plate 19
Figure 9 Dual outlet design 20
Figure 10 Bipolar plate with square bends 21
Figure 11 Bipolar plate with curved channels 21
Figure 12 Cooling channels 22
Figure 13 Cell detail showing gas side gaskets 24
Figure 14 The bipolar plate with gas gasket 25
Figure 15 Bipolar plate with gasket and GDL 26
Figure 16 Bipolar plates with cooling side gasket 28
Figure 17 Cooling side of the bipolar plate with gasket 29
Figure 18 The flow channels open and closed 32
Figure 19 Single in single out bipolar plate flow channels 32
Figure 22 The boundary conditions setup for the single out bi-polar plate 33
Figure 21 The meshed flow channels with a closeup of the mesh 33
Figure 24 CFD iterations vs mass flow rate 34
Figure 23 Open and closed flow channels for dual outlet 35
Figure 24 Boundary conditions of the duel outlet bipolar plate 35
Figure 25 Flow channels of the duel outlet bipolar plate 36
Figure 26 The plot of iterations vs flowrate 36
Figure 27 The added radius locations 38
Figure 28 Cooling simulation assembly 39
Figure 29 Cooling system heat generator locations 40
Figure 30 Boundary conditions for the cooling simulation 40
Figure 31 The cooling channels 41
Figure 32 Simulation with a flowrate of 0.001 kg/s 41
Figure 33 Simulation with a flowrate of 0.0008 kg/s 42
Figure 34 Simulation with a flowrate of 0.0005 kg/s 43
Figure 35 Simulation with a flowrate of 0.0003 kg/s 44
Figure 36 Cooling inlet with radius 45

Figure 37 Cathode Gasket with an area of 25.58 in^2 47
Figure 38 Cathode Gasket with material removed with an area of 15.31 in^2 48
Figure 39 the anode gasket with an area of 26.64 in^2 49
Figure 40 Anode gasket with material removed with an area of 15.59 in^2 50
Figure 41 The end plate gasket with an area of 14.04 in^2 51
Figure 42 the cooling channel gasket with an area of 11.61 in^2 52
Figure 43 GDL with an active area of 50.01 in^2 53
Figure 44. Assembly used for clamping force testing 56
Figure 45 Exploded view of clamping force assembly 57
Figure 46 the fixed geometry of the graphite plate 57
Figure 47 External load setup with 5021 lb_f on each washer 58
Figure 48 The mesh of the clamping force assembly 58
Figure 49 Stress contour plot of the assembly 58
Figure 50 Stress contour plot of the end plate 59
Figure 51 Clamping force assembly with dimple clamping bracket 60
Figure 52 Stress contour plot of assembly with dimple clamping bracket 60
Figure 53 Stress contour plot of the dimple design of the end plate 61
Figure 54 Clamping force assembly with square emboss clamping bracket 61
Figure 55 Stress contour plot of assembly with square clamping bracket 62
Figure 56 Stress contour plot of the square design of the end plate 62
Figure 57 Clamping force assembly with bars element added to the clamping bracket .. 63
Figure 58 Stress contour plot of assembly with bars clamping bracket 63
Figure 59 Stress contour plot of the bars design of the end plate 64
Figure 60 Clamping force assembly with layered square clamping bracket 64
Figure 61 Stress contour plot of assembly with layered square clamping bracket 65
Figure 62 Stress contour plot of the layered square design of the end plate 66
Figure 63 The bottoms of the end plates with the stress forces shown for comparison ... 66
Figure 64 Test assembly of PEMFC stack with end parts and one complete cell 67
Figure 65 Exploded view of the assembly with one cell 67
Figure 66 Mesh for the standard clamping plate. 68
Figure 67 Stress contour plot of the one cell assembly with standard clamping plate 69
Figure 68 Dimple emboss clamping plate assembly with one cell mesh 70
Figure 69 Stress contour plot of the one cell assembly with dimple emboss clamping plate 71
Figure 70 Square emboss plate assembly with one cell mesh 72
Figure 71 Stress contour plot of the one cell assembly with square emboss clamping plate 73
Figure 72 Bars emboss plate assembly with one cell mesh 74

Figure 73 Stress contour plot of the one cell assembly with bars shaped emboss clamping plate 75
Figure 74 Layered squares emboss plate assembly with one cell mesh 75
Figure 75 Stress contour plot of the one cell assembly with layered squares shaped emboss clamping plate 76
Figure 76 Stress contour plots of the one cell assemblies for comparing 77
Figure 77 Cathode bipolar plate drawing 88
Figure 78 Anode bipolar plate drawing 89
Figure 79 Graphite end plate drawing 90
Figure 80 End plate drawing 91
Figure 81 Single out bipolar plate drawing 92
Figure 82 Clamping Bracket drawing 93
Figure 83 Clamping bracket with dimples drawing 94
Figure 84 Clamping bracket with square emboss drawing 95
Figure 85 Clamping bracket with bar style emboss drawing 96
Figure 86 Clamping bracket with layered squares emboss drawing 97
Figure 87 Copper plate drawing 98
Figure 88 Membrane Drawing 99
Figure 89 GDL drawing 100
Figure 90 MEA drawing 101
Figure 91 Cathode side gasket drawing 102
Figure 92 Cathode side gasket with reduced material drawing 103
Figure 93 Anode side gasket drawing 104
Figure 94 Anode side gasket with material removed drawing 105
Figure 95 Water cooling side gasket drawing 106
Figure 96 End plate water gasket drawing 107

LIST OF TABLES

Table 1 Project goals 6
Table 2 List of testing in this project 7
Table 3 Material properties used in Solidworks simulations 31
Table 4 The single out flow channels calculated solutions 34
Table 5 The CFD results for dual outlet bipolar plate 36
Table 6 Single outlet compared to dual outlet bipolar plate 37
Table 7 the CFD results for the dual outlet bi-polar plate with 0.25mm radius added 38
Table 8 Flowrates and maximum water temperature from cooling channel testing. 45
Table 9 Outlet temperature vs channel radius 46
Table 10 Material thickness before and after compression 53
Table 11 List of forces and quantities of each type 54
Table 12 Force total for overall, per end plate, and per bolt 54
Table 13 The number of bolts required based on bolt size 55
Table 14 Calculating the required number of bolts needed 55

ABBREVIATIONS

AFC	Alkaline Fuel Cell
ATM	Atmosphere
CFD	Computational Fluid Dynamics
DMFC	Direct Methanol Fuel Cell
EPDM	Ethylene Propylene Diene Monomer
FEA	Finite Element Analysis
GDL	Gas Diffusion Layer
LBF	Pound-Force
MPa	Megapascal
MEA	Membrane Electrode Assembly
MCFC	Molten Carbonate Fuel Cell
PAFC	Phosphoric Acid Fuel Cell
PEM	Proton Exchange Membrane
PEMFC	Proton Exchange Membrane Fuel Cell
SOFC	Solid Oxide Fuel Cell

CHAPTER 1: INTRODUCTION

The energy demand of the world is always increasing as the availability of fossil fuels are decreasing. This is driving the people of the world to investigate alternative energy sources. In 2019, 17% of the energy used in the United States came from renewable energy, and this percentage is expected to rise to 21% by 2021 (U.S. Energy Information Administration, 2020). The energy sector is rapidly shifting toward renewable energy sources. One promising energy source is hydrogen. Hydrogen can be produced by electricity (electrolysis), thermochemical processes, direct solar water splitting processes, and biological processes (Office of Energy Efficiency & Renewable Energy, 2020). Most of the hydrogen in the United States is produced using steam-methane reforming which has a byproduct of carbon monoxide (Office of Energy Efficiency & Renewable Energy, 2020). Equation 1 demonstrates the steam-methane reforming reaction:

$$CH_4 + H_2O\ (+HEAT) \rightarrow CO + 3H_2 \quad (1)$$

Proton exchange membrane fuel cells are a way to produce electricity from hydrogen. There are many types of fuel cells, but the focus of this work is the proton exchange membrane fuel cell. PEM fuel cells are chosen due to their high-power density, which allows them to be relatively small, and begin generating energy quickly (Electrical Academia, n.d.). The PEM fuel cell converts hydrogen and oxygen to electricity, and details of this process are in Chapter 5. PEMFC are constructed with parts (end plates. membrane electrode assembly, collector plate, bi-polar plates, and gaskets) being compressed together. The end plates allow for the gas fittings to be connected to the

PEMFC stack and for the fasteners to push against the end plates, which causes the clamping force to hold the PEMFC together. The collector plates are used to collect and send off the power that is produced by the PEMFC. Additionally, there are bipolar plates, which can either be the same for the anode and cathode or a different design for each, depending on the design intent. On the back side of the bipolar plate, there will be either an open cooling channel for air-cooled or a closed system channels for water-cooled. There is a Membrane Electrode Assembly (MEA) with Gas Diffusion Layer (GDL) on both sides in the middle of the bipolar plates, as shown if Figure 1

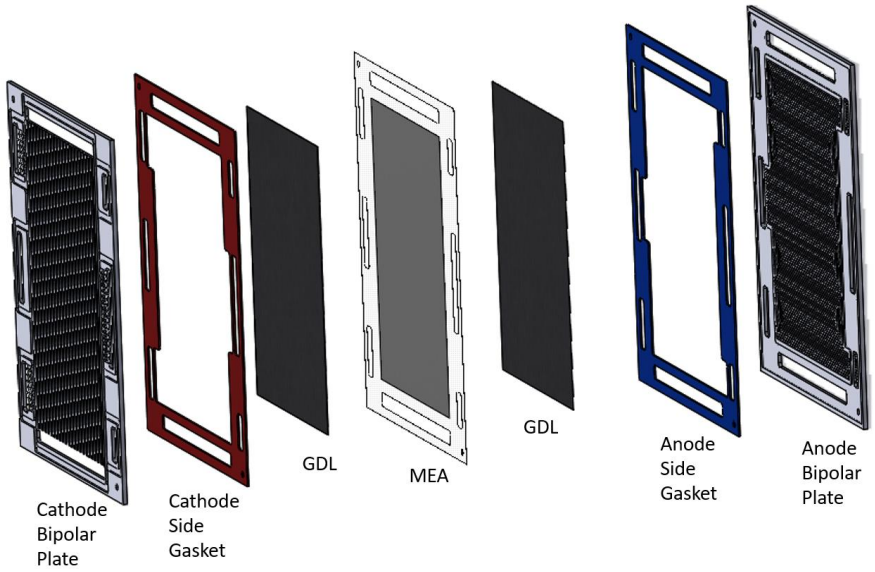

Figure 1 The Components of one PEM fuel cell

The MEA allows the hydrogen ions to pass in order to give the cell its charge and produce power. The GDL allows the gases to pass next to the MEA so that the reaction can happen. The GDL also helps move water away from the MEA and allows the cell to be electrically conductive. The gaskets are also crucial to the functioning of the PEMFC. The gasket seals the gas layers, the MEA, and the cooling channels. The gaskets can make the difference between an efficient PEMFC and a non-working PEMFC by

determining the compression force on the end plates. If the compression force is too high, the GDL will be crushed, reducing its porosity and thereby reducing the gas contact with the MEA. If the force is too small or the gasket is not compressed enough, the GDL could lose its conductivity, reducing the power output of the PEMFC and potentially causing gas and water leakage, which not only reduces efficiency but also poses a hazard. Therefore, the thickness, material, and shore hardness of the gaskets is very important.

Bi-polar plates also consist of flow channels. The flow channels include the cooling channel and the gas channels. The flow patterns effect the efficiency and the pressure drop.

In this project, a 300 cm^2 active area bi-polar plate PEMFC will be designed and simulated for the required gasket and flow channels. The gasket compression and compression force on the PEMFC will be evaluated using Compression Force Deflection charts and mathematics based on the CAD area of each part. The flow channels are evaluated using a Computational Fluid Dynamics (CFD) simulation to look at flow patterns, heat dissipation, and pressure drop.

To better understand why PEMFC was chosen an overview of the different types of fuel cells is reviewed below. The information in this section was attained from the Office of Energy Efficiency & Renewable Energy (Office of Energy Efficency & Renewable Energy, 2021).

PEMFC have a high-power density which allows them to be low weight and size compared to other fuel cells. The PEMFC uses a solid polymer and only needs hydrogen, oxygen, and water to operate. They can operate using pure oxygen from a tank or from the air. They have a low operational temperature around 80ºC. They have a quick starting

time due to the low operational temperature. Some disadvantages to PEMFC is the high cost of platinum catalyst and the purity requirement of the hydrogen gas. PEMFC are primarily used for transportation applications.

Direct methanol fuel cell (DMFC) are power by pure methanol. Methanol has a higher energy density than hydrogen and is easier to transport because it is a liquid. The main drawback to DMFC is the very sluggish anode reaction, which coupled with the inefficient cathode reaction, this gives an overall low performance especially at low temperatures (Keith Scott, 2012).

Alkaline fuel cell (AFC) uses potassium hydroxide in water as electrolyte. Modern AFC use a polymer membrane. AFC are used in space applications do to the high efficiencies above 60% and their poisoning to even low amounts of carbon dioxide (CO_2).

Phosphoric acid fuel cell (PAFC) use liquid phosphoric acid as an electrolyte. PAFC are used for stationary power generation. PAFC are more tolerant to impurities in the fuel. Disadvantages of PAFC very large size and high loading platinum needed for catalyst.

Molten carbonate fuel cell (MCFC) are used for coal-based and natural gas power plants. MCFC run at high temperature, 650ºC. Due to the high temperature lower cost catalyst and the ability convert fuels into hydrogen internally. MCFC disadvantages are the high operating temperature and its short life before decreasing performance.

Solid oxide fuel cell (SOFC) are a high efficiency FC that operates at high temperature of 1000ºC. SOFC has the highest resistance to sulfur allow it to operate on

natural gas, biogas, and gases made from coal. The disadvantage of SOFC is the high operating temperature which cause high cost in materials.

CHAPTER 2: OBJECTIVE AND INTELLECTUAL MERIT

The project is designed to validate the components designs in a PEMFC using the software Solidworks. The project uses the modeling capabilities for the design process, CFD for the gas pressure drop calculations and the water-cooling thermodynamics, and finite element modeling for force placement. Due to limitations on gasket materials, the gasket compression calculations were done mathematically.

Goals	Part	Process
Compare Gas Channels for Improvements	Bipolar Plate	CFD Pressure Drop
Water cooling Design and required Flowrate	Bipolar Plate	CFD Thermodynamic
End Plate Design Compression Comparing	Clamping Bracket	Finite Element
Gasket Design Force Calculations	Gasket	Mathematically

Table 1 Project goals

The gas pressure drop calculations are used to check for improvements in the gas flow due to the redesign of the serpentine flow pattern. These calculations are important because of the limitations the redesign causes on larger active area PEMFC. This limitation is due to the high pressure drop. Reducing the high pressure drop allows the cell size to increase.

The cooling channels are evaluated to find the required flow rate of water needed for the PEMFC stack. A correctly-designed cooling system will be needed to design the full system in the future.

Another important part of this project is the redesign of the end plates. The end plate designs are very important to the efficiency of the PEMFC stacks, and they are difficult to evaluate without FEA simulation. The challenge of moving the forces to the center of the end plate to make an even force on the bipolar plates has been studied before, but no standard solution has been found (Alizadeh, Ghadimi, Barzegari,

Momenifar, & Saadat, 2017). The emboss design chosen for this project was selected due to the low cost of stamping parts and the lower weight of the combination of the emboss metal with an internal end plate of polycarbonates compared to a solid steel end plate. The challenge of this embossed end plate design is that the layout of the embossed design can be done in unlimited variations.

This project is designed to be a stepping stone for future PEMFC designs and testing. With the promising results from the dual-direction multichannel serpentine design bipolar plates and the embossed end plate, these innovations could possibly help future PEMFC manufacturing by reducing research and development and increasing performance. Additionally, Solidworks is a well-known and accessible software so other researchers can use this project as a guide to build simulations of PEMFCs using Solidworks in the future. Table 2 shows a list of tests done to make the conclusions in this project.

Test	Process
Gas channels flowrate test for single out bipolar plate	CFD Pressure Drop
Gas channels flowrate test for dual out bipolar plate	CFD Pressure Drop
Gas channels flowrate test for dual out with added radius to channels	CFD Pressure Drop
Water cooling Design and required Flowrate by changing water flow	CFD Thermodynamic
Water cooling Design efficiency change by adding radius to channels	CFD Thermodynamic
End Plate Design Compression Comparing with and without emboss up to endplate	Finite Element
End Plate Design Compression Comparing with and without emboss though a cell	Finite Element
Gasket Design Force Calculations of original design	Mathematically
Gasket Design Force Calculations of reduced material design	Mathematically
Calculate total force needed	Mathematically
Calculate bolt size and quantity needed for total force	Mathematically

Table 2 List of testing in this project

CHAPTER 3: BI-POLAR PLATE REVIEW

3.1 Background

The bi-polar plates are an important part of the PEMFC as they control the flow of gases, the cooling flow, the removal of byproducts, including water, and the flow of the electricity produced. There are many designs when it comes to the bi-polar plate; a few examples are the Pin design (Figure 2 left side), Cascade design (Figure 2 right side), Parallel design (Figure 3 left side), and the Serpentine design (Figure 3 right side).

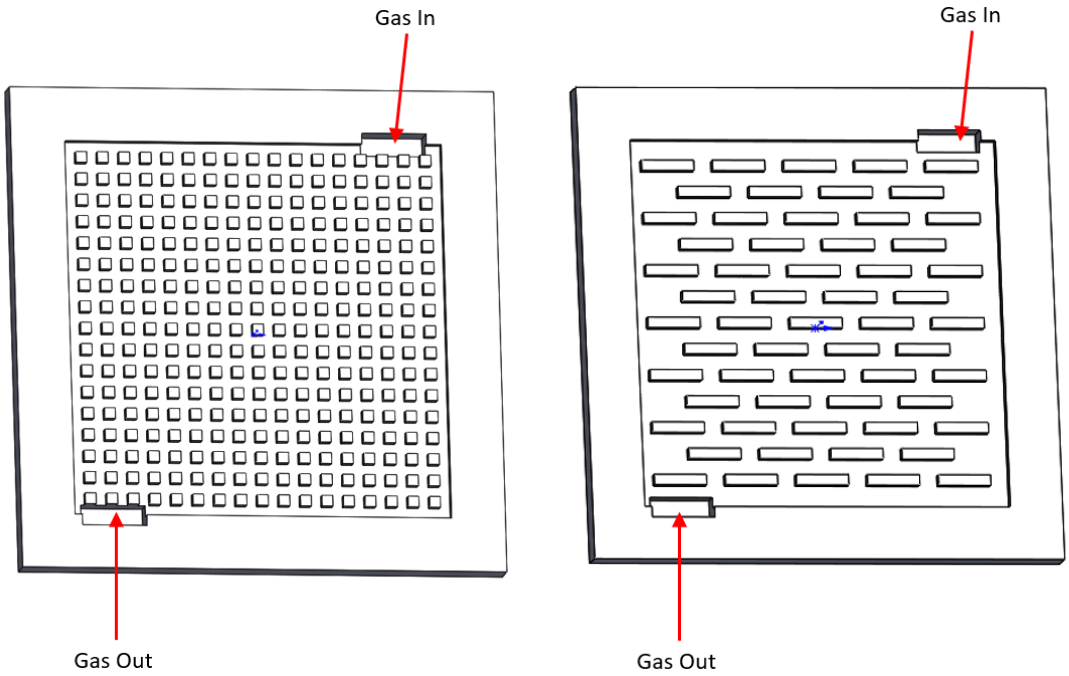

Figure 2 Pin bipolar design (left), Cascade bipolar design (right)

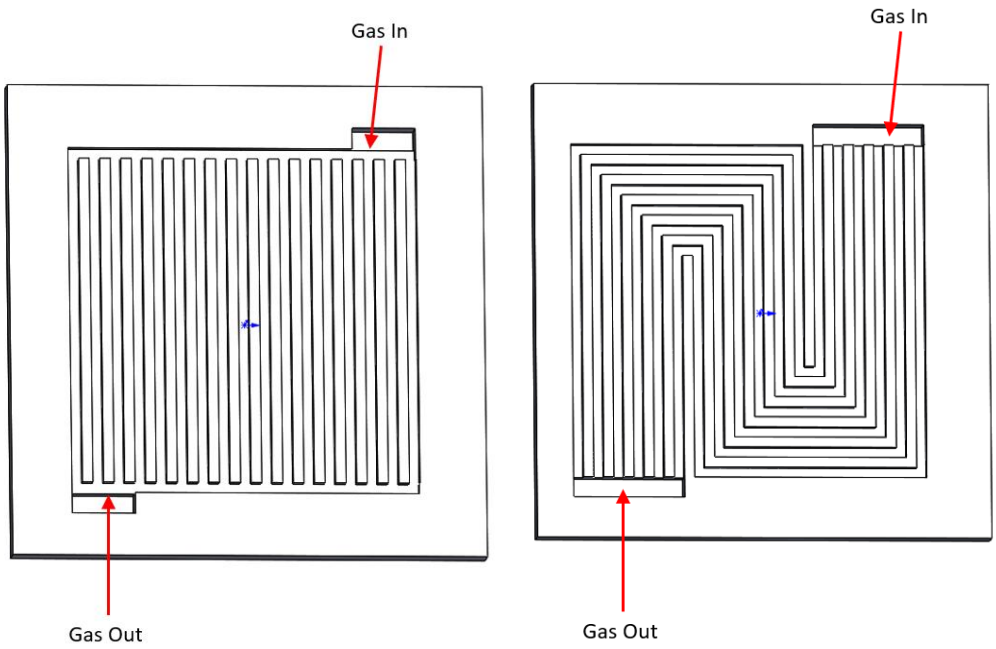

Figure 3 Parallel bipolar design (left), Serpentine bipolar design (right)

A poorly designed bipolar plate can cause uneven gas distribution, hot spots in the MEA, unstable current density, and cell failure due to bad water management (Wilberforce & Ogungbemi, 2019). The life and efficiency of the PEMFC stack can be directly related to the design of the bipolar plate. The pressure drop across the bipolar plate affects the performance of the bipolar plate as it shows restrictions in the gas flow and how well water that is produced by the reaction is removed from the system so that the MEA does not get flooded. To provide a better understanding of the requirements of the bi-polar plate design, Wilberforce & Ogungbemi's (2019) comprehensive study on the effect of bipolar plate (BP) geometry design on the performance of photon exchange membrane (PEM) was reviewed.

3.2 Review

The performance of the PEM fuel stack directly relates to the reactants being evenly distributed over the active area. The distributions of the reactant gas are managed directly by the design of the bipolar plates. The bipolar plate design also relates to the efficiency of cooling and energy removal. Wilberforce and Ogungbemi's (2019) article provide an in-depth examination of each component that makes up the design of the bipolar plate.

The most critical issue in bipolar plate design is minimizing the pressure drop of gases as they pass through the bi-polar plate. Fuel cell scientists recommend that the pressure drop be reduced to the barest minimum (Wilberforce & Ogungbemi, 2019). Pressure drops in bipolar plates are related to the plate's design, the length of the channels, and the depth of the channels. Other factors include the material surface finish and shape of the channel. The compositional material and manufacturing process will give the friction factor of the channels. The friction factor is also called the roughness factor, which is used in simulations. Another design factor is the width of the ribs in between flow channels. The study concluded that a wider channel with thinner ribs is recommended; this is based on pressure drop over the length of the channel. The shape of the cross section of the channel is also reviewed. The channel could be a triangle or a rectangle, as well other shapes. Based on the report, the triangle shape produces higher voltage but is prone to flooding, so a rectangle cross section is preferred.

The pin, cascade, parallel, and serpentine flow pattern designs are examined. The pin-like design has a low pressure drop but is limited by uneven distributions of gases, which leads to the possibility of flooding and uneven temperature distributions. The cascade design has a high pressure drop and a low rate of penetration of the gases,

resulting in efficiency problems. The parallel design provides low pressure drop but causes a nonuniform distribution of gases. The serpentine design is the commercially-accepted design as it has both good water management and thermal conductivity with enhanced flow rates; however, the serpentine design is also limited by higher pressure drops and some uneven reactions.

The directions of the air flow against the hydrogen flow are important to the performance of the bi-polar plates. There are three different options for how the flow directions relate to each other. The first choice is that the gases flow in the same direction, directly on the other side of the MEA. The second choice is to have the gases flowing across each other in a perpendicular relation. The last type is for the gas flows to move in opposite directions. Research has shown the opposite direction design is the most efficient due to the more evenly humidified MEA, reduced flooding, and increased current density.

3.3 Relation to this project

This project will use information from Wilberforce and Ogungbemi's (2019) study expand upon their findings. The bi-polar plate design in this study uses the parallel design due to its high performance and preference in industry. This study examines the issue with the pressure drops caused by the long channels of the design to make improvements. The rectangular channel design will be used and compared to rectangular channels with a radius in the corners to see if there is any improvement in performance. The flow channel directions will be a modified opposite directional flow, so the hydrogen and oxygen will be traveling in different directions.

3.4 PEMFC Design Overview

A PEMFC is designed to convert hydrogen gas into electricity. The process uses hydrogen and oxygen to produce electricity with byproducts of H_2O and heat.

The Anode reaction is on the hydrogen side of the PEMFC.

$$H_2 \rightarrow 2H^+ + 2e^- \qquad \text{Anode Reaction} \tag{2}$$

The Cathode reaction is on the oxygen side.

$$\frac{1}{2}O_2 + 2H^+ + 2e^- \rightarrow H_2O + heat \quad \text{Cathode Reaction} \tag{3}$$

The PEMFC operates in a temperature range between 20 and 180 degrees Celsius. (Alrweq 2018)

The reaction is illustrated in Figure 4, which was drawn based on the drawing used by the National Museum of American History, Smithsonian Institution. (National Museum of American History, 2021)

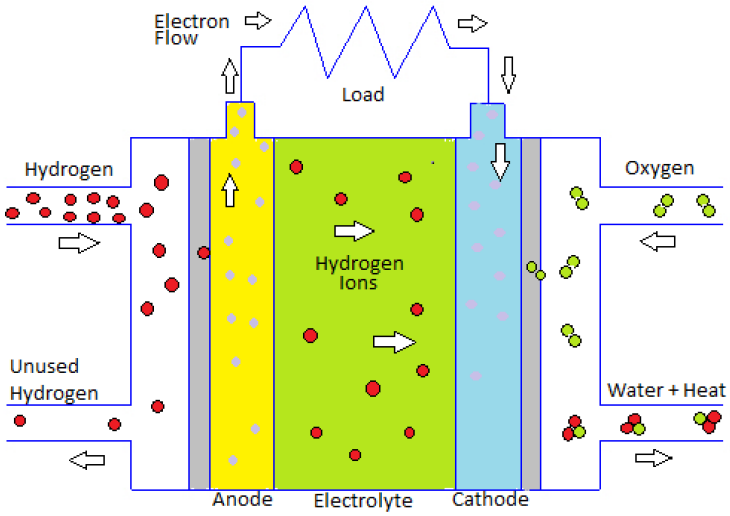

Figure 4 Illustrated PEMFC reaction.

The major parts of a PEMFC consist of the cell itself, which includes the bipolar plates, the GDLs, the seals, and the MEA. These cells are stacked together to increase

output; this creates a PEMFC stack. The parts of a PEMFC stack include the cell assemblies, the gaskets, end cooling plates, the current collector plates, end plates, gas fittings, clamping brackets (optional), and fasteners.

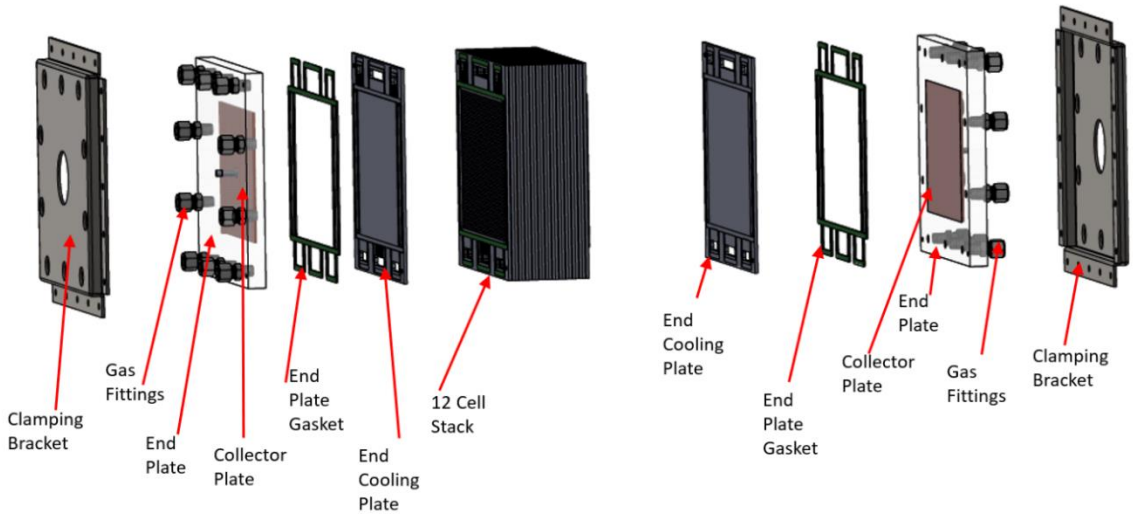

Figure 5 Parts of a PEMFC Stack

The gases and cooling water flow through the end plates. The fittings are on both end plates but can be plugged on one side if the stack is not large enough to need extra inputs and outputs. The inputs and output can be seen in Figure 6

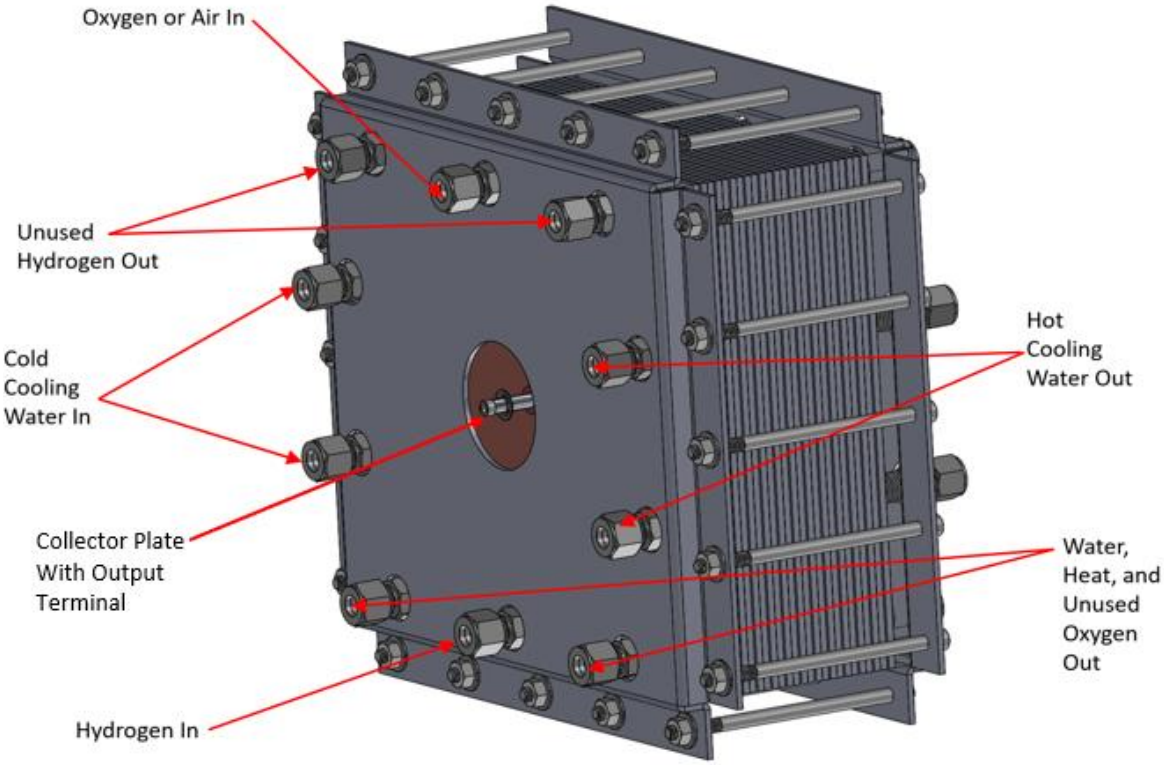

Figure 6 The PEMFC Stack inputs and Outputs

CHAPTER 4: CLAMPING FORCE

4.1 Background

The clamping force is the force that is applied to the end plate to compress the PEMFC stack. The force must seal the gas flow channel and the cooling channel and make good contact for conductivity. The clamping force can be done in different ways, but it is common to use an end plate made of a stiff material like metal or reinforced plastic that transfers the force from the bolts to the stack of the PEMFC. Researchers state that around 59% of the total power lost in a PEMFC is to the contact resistance between the bipolar plate and the GDL layer, which is predominately caused by ununiformed pressure from the end plates (Alizadeh, Ghadimi, Barzegari, Momenifar, & Saadat, 2017).

The main problem with the end plates and bolt design is that, as the clamping force is increased, the end plate begins to have a slight bow which causes the force to maximize around the edge of the stack. The pressure in the middle of the bipolar plate is lowest due to this curving of the plate. Figure 7 shows how the forces are exerted on the end plate and the bipolar plate.

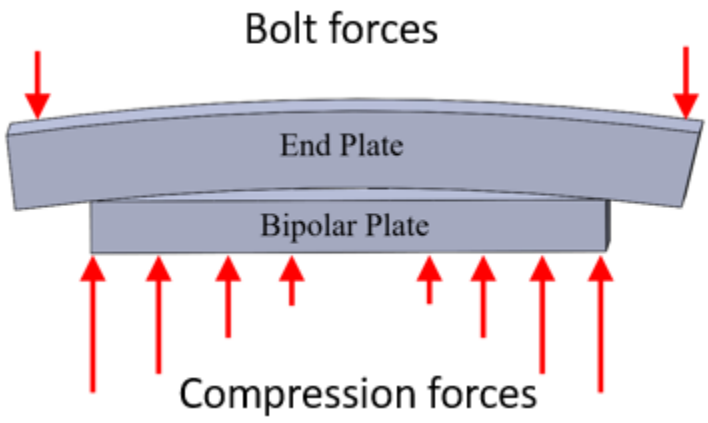

Figure 7 The forces on the end plate with the curvature

A common way to fix this problem is to make the end plate out of a thick piece of stainless steel and add drilled and tapped holes placed in a pattern in the center of the plate. The tapped holes are then filled with bolts that can be tightened to apply more force to the middle. This design does help, but it causes point pressure on the bipolar plate and is a very heavy option based on the weight of the plate and the extra bolts. Alizadeh, Ghadimi, Barzegari, Momenifar, and Saadat (2017) look at a solution for this problem.

4.2 Review

The paper looks at a new solution for the uneven clamping force caused by the end plates using finite element modeling to show the difference in performance between designs. The design is a hydraulically pressurized pocket that is installed in between the end plate and the bipolar plate. The pocket can be pressurized after the bolts are tightened to add the even force to the center of the bipolar plate. This even force improves performance and reduces hot spots caused by the uneven contact pressure on the MEA. The pocket was placed on one side of the stack and was designed using two O-rings. The space between the O-rings becomes the pocket after the O-rings are compressed. Then, the air pressure can be regulated to change the forces on the center of the bipolar plates.

The finite element testing was setup using a single cell in the two designs, first with the standard clamping setup and the second with the pressurized pocket. ABAQUS FEA simulation software was used for the calculations. The model with the standard setup had the largest pressure (4.8 MPa) on the outside corner of the bipolar plate and decreased to zero on the center area. The design with the pressurized pocket has a mostly even pressure range across the MEA. On the outside of the MEA, the pressure is 2.02 MPA while the pressure is 1.36 MPa in the center. The test was also done with contact

pressure film which resulted in similar results. Overall, the pressure pocket design is shown to be very promising with an improvement in the uniform distribution of the pressure on the MEA.

4.3 Relation to this project

In this project, finite element modeling will be used to check for improvements in end plate design. Solidworks Simulation will be used in a similar fashion. The authors used a pressurized pocket to result in a more uniform pressure distribution but, in this project, embossed end plates will be used.

CHAPTER 5: PEMFC DESIGN

5.1 Bipolar Plate Design

The bipolar plates are designed to control the flow of gases and cooling water. They must be made of conductive and thermal materials. On one side of the bipolar plate, there are channels for the gas flow. The other side of the bi-polar plate is for cooling.

The gas side of the bipolar plate highly affects the performance of the fuel cell. Based on its design, it can affect the current density, water management, pressure drop, and gas distribution (active area covered). In this project, several serpentine channels are combined; this design was chosen because it produces a lower pressure drop, removes water effectively, covers the full active area with gas flow, and is useful for large active areas (Wilberforce & Ogungbemi, 2019). The challenges of this design are that longer channels produce greater pressure drops and non-uniform reactant due to lower hydrogen levels toward the end of the flow channels. A 300 cm^2 active area bipolar plate was chosen to show how the pressure drops across a larger area PEMFC. A 200 cm^2 active area PEMFC is known to be large (Carcadea, 2020).

By increasing the number of channels, the pathway gets shorter. In figure 8, the bipolar plate has a 12-channel serpentine design that was created for this project testing.

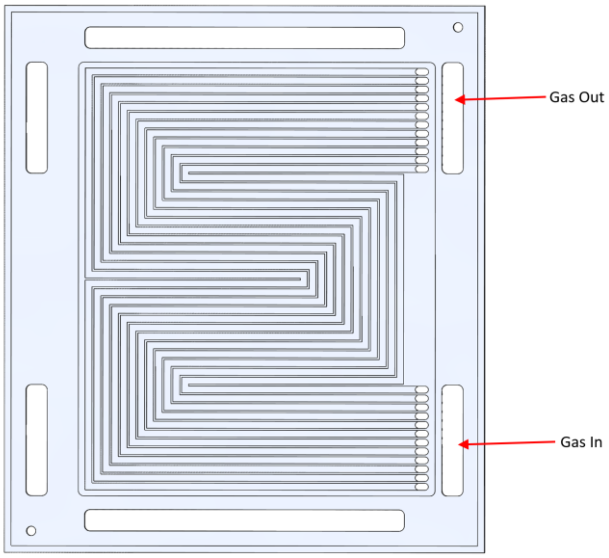

Figure 8 A 12 channel serpentine design bipolar plate

The 12-channel design allows the channels to travel across the active area only four times which helps to reduce pressure drops caused by the directional changes at the corners of the design pattern. The major issue with this design is that the channels are still long, which causes a larger pressure drop than a smaller active area bipolar plate. The channels are 28.05 inches long. To increase the efficiency of the bi-polar plate, the channel length needs to be decreased.

To decrease the length of the channels, a twin output design was made. The design moved the inlet to the center on one side and made an upper and lower outlet. This allows

the channel to be much shorter. The dual outlet design is shown in Figure 9.

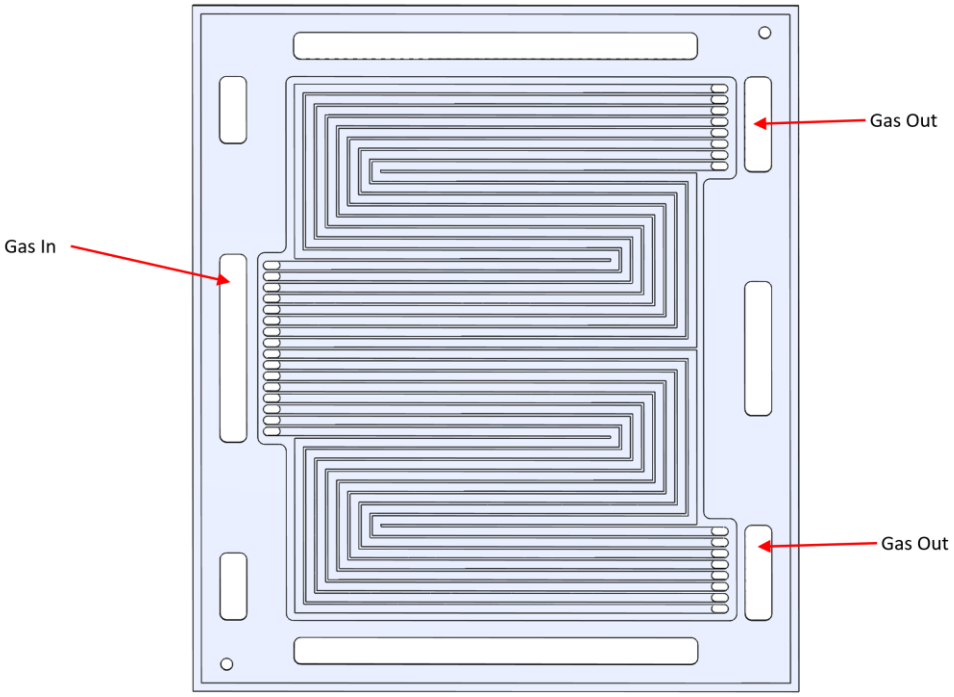

Figure 9 Dual outlet design

With the dual outlet design the channel's length is 18.68 inches, which is 9.37 inches shorter than the previous design. The effects of this change will be simulated using CFD to find the change in pressure drop.

The shape of the channels is the next important consideration for gas channels in the bi-polar plate. Square like channel bends as shown in Figure 10 increase the pressure drop compared to curved channels as in Figure 11 (Wilberforce & Ogungbemi, 2019).

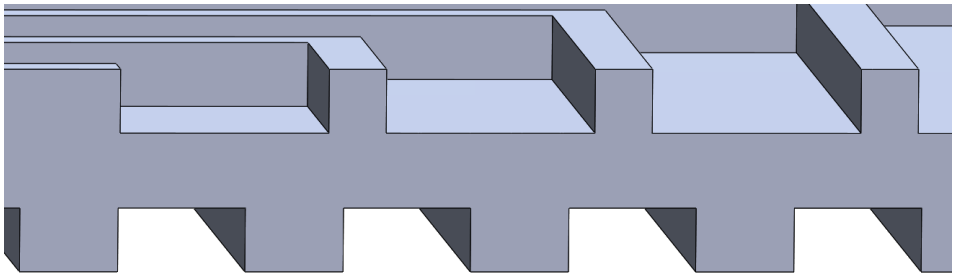

Figure 10 Bipolar plate with square bends

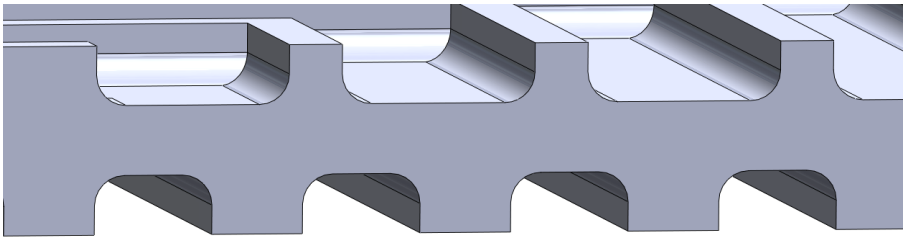

Figure 11 Bipolar plate with curved channels

In this project, CFD simulation is used to find the radius to reduce pressure drop without reducing the flow rate by the reduction of the channel area.

The next aspect of the bi-polar plate to investigate is the cooling channels. The cooling channels are evaluated using CFD to find the pressure and flow rate needed to keep the bi-polar plates cool. Additionally, the bends of the channels are evaluated to see their effects on the plates' cooling. The cooling channels are shown in Figure 12.

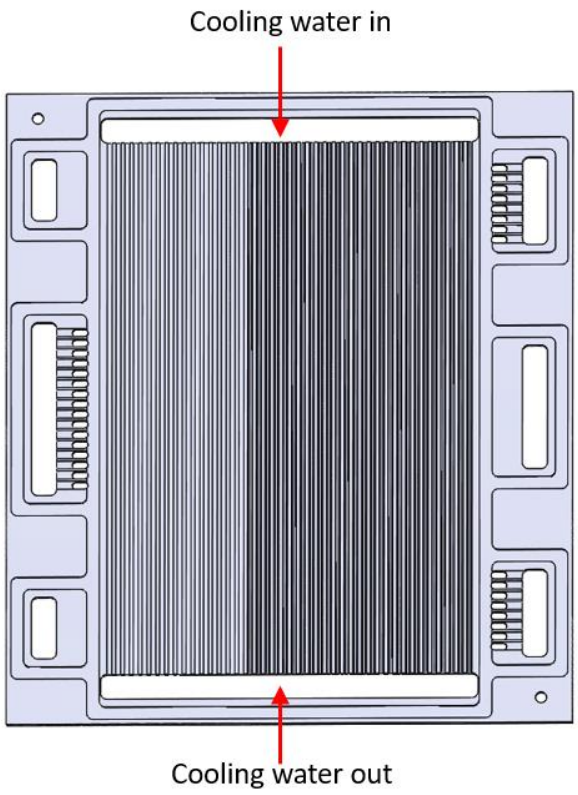

Figure 12 Cooling channels

5.2 Gasket Design

The gasket design is important in many ways for the effective and efficient performance of the PEMFC. First, the gasket seals the gas layers and cooling layers so that there are no leaks. Second, gaskets must be made from a material that can withstand the gas and temperature changes. Third, the compression of the gasket determines the conductivity of the plates. Fourth, the thickness of the gasket determines the amount of pressure on the GDL.

In this design, two materials are examined, Silicone and EPDM (Ethylene Propylene Diene Monomer rubber). Both materials are readily available and are used in PEMFC designs.

Material hardness directly affects the force needed to compress the gasket and the gaskets ability to seal. Silicone is available with Shore A hardness from 10 to 100 durometer. EPDM is available with a Shore A hardness from 40 to 80 durometer. The higher the shore hardness (stiffness), the higher the sealing pressure is (Lin, Chien, Tan, Chao, & Van Zee, 2011). LSR and EPDM show a stable and steady stiffness under the temperature range up to 90ºC (Lin, Chien, Tan, Chao, & Van Zee, 2011). A common shore hardness for both EPDM and silicone is 70 to 75, which will be used for this design.

Examining how a material holds up under use in a PEMFC is another important consideration when selecting a gasket material. Silicone rubber has been tested and does not meet the requirements for use in PEMFC. Silicone can degrade at 60ºC and have mechanical change at 80ºC. The degradation starts at surface hardening then goes onto cracking (Tan, Chao, Li, & Van Zee, 2007). This makes is unsuitable as a gasket material in PEMFC.

EPDM rubber was also tested to see how it met the requirements of usage in PEMFC. The testing shows that operational temperatures do not affect the material. EPDM does not display surface hardening or any changes in mechanical properties (Tan, Chao, Wang, Gong, & Van Zee, 2009). Due to preexisting testing results, EPDM has been chosen for this project. The force used in this project to compress the gasket was derived from the charts produced by Parker Hannifin Corporation. Based on the chart for square gasket G008 divided by its cross-section area, the value of 61.58 PSI (424.027 Pa) is found to produce a compression of 10% of the gasket thickness (Parker Hannifin Corporation - TechSeal Division, 2020).

There are two different gasket designs in PEMFC, which serve different functions. These two gasket designs are the gasket on the MEA side of the bipolar plate and the gasket on the cooling side of the bipolar plate.

The MEA side of the bipolar plate gasket has more than one function. The first function is to seal all the gas sections and the water section. The second function is to control the compression pressure on the GDL. Figure 13 shows the cell with the gas side gaskets.

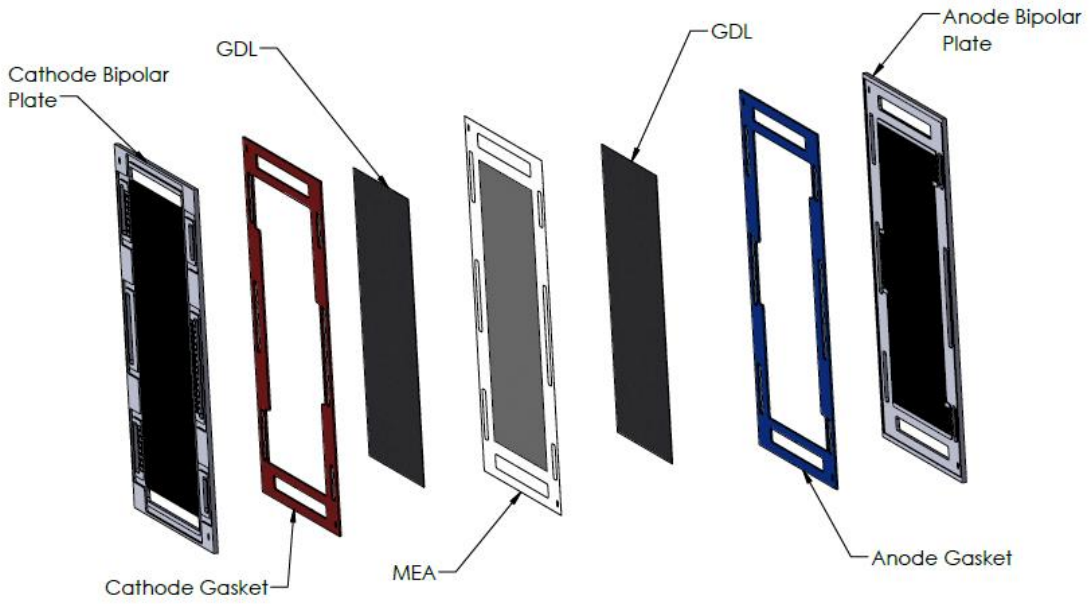

Figure 13 Cell detail showing gas side gaskets

As you can see in Figure 13, the GDL sits in the middle of the gaskets. In Figure 14, the gasket is shown in its location on the bipolar plate where it seals all the gas and water passages.

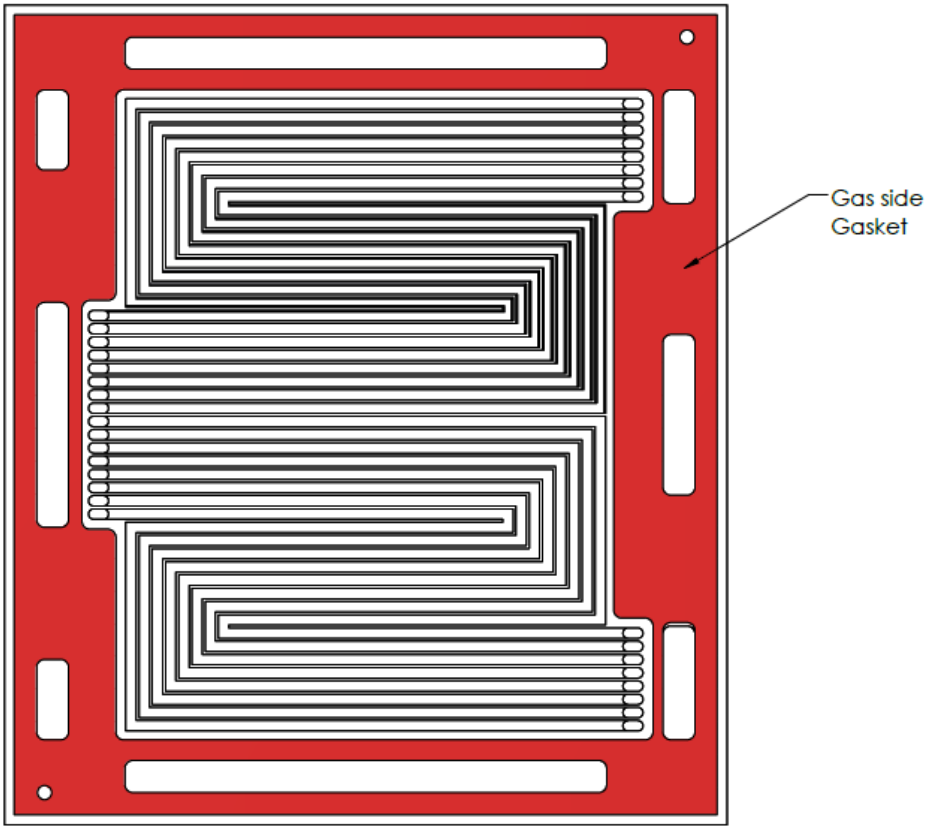

Figure 14 The bipolar plate with gas gasket

The gasket sits down in a cutout in the bipolar plate to keep it from moving and to help it seal the gas channels. The gasket has a high surface area, so the amount of compression can be better controlled by force. The compression amount is very important because the forces on the GDL is controlled by the final gasket thickness and its required forces. The placement of the GDL is shown in Figure 15.

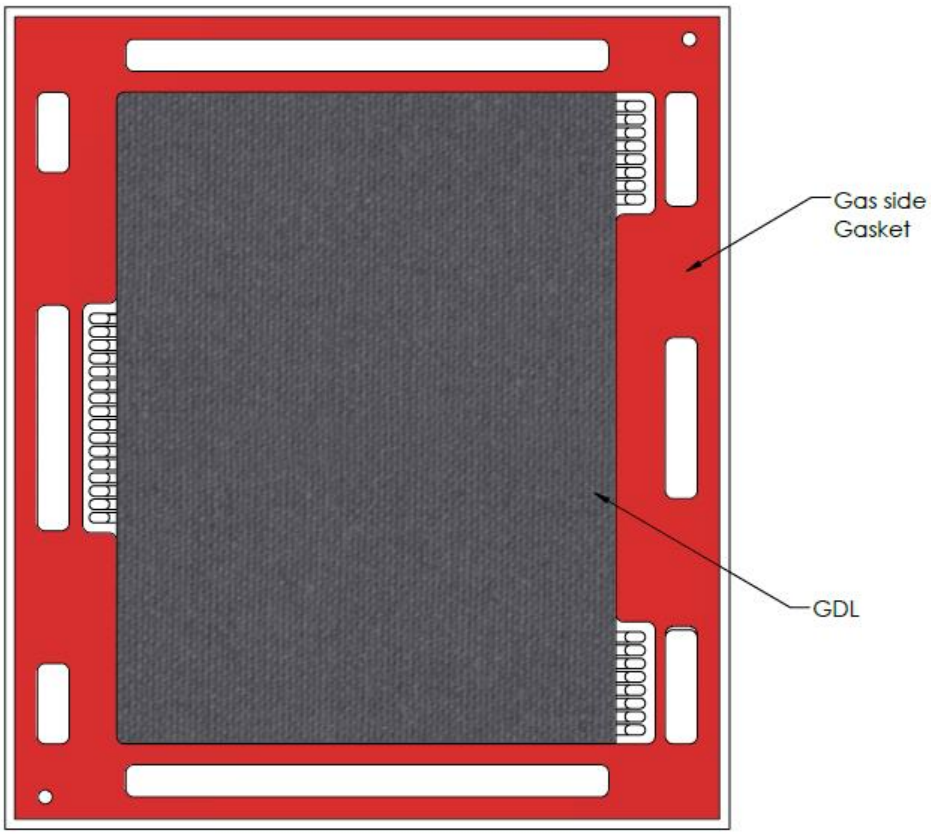

Figure 15 Bipolar plate with gasket and GDL

The GDL compression is very important for two reasons. First, if the GDL does not make good contact between the bi-polar plate and the MEA, then GDL resistance will go up. As contact pressure increases, the resistance decreases, which improves the electrical and thermal conductivity of the cell and helps support a more uniform distribution across the active area. Research has revealed that 59% of power lost in a PEM fuel cell is due to contact resistance between the GDL and the bi-polar plate (Alizadeh, Ghadimi, Barzegari, Momenifar, & Saadat, 2017). As the contact pressure increases, the GDL may become deformed, which reduces the thickness and porosity of the GDL, and causes the GDL to intrude into the bipolar plate flow channels (Atyabi, et al., 2019). The research shows an improvement in the performance of the GDL up to a pressure of 4.5 N/mm^2 with a decrease in performance at higher pressures.

The GDL material greatly affects the deformation under pressure, so it must be examined when choosing the material. Three materials are examined for this project, SGL 29BCE, Toray TGP-H 060, and Freudenberg H2315. SGL 29BCE has its optimal pressure at 0.5 N/mm^2, and, as the pressure is increased past this point, the performance decreases. The optimal pressure range of the Toray TGP-H 060 0.7 to 1.6 N/mm^2, and, as the pressure is increased past 1.6 N/mm^2, the performance decreases; higher pressures also cause permanent damage to the material. Freudenberg H2315's optimal pressure range starts at 0.7 N/mm^2, continues to be flat at higher pressures, and does not have any permanent damage, even at a pressure of 6 N/mm^2 (Irmscher, Qui, JanBen, Lehnert, & Stolten, 2019).

Do to the improvement of contact pressure up to 4.5 N/mm^2, its s flat optimal performance level, and its ability to operate without damage at high pressure levels, Freudenberg H2315 was chosen for this project. The design will be set for an optimal GDL pressure of 1 N/mm^2. This GDL pressure has been chosen because the compression information is available by the manufacturer. The manufacturer states that the GDL thickness changes from 0.210mm to 0.170mm with 1 MPa (145.038 psi) of force (Freudenberg, 2020).

The water-cooling side of the bipolar plate has a differently designed gasket due to its different needs. The main difference is that the cooling side plates need to be in contact with each other to minimize electrical resistance. Figure 16 shows the placement of the cooling gasket.

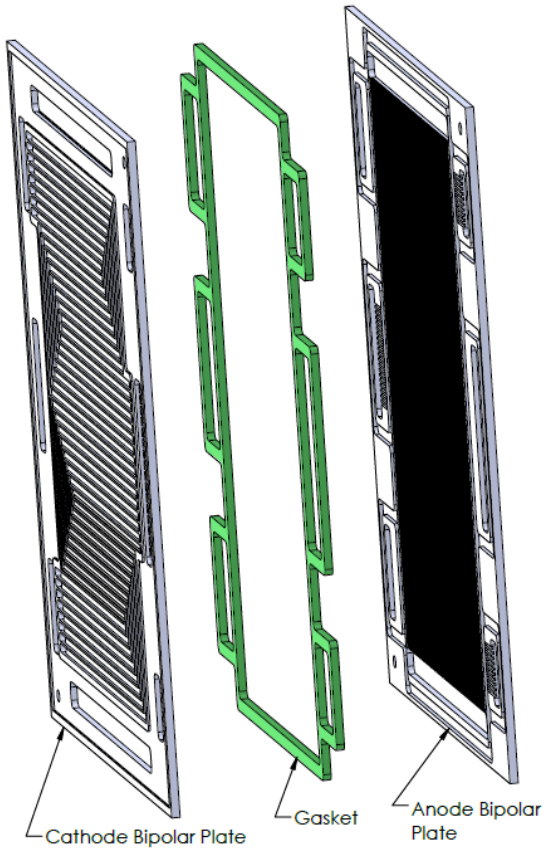

Figure 16 Bipolar plates with cooling side gasket

The gasket gets compressed in between the Cathode and Anode bipolar plates so the thickness of the gasket is very important. If the gasket is too thick, due to the compression needed for the gas gasket, the cooling gasket will not be compressed enough, and the plates will not come into full contact as needed. If the gasket is too thin, then there will not be enough sealing force to keep the water and gases from leaking. Using calculations, in this project, the correct thickness will be found so that the plates encounter each other with a little less force than what is needed on the MEA side gaskets; this way the cooling sides of the plate come into full contact. Figure 17 shows how the gasket matches up to the bipolar plates.

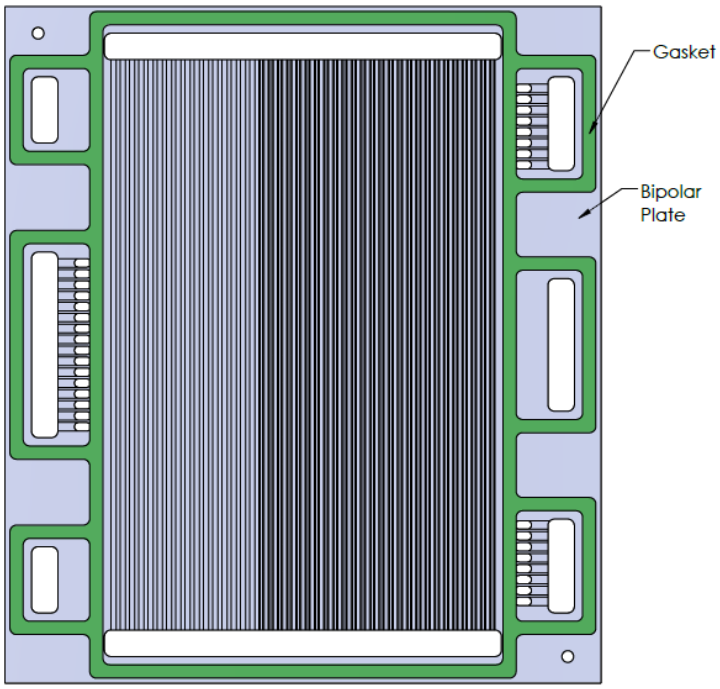

Figure 17 Cooling side of the bipolar plate with gasket

5.3 Clamping Bracket Design

The clamping bracket is used to transfer the clamping force needed to compress the PEMFC stack to the bolts that produce the force. On this design, sheet metal is used with a polycarbonate plate as an insulator. The polycarbonate plate is also used to install gas and water fittings. The thickness of the sheet metal can be used to change force, and, if needed, emboss can be used to change placement of the forces. In metalwork emboss is to raise a on a blank with dies of similar pattern, one the negative of the other (Dictionary.com, LLC, 2021). Due to the thickness of the sheet metal used the emboss will be made using a stamping process. The design of the clamping bracket must apply a uniform force to the stack.

The thickness of the clamping plate directly relates to the uniformity of forces applied to the stack, and this increases the weight and material cost (Alizadeh, Ghadimi,

Barzegari, Momenifar, & Saadat, 2017). Simulating embossed sections of the clamping plate will help to achieve uniform pressures.

Chapter 6: Bi-polar Plate Simulation

6.1 Flow Channel Length Simulation

The flow simulation (CFD) in Solidworks is used to evaluate the influence of the length of the channel on the pressure drop. The simulation uses a set pressure change, and this gives a mass flow rate which is compared for both channel length to evaluate the change.

The simulation material properties used in all the Solidworks CFD and FEA simulations are found in Table 3.

Material	Graphite	Copper	Polycarbonate	304 Stainless Steel
Eleastic Modulus (Mpa)	4800	110000	2320	190000
Poisson's Ratio	0.28	0.37	0.3912	0.29
Mass Density $\left(\frac{N}{mm^3}\right)$	2240	8900	1190	8000
Tensile Strength (Mpa)	100.826	394.38	62.7	517017
Yield Strength (Mpa)	120.594	258.646		206.807
Thermal Conductivity $\left(\frac{W}{m * K}\right)$	168	390	0.189	16
Specific Heat $\left(\frac{J}{Kg * K}\right)$	712	390	1535	500

Table 3 Material properties used in Solidworks simulations

The single in, single out standard design serpentine bipolar design is evaluated first. The first step is to enclose the flow channels as shown in figure 18.

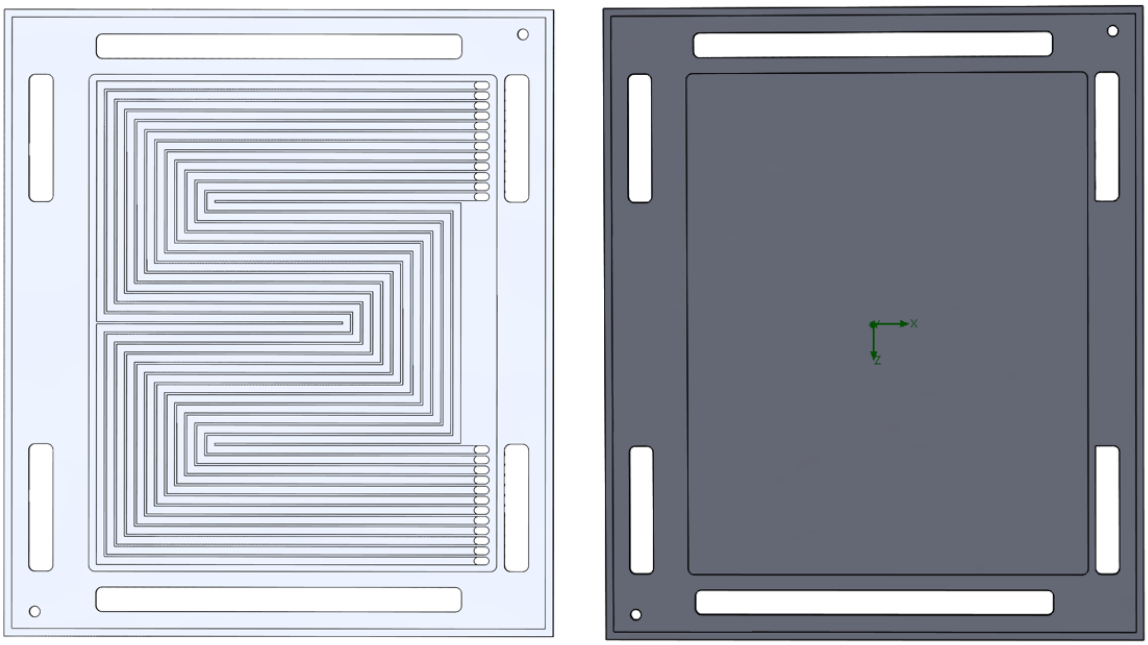

Figure 18 The flow channels open and closed

Figure 18 shows two models. On the left, is the model with open channels, which shows how the part is produced; on the right, is the model with the enclosed channels, which is needed to create the flow channels. The next step is to create caps so that the flow channels can be created. Figure 19 shows the created flow channels, with a total volume of gas as 26 milliliters.

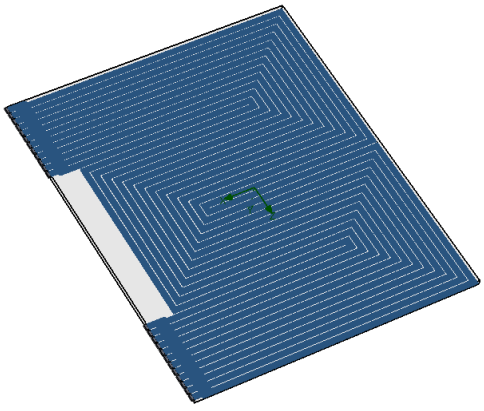

Figure 19 Single in single out bipolar plate flow channels

Next, the boundary conditions and goals are created to compare the two options, single out and dual out, and the mass flow rate is calculated. Due to the need to make the gas flow, the inlet pressure is set at 5 psi above ATM pressure (135798.78 Pa) and ATM pressure (101325 Pa) is used for the output making a pressure drop. The boundary conditions are shown in Figure 21.

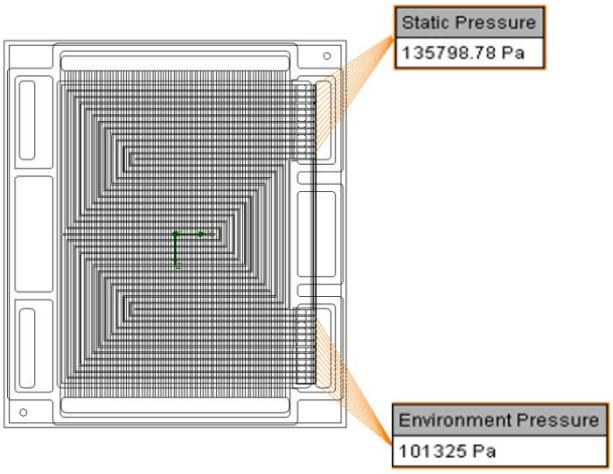

Figure 20 The boundary conditions setup for the single out bi-polar plate

The final step before running the CFD is to setup the mesh. A five cells wide mesh was used across each of the channels in both simulation of the single out and dual outlet. The mesh is shown in figure 21.

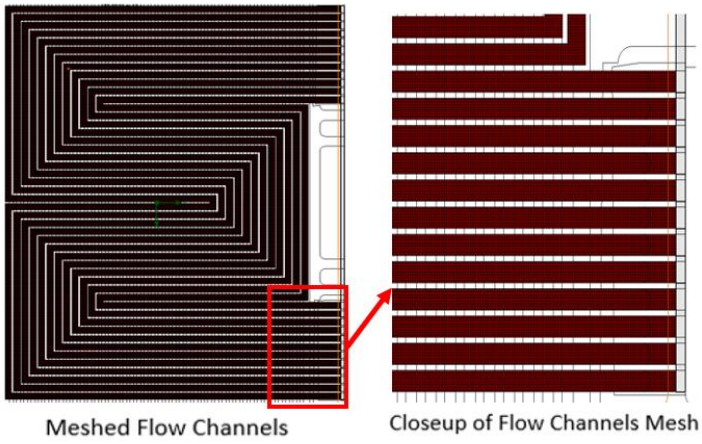

Figure 21 The meshed flow channels with a closeup of the mesh

The CFD goes over iterations until it comes up with a solution. The iterations versus mass flow rate is shown in Figure 23.

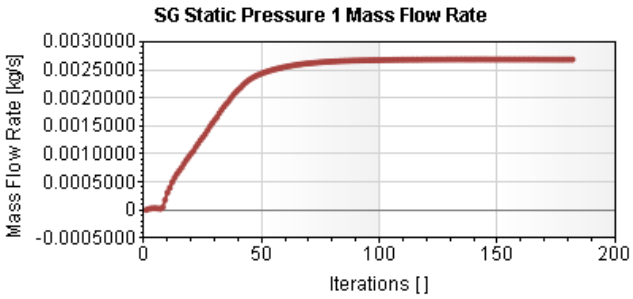

Figure 22 CFD iterations vs mass flow rate

The calculated values of the flow channels are shown in Table 4.

Goal Name	Unit	Value	Average Value	Minimum Value	Maximum Value
SG Static Pressure 1 Mass Flow Rate	$\frac{kg}{s}$	0.002687	0.002684	0.0026692	0.0026879
SG Static Pressure 1 Volume Flow Rate	$\frac{m^3}{s}$	0.001665	0.001664	0.0016546	0.0016661
SG Static Pressure 1 Velocity AV	$\frac{m}{s}$	42.28717	42.25726	42.031476	42.309074

Table 4 The single out flow channels calculated solutions

The most important finding is that, with a drop-in pressure of 5 psi, the mass flowrate of the single out bipolar plate is .0026865 kg/s.

The same test was performed on the dual outlet bipolar plate. In Figure 23, the open and closed flow channels are shown.

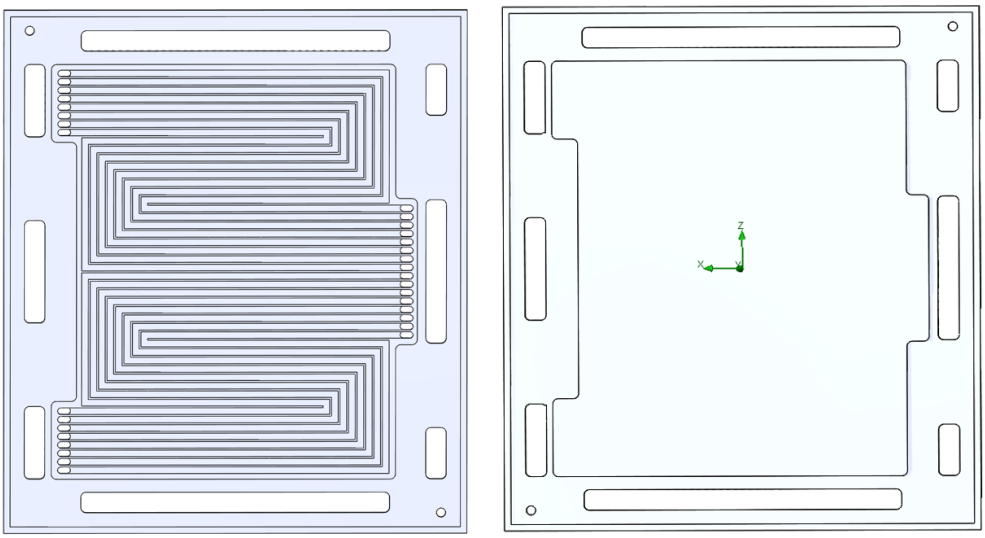

Figure 23 Open and closed flow channels for dual outlet

The same boundary conditions are set on the dual outlet bipolar plate, except the two outlets are set at ATM pressure. The boundary conditions for the dual outlet bipolar plate are shown in figure 24.

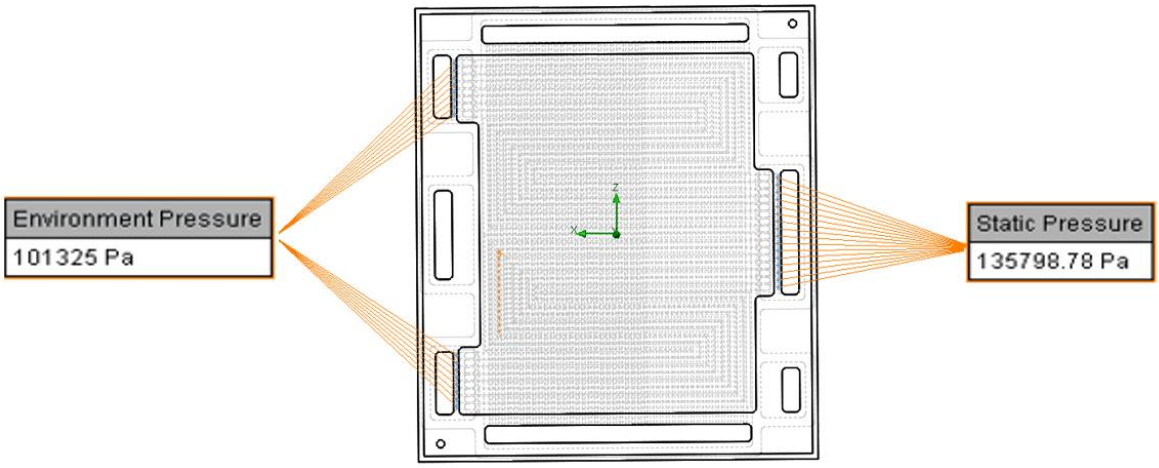

Figure 24 Boundary conditions of the duel outlet bipolar plate

Figure 25 shows the flow channels with the total volume of the flow channels as 27 milliliters.

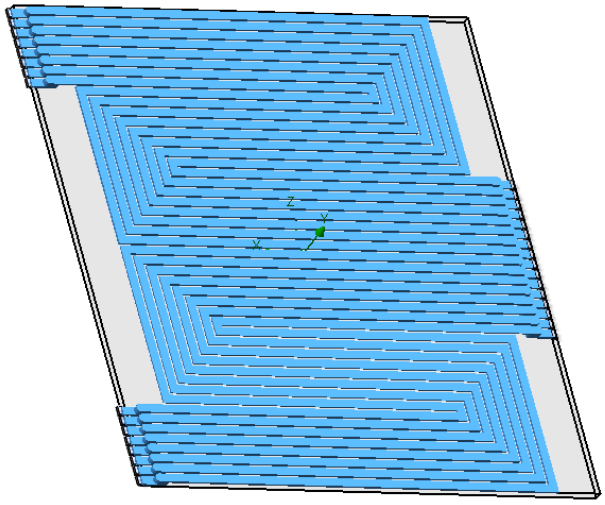

Figure 25 Flow channels of the duel outlet bipolar plate

The iteration curve of the dual outlet bipolar plate is shown in Figure 26.

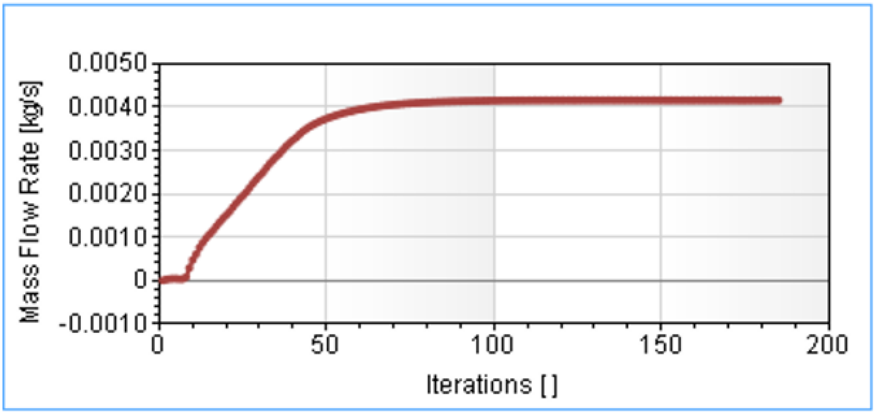

Figure 26 The plot of iterations vs flowrate

The CFD results for the dual outlet bipolar plate are listed in Table 5.

Goal Name	Unit	Value	Average Value	Minimum Value	Maximum Value
SG Static Pressure 1 Mass Flow Rate	$\frac{kg}{s}$	0.004133	0.004133	0.0041187	0.0041365
SG Static Pressure 1 Volume Flow Rate	$\frac{m^3}{s}$	0.002562	0.002562	0.002553	0.0025641
SG Static Pressure 1 Velocity AV	$\frac{m}{s}$	48.78663	48.79451	48.638208	48.834289

Table 5 The CFD results for dual outlet bipolar plate

The CFD result show that the mass flowrate of the dual outlet bi-polar plate is 0.0041357 kg/s with the pressure drop of 5 psi used to cause the flow of gas.

The results of the two bipolar plates are compared in Table 6.

	Single Out Bipolar Plate	Dual Outlet Bipolar Plate	Increase caused by dual outlet	Percentage Change
Volume mL	26	27	1	3.70%
Mass Flowrate kg/s	0.0026844	0.0041327	0.0014483	53.95%
Velocity m/s	42.287	48.787	6.5	15.37%

Table 6 Single outlet compared to dual outlet bipolar plate

The dual outlet design is shown to have some major improvements in mass flowrate, with a 53.95% increase in performance with the same pressure drop. This demonstrates that fresher gasses will reach the cells, but higher flowrate will also help remove water deposits. The 15.37% increase in velocity will also help keep the channels clear.

6.2 Radius Simulation for Gas Channels

A 0.25mm radius was added to the dual outlet bipolar plate flow channels to see if any improvement in flowrate would be found. A radius of 0.25mm was selected because a larger radius would cause failures due to the thinness of the material between the channels. Figure 27 shows where the radius was added.

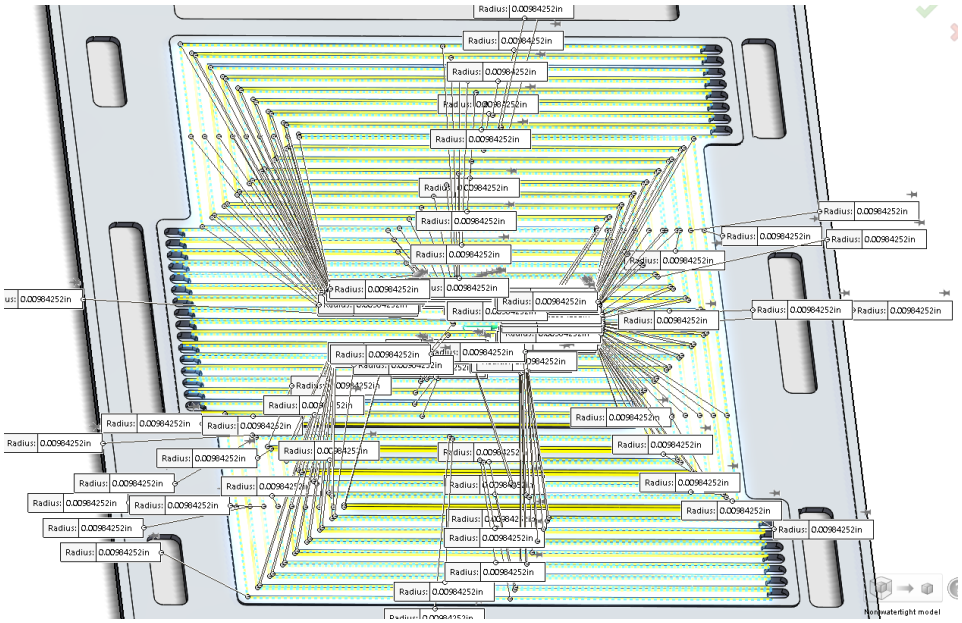

Figure 27 The added radius locations

The results are found in Table 7.

Goal Name	Unit	Value	Average Value	Minimum Value	Maximum Value
SG Static Pressure 1 Mass Flow Rate	$\frac{kg}{s}$	0.004187	0.004189	0.0041785	0.0041918
SG Static Pressure 1 Volume Flow Rate	$\frac{m^3}{s}$	0.002595	0.00259	0.0025901	0.0025984
SG Static Pressure 1 Velocity AV	$\frac{m}{s}$	49.42691	49.45197	49.34342	49.486108

Table 7 the CFD results for the dual outlet bi-polar plate with 0.25mm radius added

The results show a mass flowrate of 0.0041868 kg/s, which is an increase of 1.3%. The radius did improve the performance of the flow channels.

6.3 Cooling Channel Simulation

To evaluate the cooling channels, the first step is to calculate the waste heat produced in the fuel cell stack that must be removed from the stack by the cooling channels. To find the heat production rate equation 4 was used.

$$Heating\ rate = P_e \left(\frac{1.25}{V_c} - 1\right)\ W \quad (4)$$

Where P_e is the power produced by the PEMFC stack, and V_c is the voltage at current draw (James Larminie, 2003). For this PEMFC stack, P_e = 1000 watts, V_c = 0.65, which gives a value of 923.08 watts. There are 13 cooling sections in the stack, 11 full and 2 halves at the end plates, which gives a value of 76.92 watts per cooling set. In total, 38.46 watts are created at the top bi-polar plate, and 38.46 watts are created at the bottom.

Figure 28 shows the assembly used for the cooling simulation.

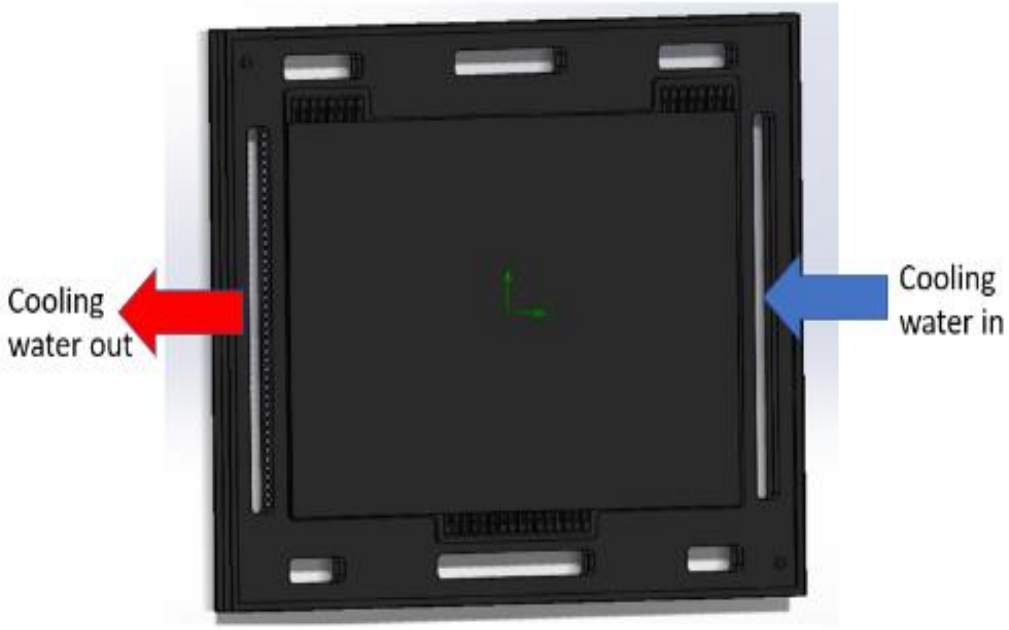

Figure 28 Cooling simulation assembly

The assembly has a cathode bi-polar plate and an anode bipolar plate situated back to back as the cooling channels flow behind them. A plate is added on both sides to represent the GDL which is where the 38.46 watts enter into the system as shown in Figure 29.

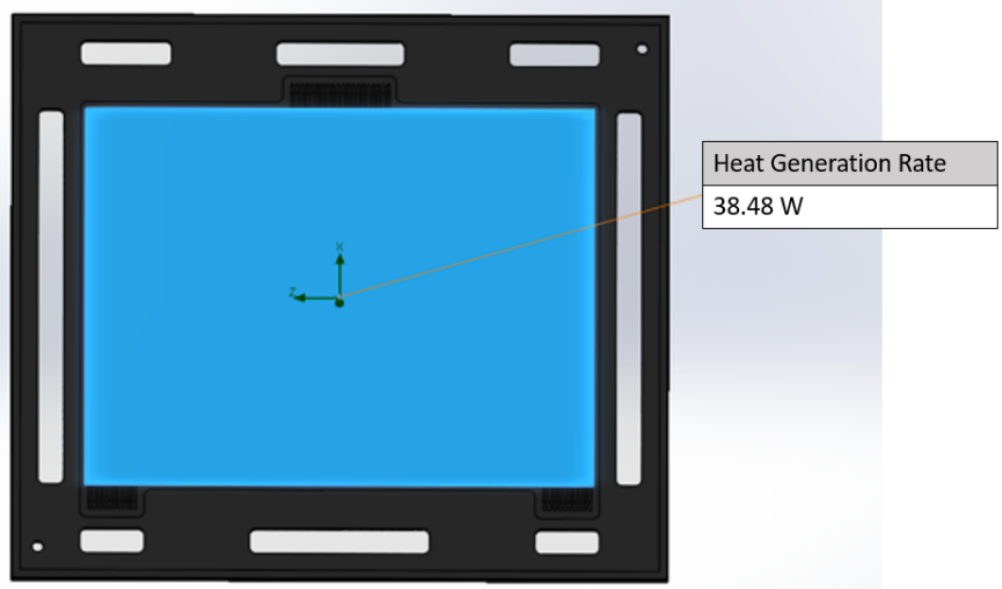

Figure 29 Cooling system heat generator locations

The boundary conditions on the inlets and outlets of the system are setup with an inlet water mass flow rate, an output pressure at 101325 Pa and an outlet temperature of 373 kelvin. The system will seek the water temperature of 373 kelvin but is limited by the mass flowrate and the heat generated. The boundary conditions are shown in Figure 30.

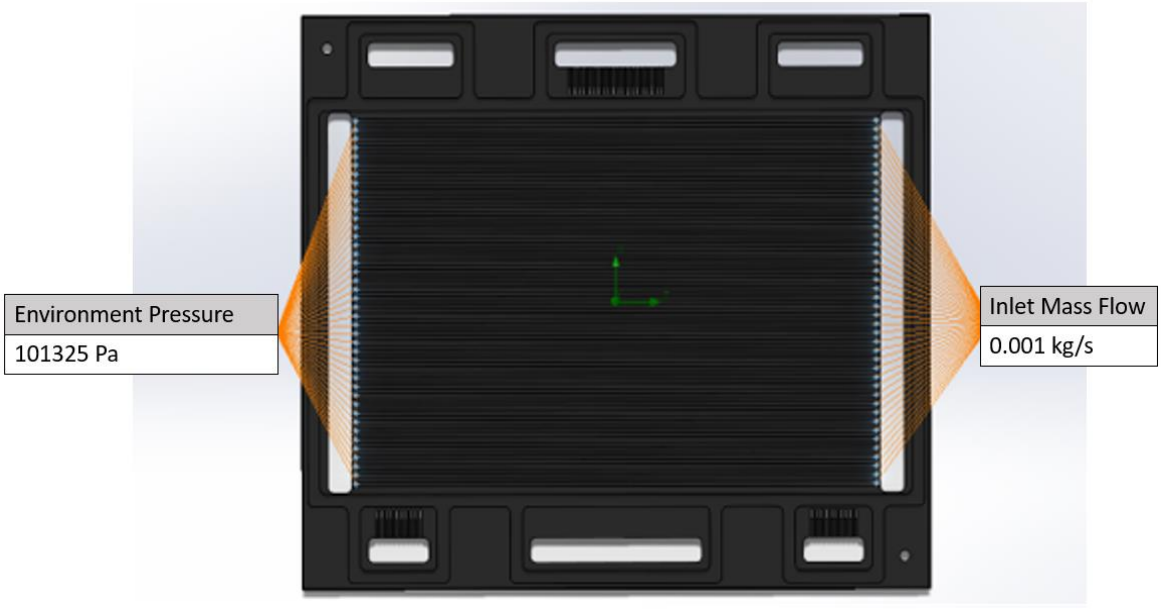

Figure 30 Boundary conditions for the cooling simulation

The cooling channels are shown in Figure 31 with a volume of 36 milliliters.

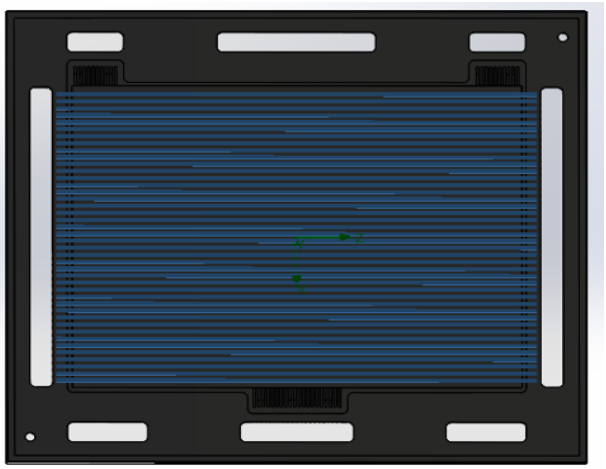

Figure 31 The cooling channels

The goal of this simulation is to find a cooling flowrate that would produce exiting water near the operating temperature of the PEMFC stack. The first flowrate examined was 0.001 kg/s, and the temperature results are shown in Figure 32.

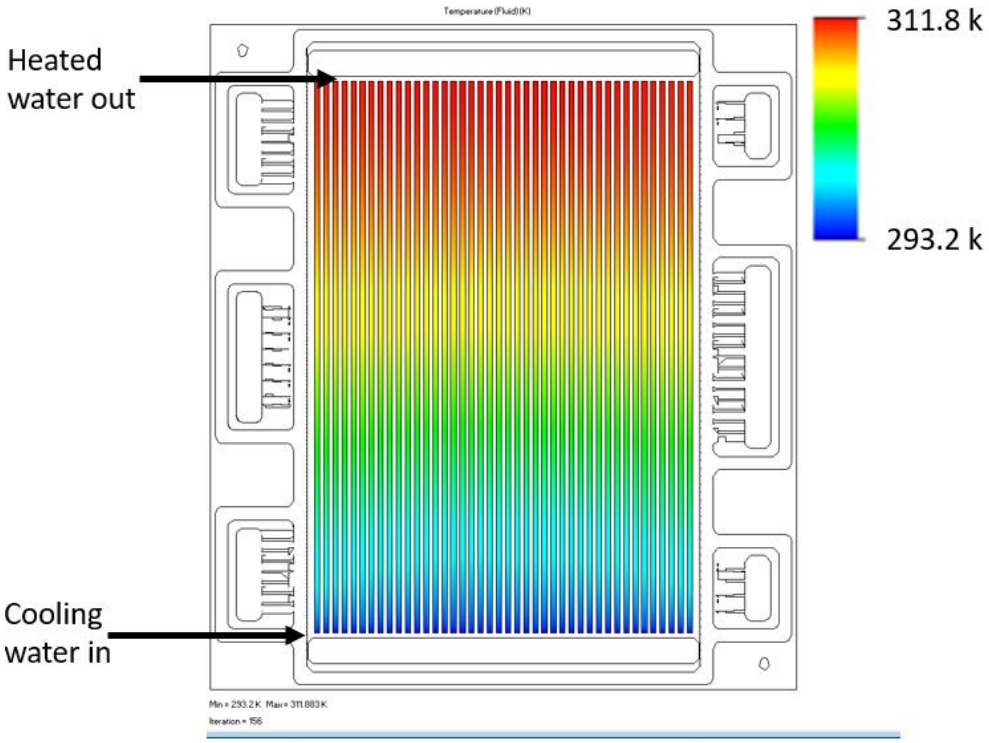

Figure 32 Simulation with a flowrate of 0.001 kg/s

At a flowrate of 0.001 kg/s (60 mL/min), the maximum water temperature at the output is 311.8 kelvin (38.65 C). The next flowrate examined was 0.0008 kg/s, which is shown in Figure 33.

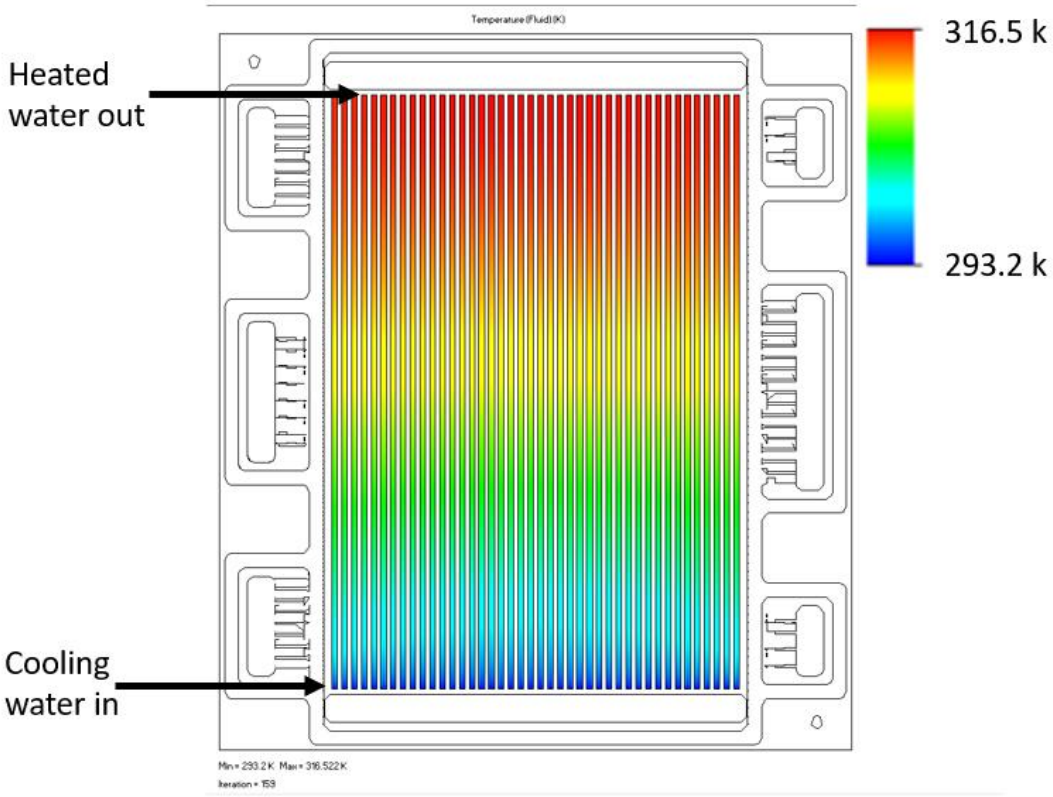

Figure 33 Simulation with a flowrate of 0.0008 kg/s

At a flowrate of 0.0008 kg/s (48 mL/min), the maximum water temperature at the output is 316.5 kelvin (43.35 C). The next flowrate examined was 0.0005 kg/s, which is shown in Figure 34.

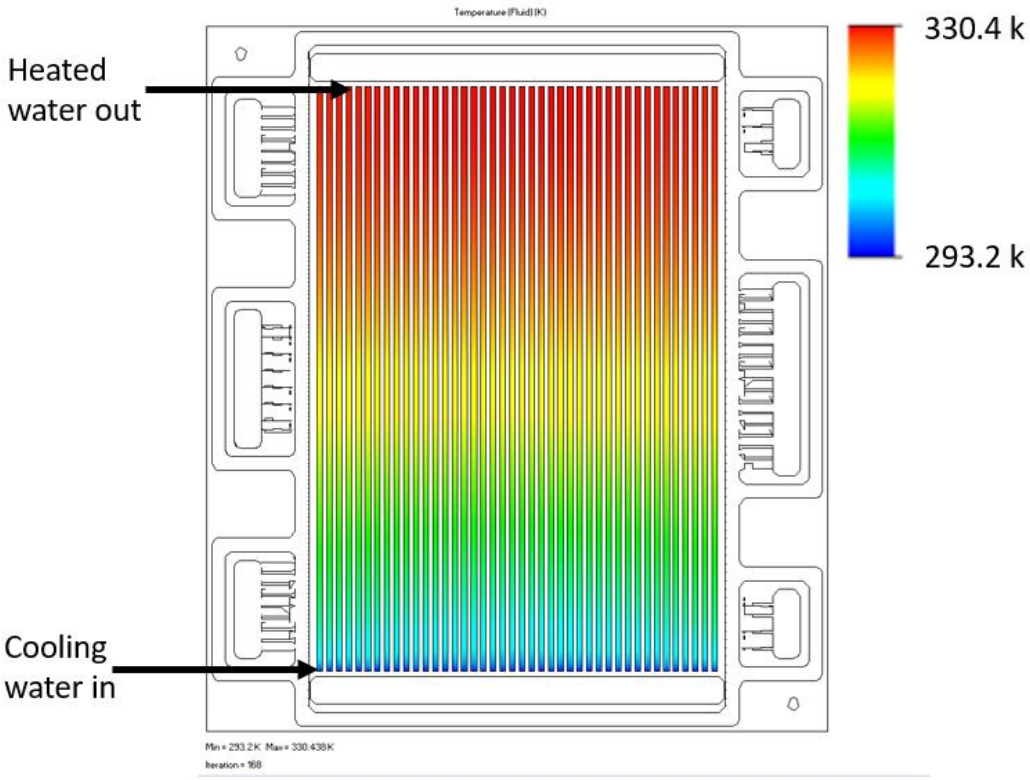

Figure 34 Simulation with a flowrate of 0.0005 kg/s

At a flowrate of 0.0005 kg/s (30 mL/min), the maximum water temperature at the output is 330.4 kelvin (57.25 C). The next flowrate examined was 0.0003 kg/s, which is shown in Figure 35.

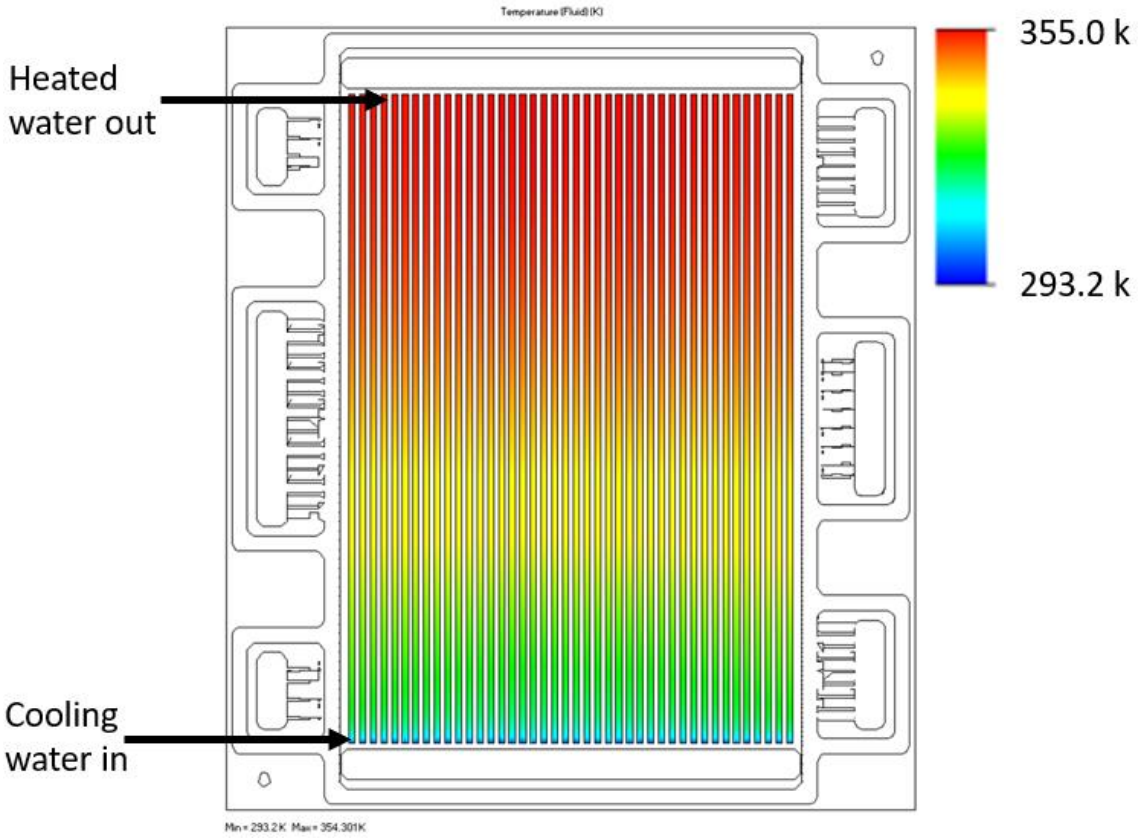

Figure 35 Simulation with a flowrate of 0.0003 kg/s

At a flowrate of 0.0003 kg/s (18 mL/min), the maximum water temperature at the outlet is 355.0 kelvin (81.85 C), which is a good operating temperature. Based on the design of the stack, which has 12 cooling areas, the total cooling water flowrate is 216 mL/min. The results from the tested flowrates are shown together in Table 8.

	Flowrate		Maximum Water Temperature	
Simulation Run	$\left(\frac{kg}{s}\right)$	$\frac{mL}{min}$	K	C
Run (.001)	0.001	60	311.8	38.65
Run (.0008)	0.0008	48	316.5	43.35
Run (.0005)	0.0005	30	330.4	57.25
Run (.0003)	0.0003	18	355	81.85

Table 8 Flowrates and maximum water temperature from cooling channel testing.

Using the flowrate of 0.0003 kg/s (18 mL/min), the corners of the flow channels are examined. The original design has square channels, and a different radius was used to see how the performance of the cooling system changed. Four radii are used in this testing: 0.15 mm, 0.25 mm, 0.35 mm, and 0.5 mm. Figure 36 show a channel inlet with a radius.

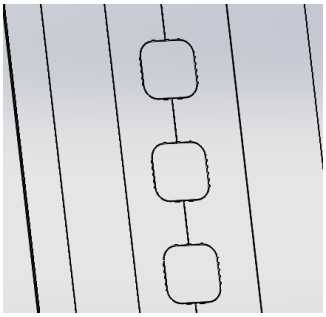

Figure 36 Cooling inlet with radius

The radii are listed in Table 9 with the corresponding outlet temperature.

Radius (mm)	Outlet Temperature (K)
NA	355.0
0.15	356.535
0.25	356.534
0.35	356.515
0.5	356.522

Table 9 Outlet temperature vs channel radius

Based on the findings shown in Table 9, a radius does increase the efficiency of the system, but it does not improve with larger radiuses.

CHAPTER 7: Gasket Compression Calculations

7.1 Calculating Forces on Gaskets

First, the surface area of the gaskets must be calculated using Solidworks.

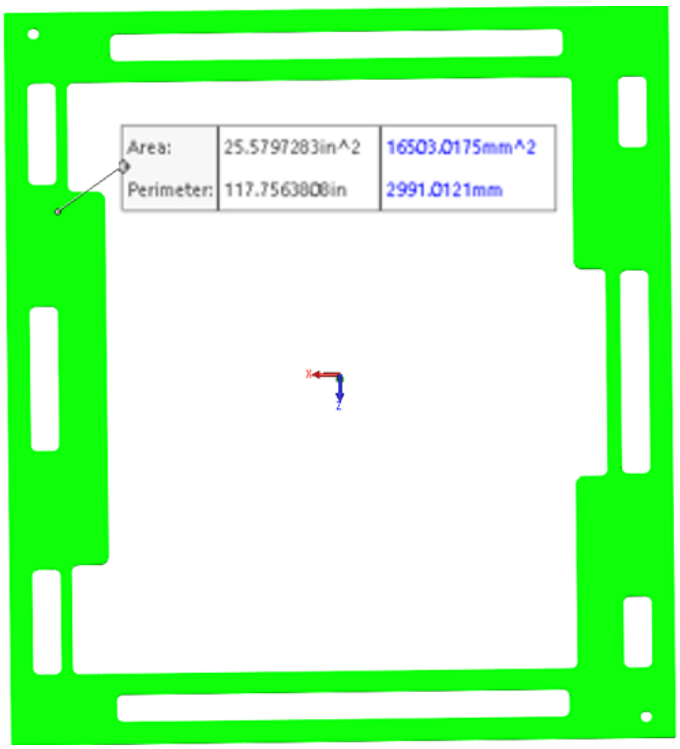

Figure 37 Cathode Gasket with an area of 25.58 in^2

The CAD model in Figure 37 shows that the area of the gasket is 25.58 in^2, which would require a force of 1,575.2 lb_f. The required force is found by multiplying the area in inches by the required pressure to compress the gasket by 10% which is 61.58 PSI. The large area of the gasket would cause a large compression force so the unneeded material from the gasket is removed to reduce the force.

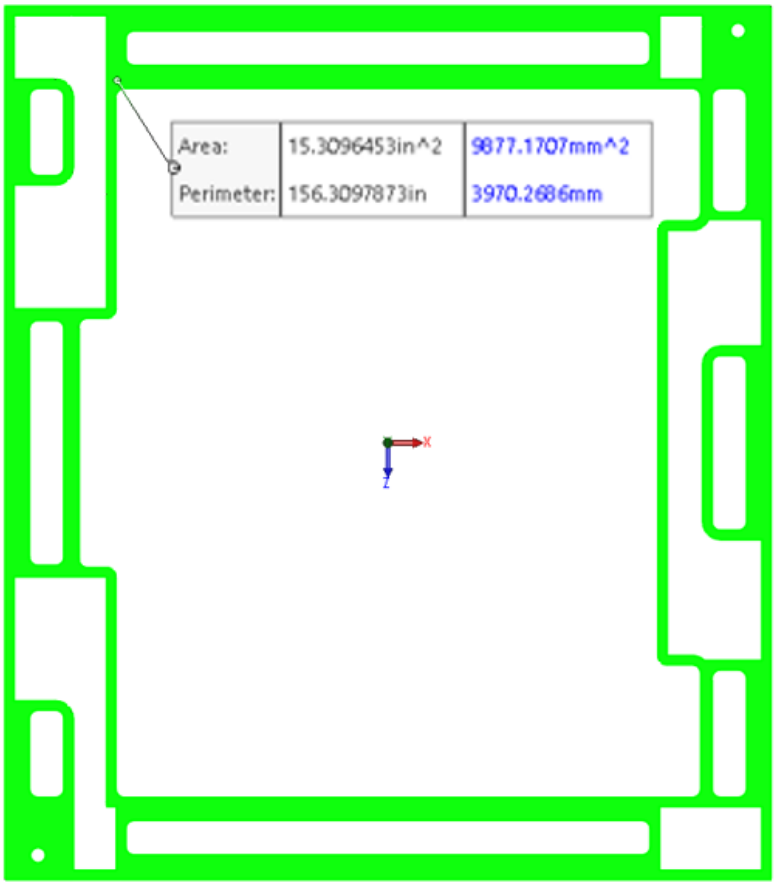

Figure 38 Cathode Gasket with material removed with an area of 15.31 in^2

As is shown in Figure 38, the redesign reduced the material area to 15.31 square inches, which now gives a required force of 942.8 lb_f. The redesign reduced the required force by 632.4 lb_f.

The next gasket to look at is the anode gasket in Figure 39.

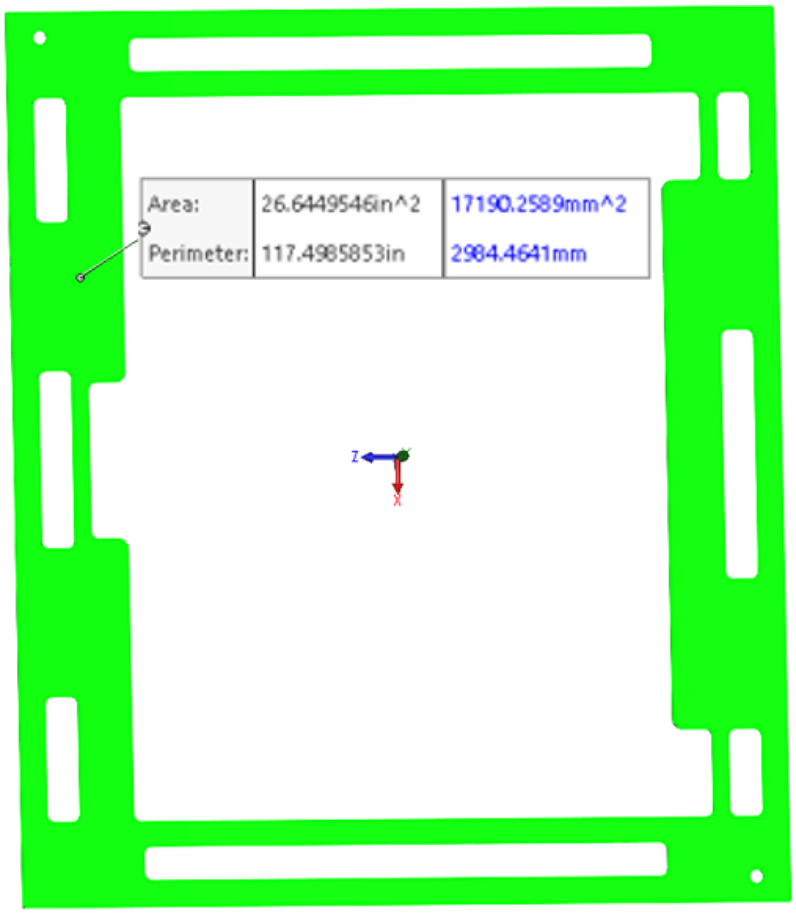

Figure 39 the anode gasket with an area of 26.64 in^2

The area of the anode gasket is 26.64 in^2, which gives a required force of 1,640.5 lb_f. Due to this high force, the area of the anode gasket will be reduced.

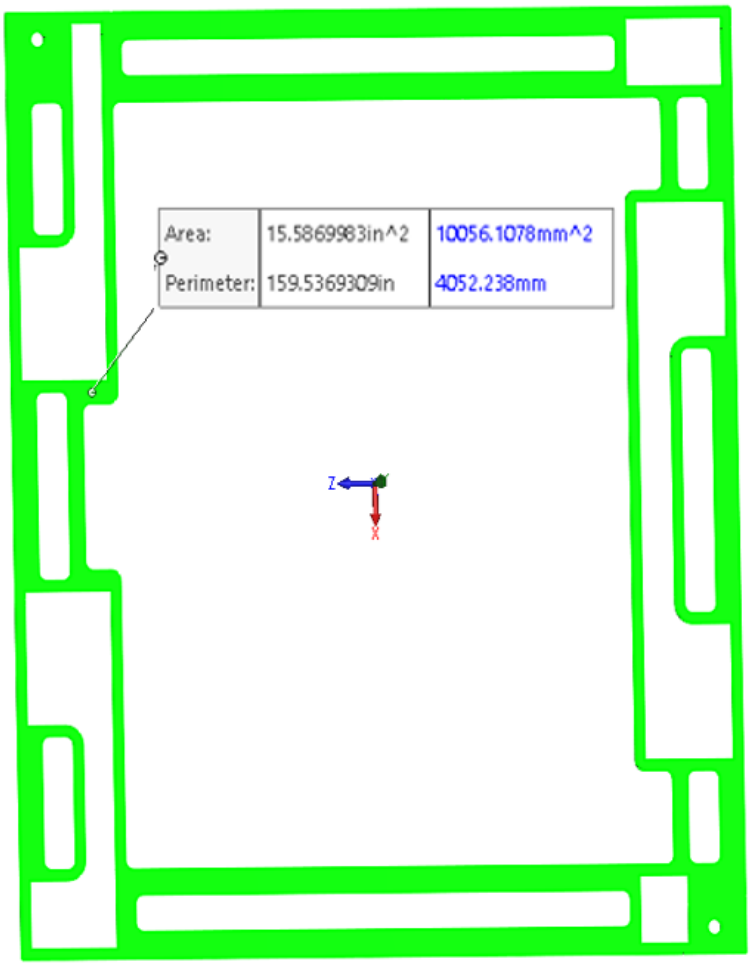

Figure 40 Anode gasket with material removed with an area of 15.59 in^2

In Figure 40, the gasket redesign is shown with its new area of 15.59 in^2, which will require a force of 960.0 lb_f, a reduction of 680.5 lb_f. The next gasket is the end plate gasket, which is used to seal the gas and water cavities.

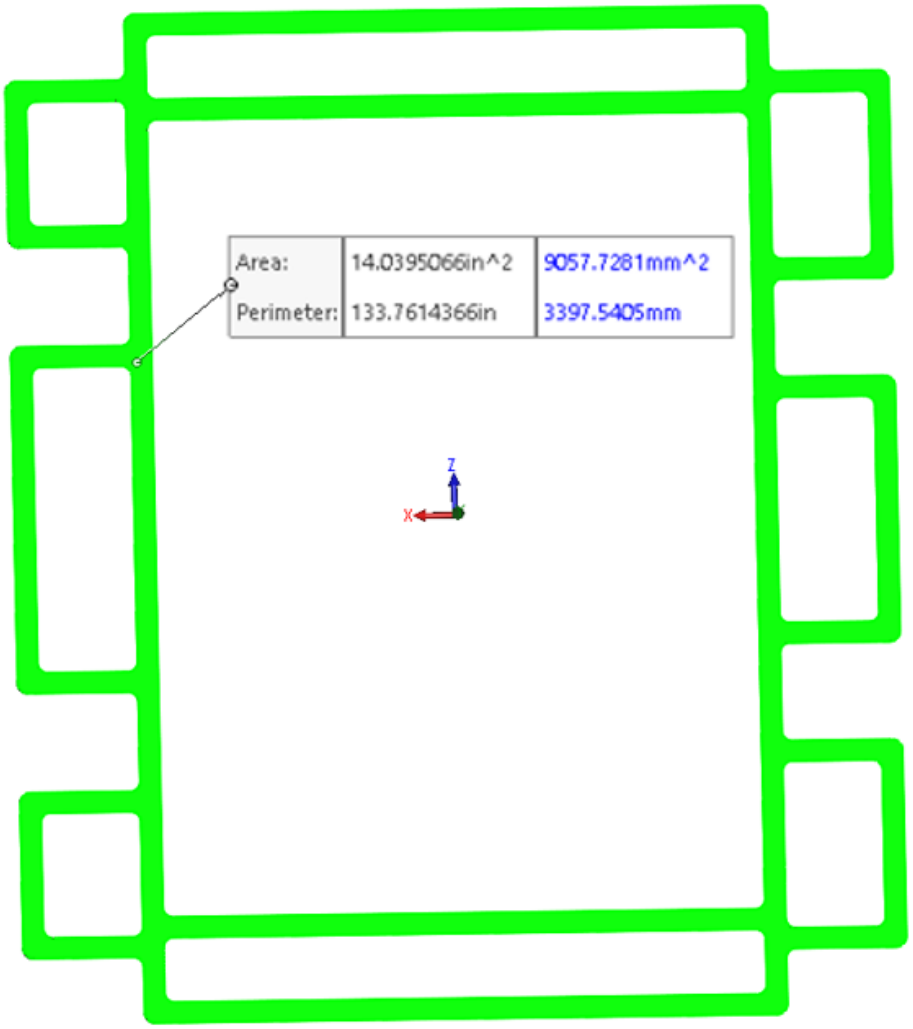

Figure 41 The end plate gasket with an area of 14.04 in^2

The end plate gasket has an area of 14.04 in^2 shown in Figure 41, which makes the gasket require a force of 864.6 lb_f.

The final gasket is the cooling channel gasket.

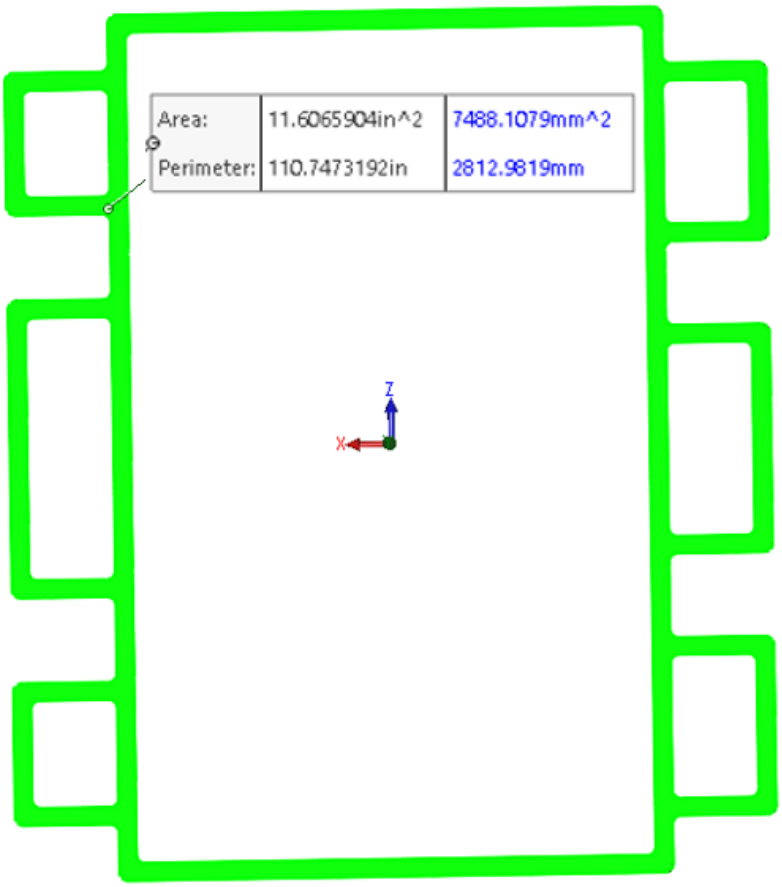

Figure 42 the cooling channel gasket with an area of 11.61 in^2

The cooling channel gasket has an area of 11.61 in^2, which will require a force of 714.3 lb_f.

The final force that needs to be determined is the force on the gas diffusion layer (GDL). To find the force, the area must be found.

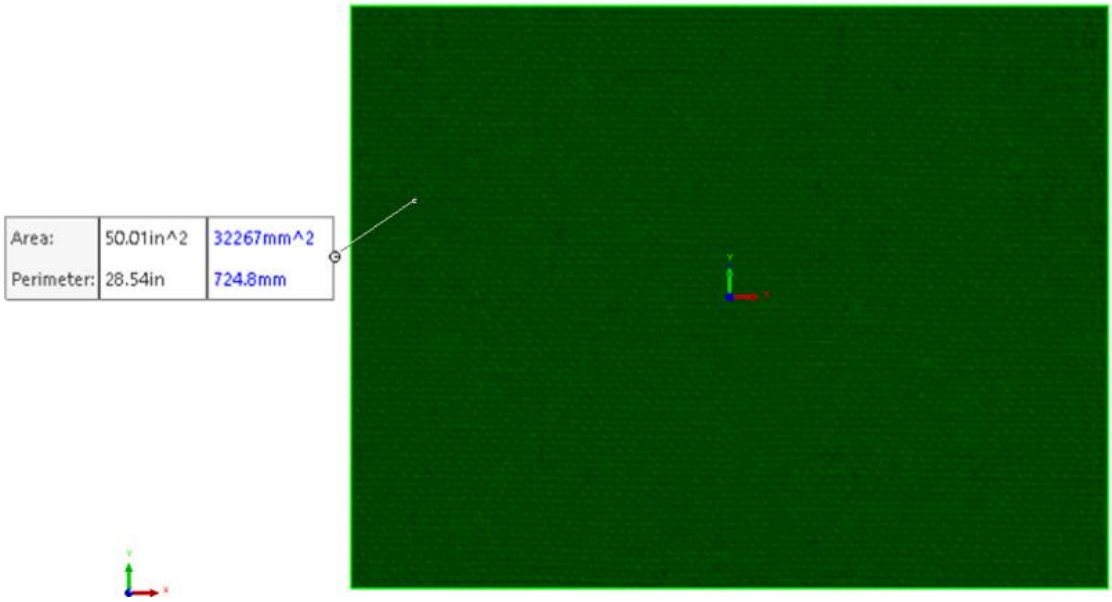

Figure 43 GDL with an active area of 50.01 in^2

Figure 43 shows that the area of the GDL is 50.01 in^2, which will require a force of 7253.4 lbf.

7.2 Material Thickness

The gasket thicknesses are calculated based on the required thickness and then calculating the thickness after 10% compression. The 10% compression was chosen as it is the minimal amount needed for EPDM gaskets based on Parker instructions on gaskets (Parker Hannifin Corporation - TechSeal Division, 2020).

Gasket	Compressed Thickness (mm)	Compressed Thickness (inches)	Original Thickness (mm)	Original Thickness inches
Cathode Gasket	0.9	0.035	1	0.039
Anode Gasket	0.9	0.035	1	0.039
End Plate Gasket	1.35	0.053	1.5	0.059
Cooling Gasket	2.7	0.106	3	0.118
GDL	0.17	0.007	0.21	0.008

Table 10 Material thickness before and after compression

The gasket cutout depth had to be slightly changed to make the gaskets' original thicknesses align with standard size sheets for die cutting. The GDL was added to Table 10 just for reference.

7.3 Clamping Forces

All the forces calculated in section IV A are listed in Table 11.

Gasket	Force Needed (lb_f)	Force Needed (N)	Qty Needed	Force Needed (lb_f) Total	Force Needed (KN) Total
Cathode Gasket	632.4	2813	12	7588.8	21347
Anode Gasket	680.5	3027	12	8166	24719
End Plate Gasket	864.6	3846	2	1729.2	6650
Cooling Gasket	714.3	3177	13	9285.9	29505
GDL	7253.4	32265	24	174081.6	5616696

Table 11 List of forces and quantities of each type

The force listed in Table 11 also show the overall force for each type of gasket and GDL. The forces required are based on the pressure need to compress the gaskets by 10% and the setting pressure of the GDL multiplied by the area. The total forces, per end plate forces, and per bolt location forces are listed in Table 12.

	Force Needed (lb_f) Total	Force Needed (N) Total
Clamping Total	200851.5	5.7E+09
Per End Plate	100425.8	2.85E+09
Per bolt location	5021.288	1.42E+08

Table 12 Force total for overall, per end plate, and per bolt

Table 12 shows that the overall clamping force of the PEMFC stack is 200,851.5 lbf. The force is then split across each of the end plates, which is 100,425.8 lbf. The per bolt location lists the force at each of the contact locations on the clamping bracket,

which is 5021.3 lbf. Due to the very high force per bolt 7/16" Lamalloy (Rated L9) bolts must be used, which have a clamping load of 11550 lbf (Engineering Toolbox, 2020).

Bolt Size (in)	Number of Bolts Needed
1/4	59
5/16	36
3/8	24
7/16	18

Table 13 The number of bolts required based on bolt size

The required bolts need was calculated by dividing the total force by the maximum clamping force of each bolt; then rounding it up to the next whole number. The maximum clamping for is 75% of the proof load force for each bolt. The calculations are in Table 14.

Total Load (lb_f)	Bolt Size (in)	Max Clamping Load (lb_F)	Total Divided By Max	Rounded Up
200851.5	1/4	3450	58.218	59
	5/16	5700	35.237	36
	3/8	8438	23.803	24
	7/16	11550	17.390	18

Table 14 Calculating the required number of bolts needed

Based on Table 13, the best bolt choices for this PEMFC is the 3/8 inch or the 7/16 inch. For this project, we are keeping 20 bolt locations so 7/16 inch is used.

CHAPTER 8: Clamping Bracket Force Simulation

8.1 Clamping Bracket Simulation Setup

The setup of the Clamping Bracket Simulation is designed to focus on the forces on the end cooling plate because the clamping bracket transfers the forces into the cell stack. The bolt holes and washers are changed to fit the 7/16 inch bolt due to the findings in Chapter 6.

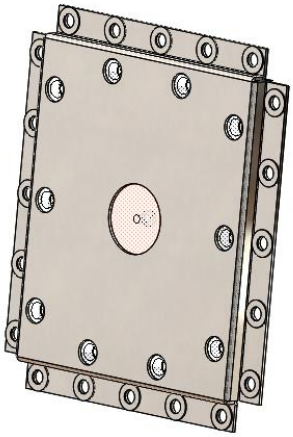

Figure 44. Assembly used for clamping force testing

Figure 44 shows the assembly that is used for the clamping force testing. The exploded view is shown in Figure 45.

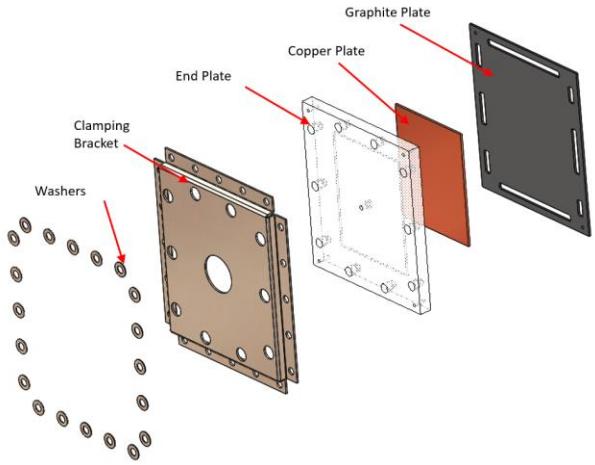

Figure 45 Exploded view of clamping force assembly

The graphite plate is fixed in the assembly as it represents the cell stack. The force is spread out evenly on each of the washers to represent the bolt clamping down on the clamping bracket. The sheet metal used is 12-gauge 304 stainless Steel which is 0.125 inches thick. There will not be a focus on the bending of the metal bolt tabs as the tightness of the bolts in the hole will minimize this.

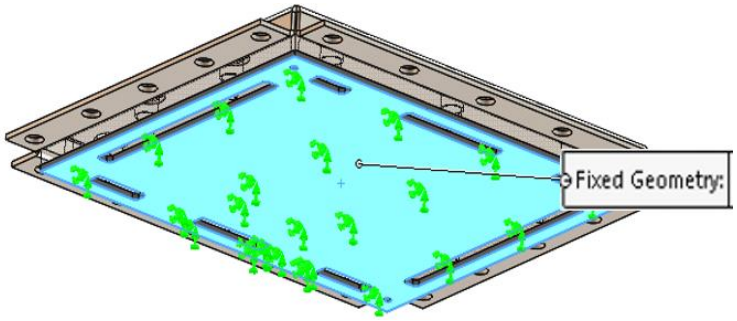

Figure 46 the fixed geometry of the graphite plate

Figure 46 shows how the graphite plate is fixed in all direction, which allows this system to represent the compressive forces on the end plate. This demonstrates how the forces are displaced by countering the forces of the bolts with the compression of the PEMFC stack; this causes the end plate to be in compression without any fixed geometries.

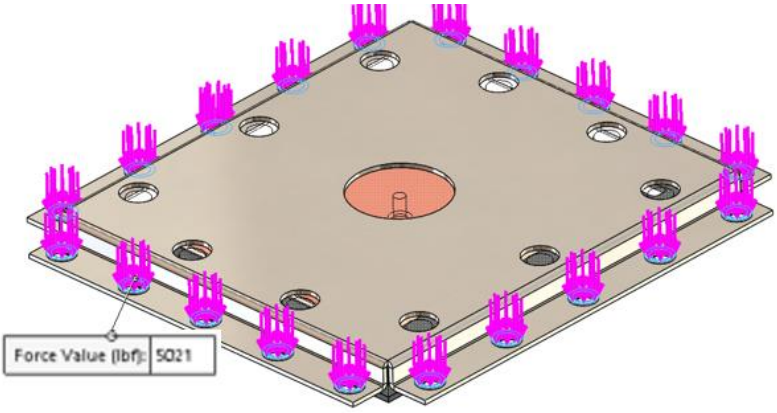

Figure 47 External load setup with 5021 lb_f on each washer

Figure 47 shows the clamping force is evenly spread onto the washer locations to represent the clamping force of the bolts. The force is 5021 lb_f per bolt.

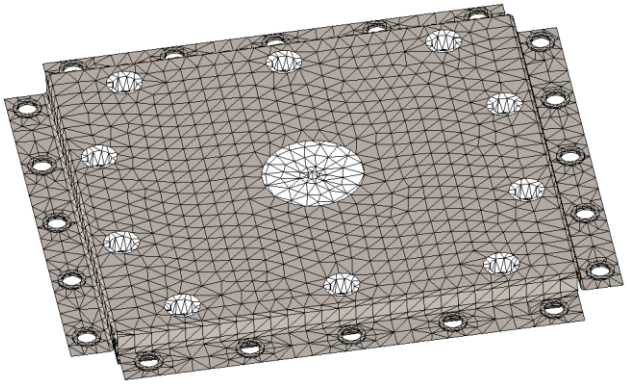

Figure 48 The mesh of the clamping force assembly

Figure 48 shows the mesh of the assembly which is used in the static study.

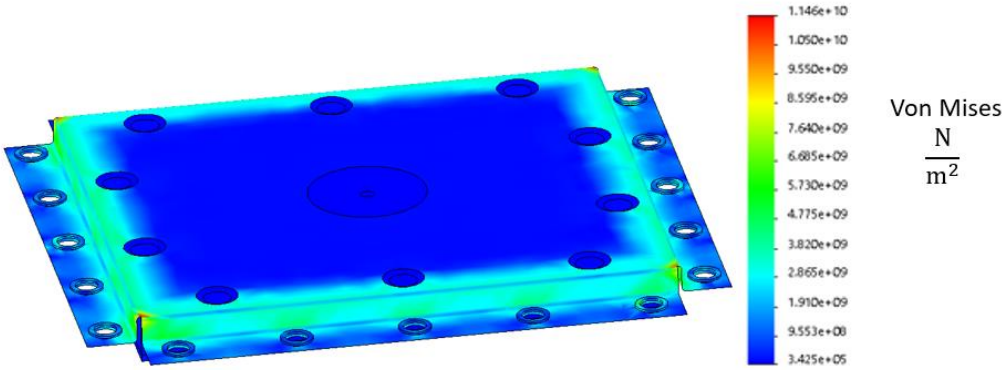

Figure 49 Stress contour plot of the assembly

Figure 49 shows the stress caused by clamping force of the bolts in the assembly. It shows that most of the forces are located around the edge of the end plate. Figure 50 demonstrates how these forces interact with the end plate, which allows for the viewing of the forces entering the stack.

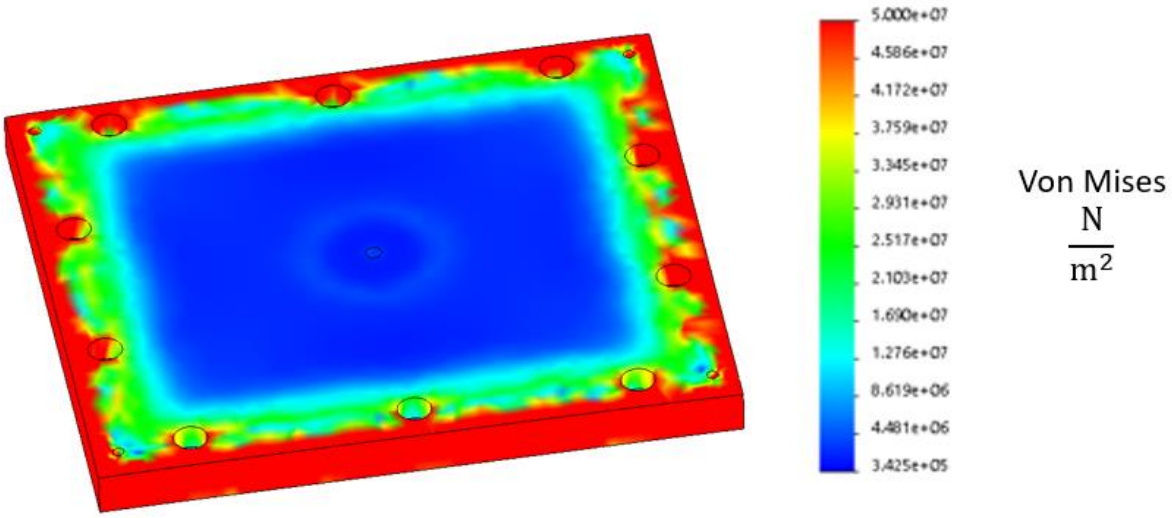

Figure 50 Stress contour plot of the end plate

Figure 50 shows that majority of the force entering the stack is around the edges. As discussed earlier in Chapter 5, this is not the best solution since the largest force in the system is caused by the GDL, which is in the middle of the PEMFC.

8.2 Embossments in clamping bracket

To move the forces from the outside to other locations within the end plates embossments were used. All the emboss plates move the emboss material location by 0.08 inches. The first design is a dimple design. This design has dimples spread out to pinpoint the forces. The dimple design plate is shown in Figure 51.

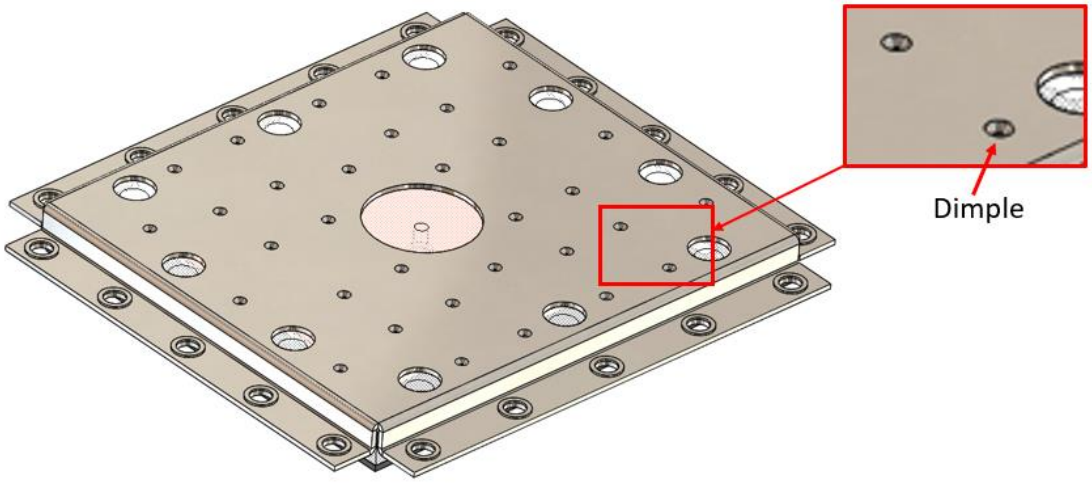

Figure 51 Clamping force assembly with dimple clamping bracket

The dimple clamping bracket test had the same loads and fixtures.

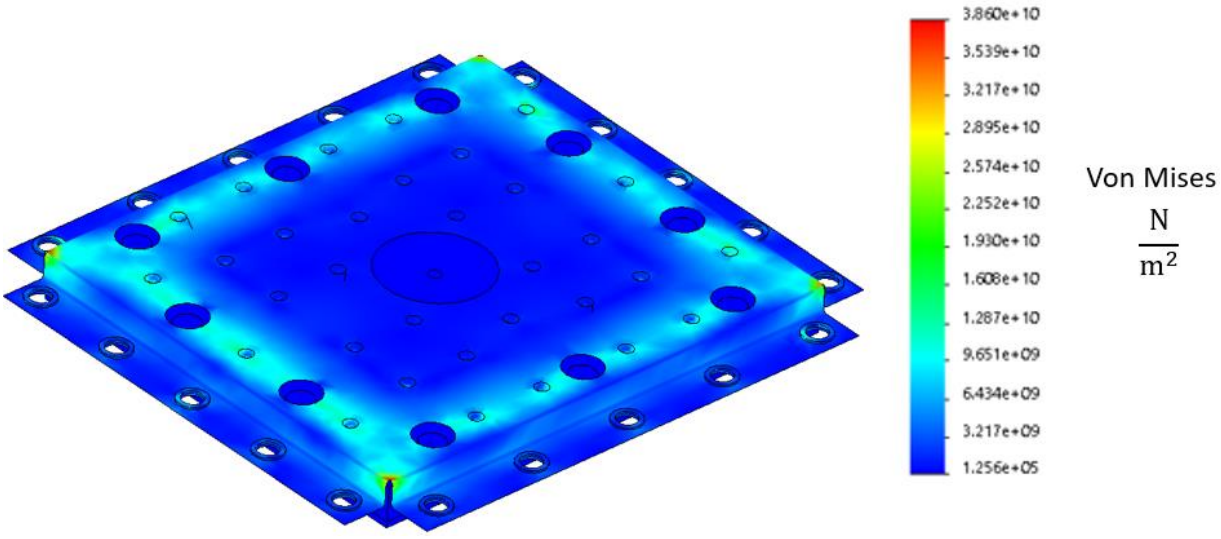

Figure 52 Stress contour plot of assembly with dimple clamping bracket

Figure 52 shows the stress chart of the dimple design. The figure shows that the forces have moved toward the center because the highest forces are no longer focused around the bolts.

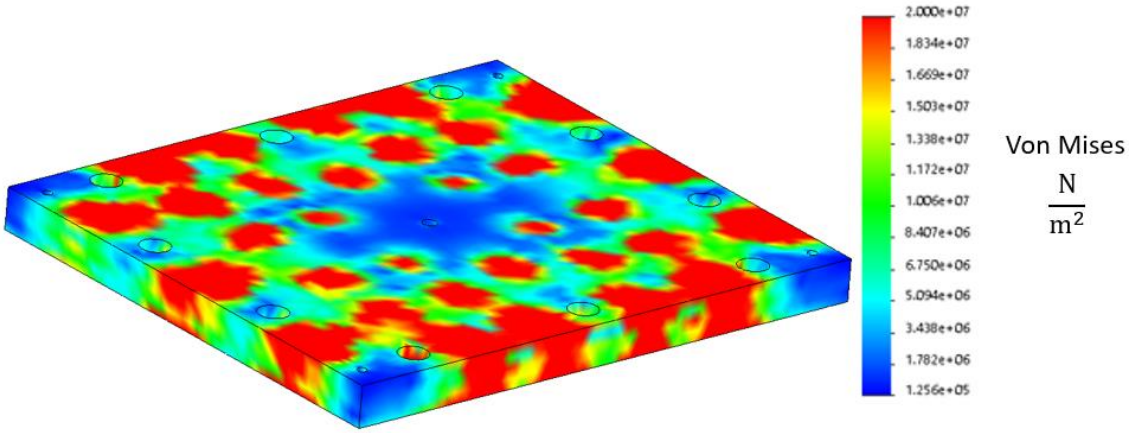

Figure 53 Stress contour plot of the dimple design of the end plate

Based on Figure 53, in the dimple design, the forces acting on the clamping bracket are spread more evenly throughout the end plate. The forces not only are around the edge there are points in the middle as well.

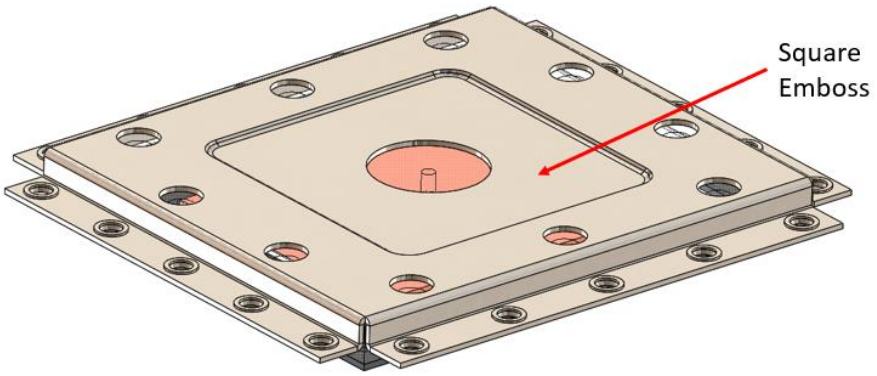

Figure 54 Clamping force assembly with square emboss clamping bracket

Figure 54 shows the second emboss design with a square emboss. The square is in the center of the clamping bracket.

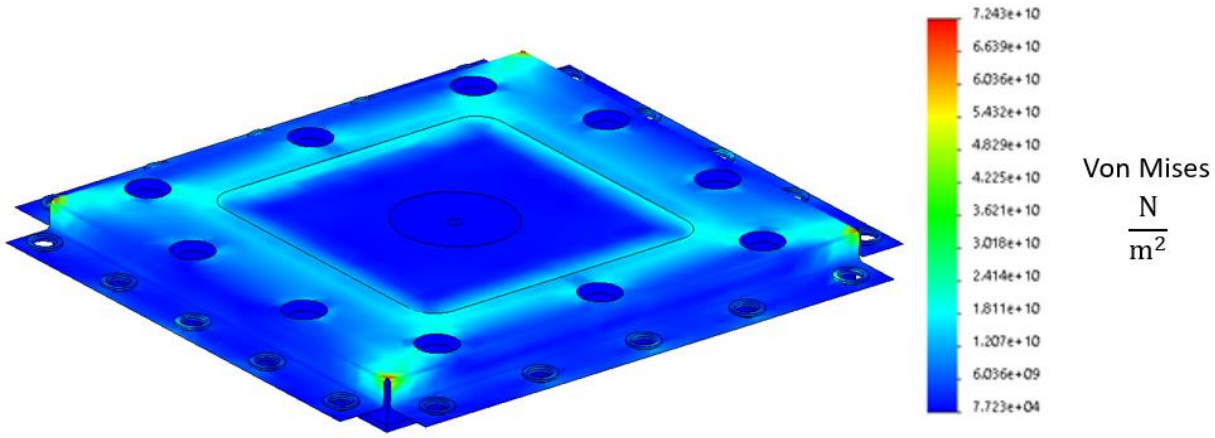

Figure 55 Stress contour plot of assembly with square clamping bracket

In Figure 55, the stress force can be seen with the highest forces starting at the edge of the emboss.

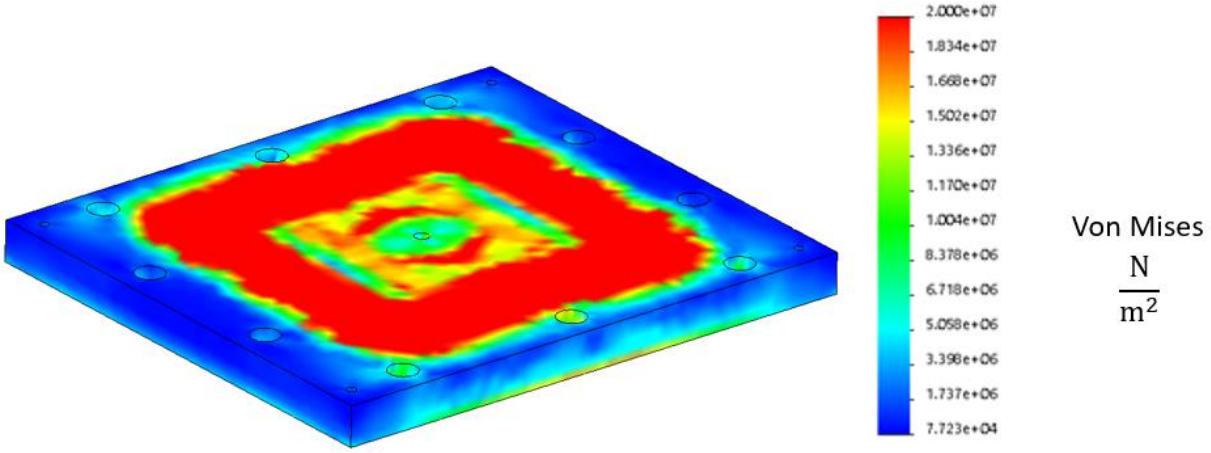

Figure 56 Stress contour plot of the square design of the end plate

Figure 56 shows the stress force focused on the end plate. It shows that the main transfer of forces is located at the bottom of the emboss.

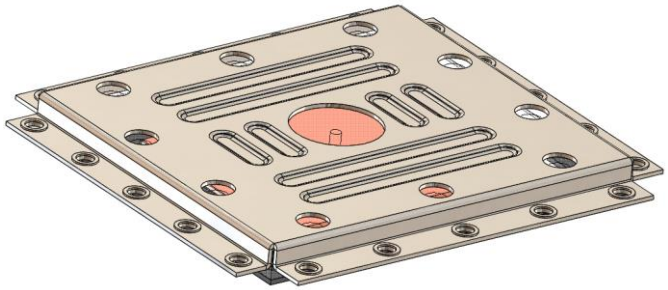

Figure 57 Clamping force assembly with bars element added to the clamping bracket

Figure 57 depicts the third design of the clamping bracket using bar shaped embossing.

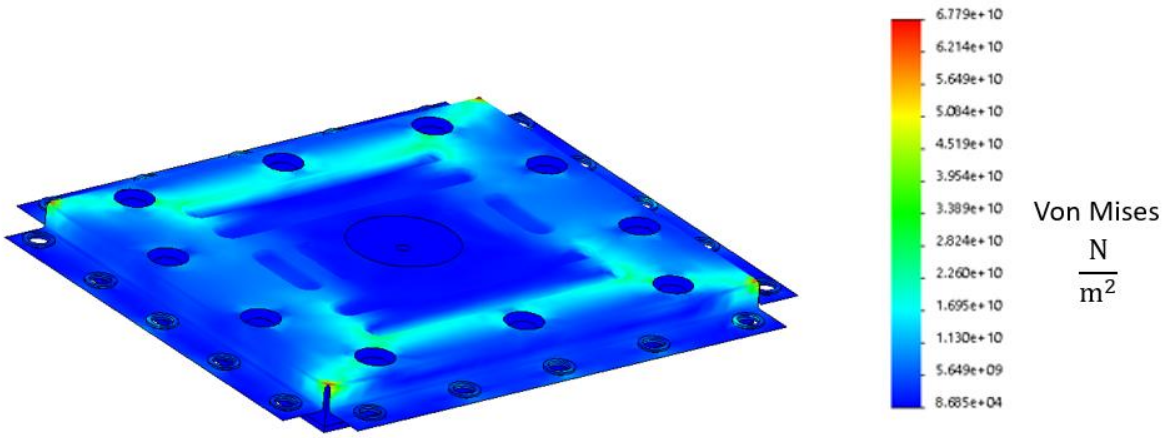

Figure 58 Stress contour plot of assembly with bars clamping bracket

Figure 58 shows how stress can act on the bars on the embossed plate. The forces gather around the outside bars and in all four corners.

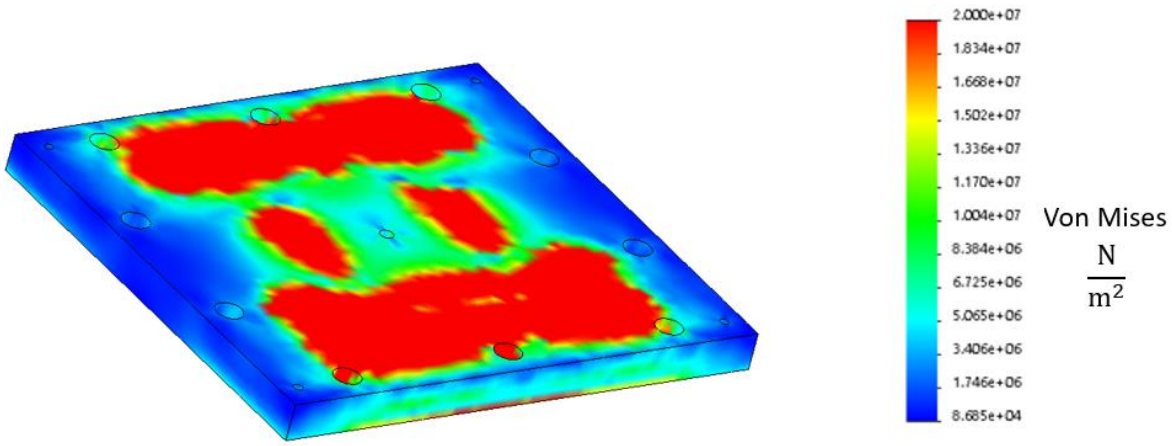

Figure 59 Stress contour plot of the bars design of the end plate

Figure 59 depicts the end plate under the influence of the bar embossed plate. Some of the forces are focused on the center, but much of it is focused around the gas inputs and outlets.

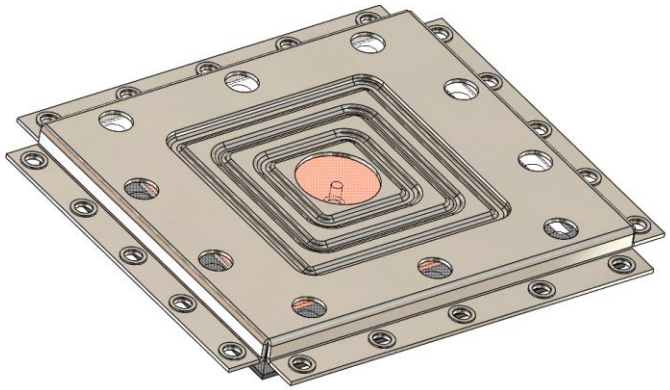

Figure 60 Clamping force assembly with layered square clamping bracket

Figure 60 shows the clamping bracket with layered square emboss.

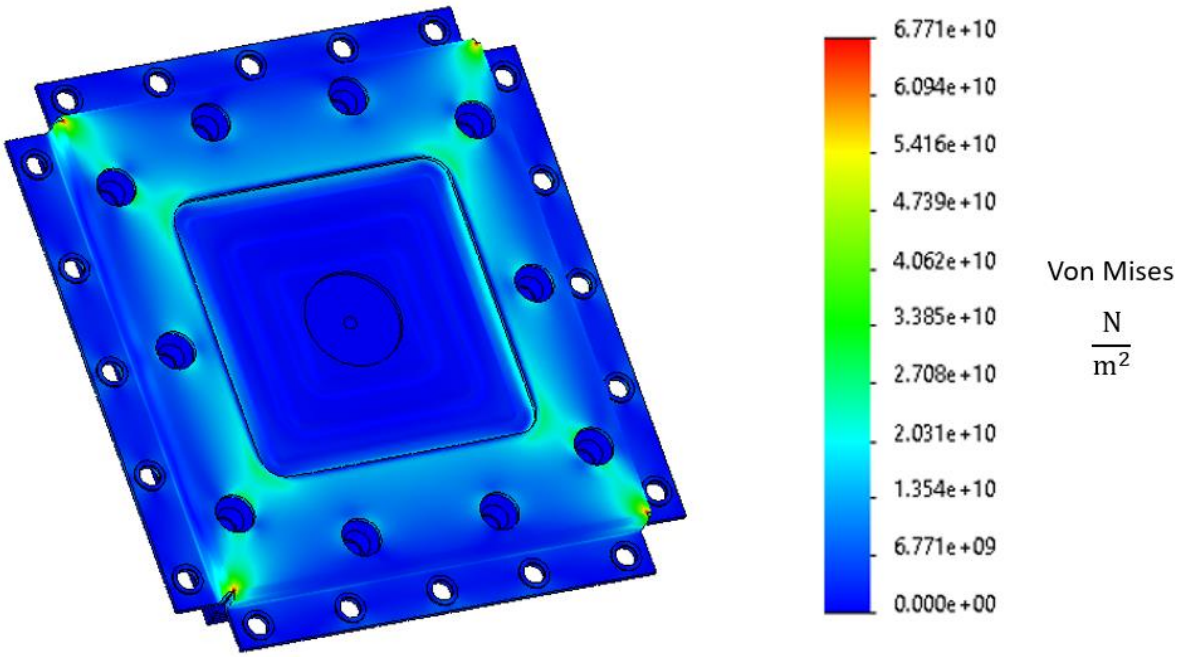

Figure 61 Stress contour plot of assembly with layered square clamping bracket

Figure 61 depicts the stress force on the clamping bracket with layered square emboss. On this design, the forces are very evenly displaced.

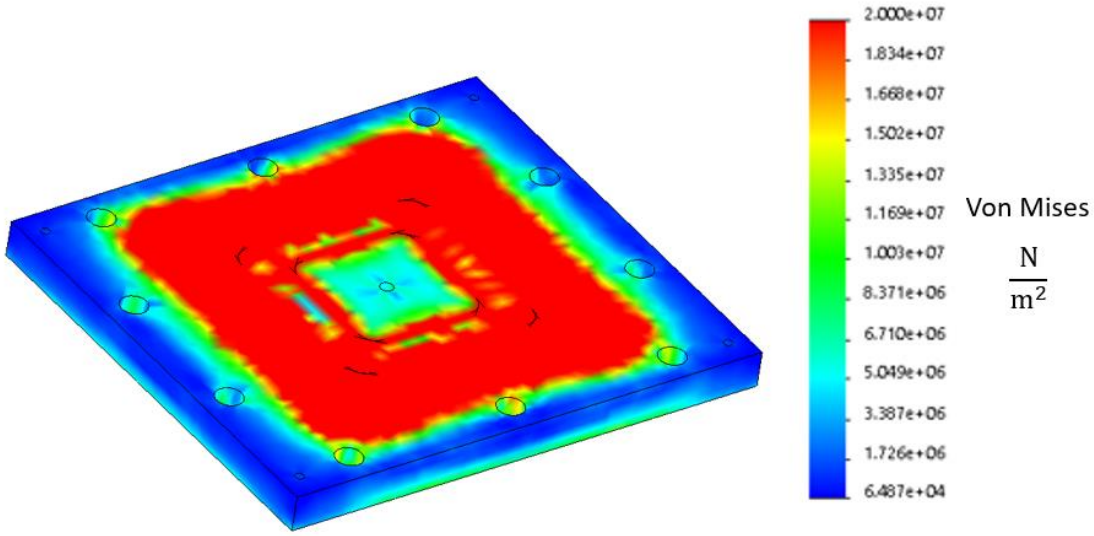

Figure 62 Stress contour plot of the layered square design of the end plate

Figure 62 shows the stress force on the end plate. The force is mostly focused around the area of the GDL, which requires the highest amount of force.

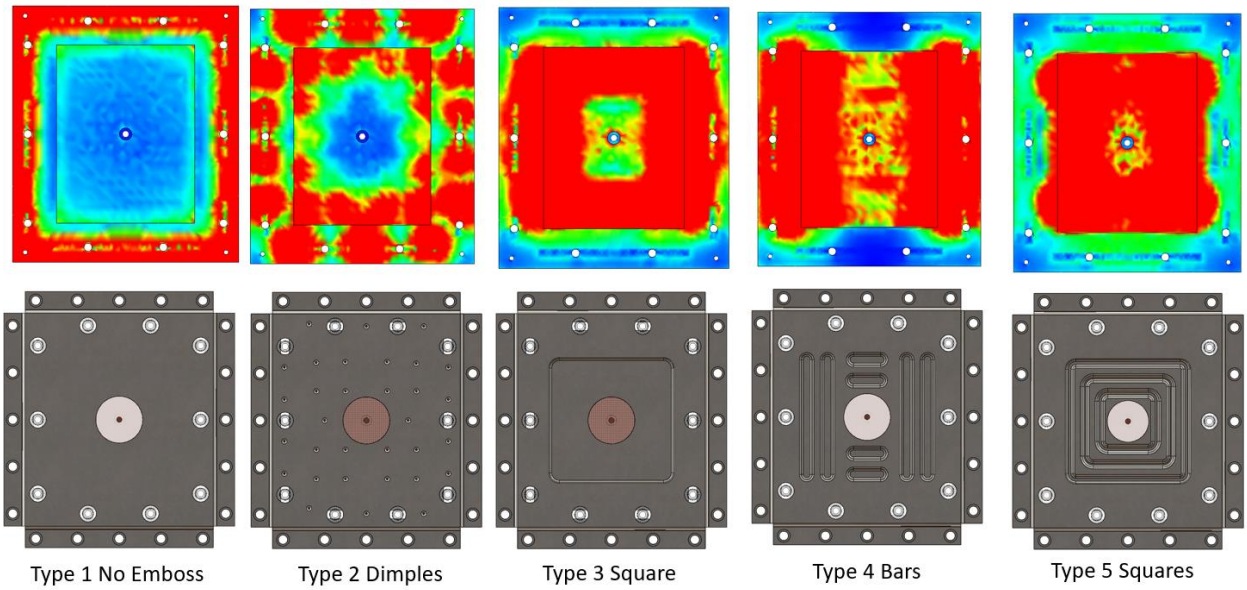

Figure 63 The bottoms of the end plates with the stress forces shown for comparison

Figure 63 depicts the bottoms of the end plates used with each of the clamping brackets. The bottom of the end plate shows how the forces enter the rest of the stack. Each design has a unique stress force layout. Based on the visual inspection of the force layout, type 5 looks like it would be the best due to its ability to focus force on the center of the end plate, over the GDL and to distribute a secondary force over all the gas and cooling input and outputs.

To look into the clamping forces caused by the different clamping plates deeper into the PEMFC stack a second assembly was evaluated. The assembly in Figure 64 shows an assembly with end parts and one full cell.

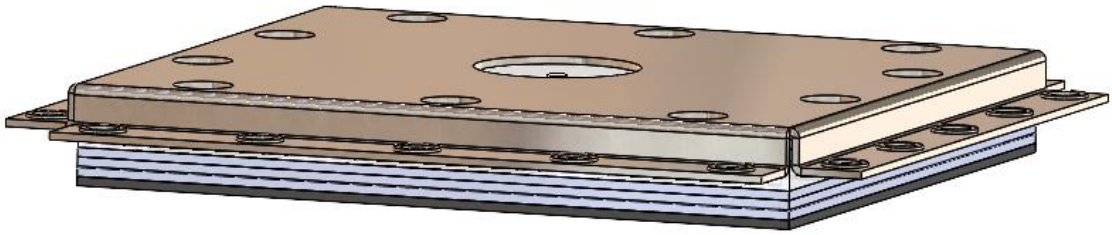

Figure 64 Test assembly of PEMFC stack with end parts and one complete cell

The test assembly parts can be seen in the exploded view in Figure 65.

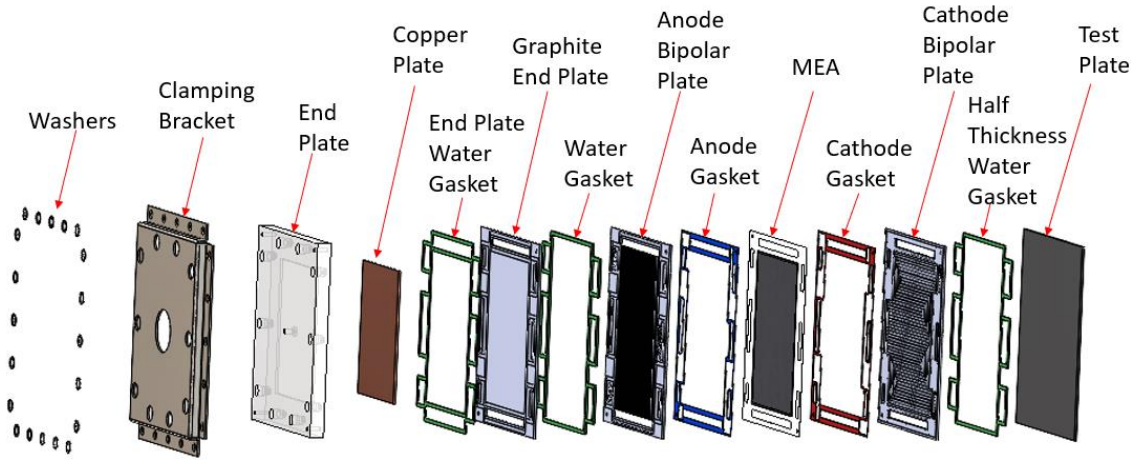

Figure 65 Exploded view of the assembly with one cell

As in the first test the forces of the bolts will be added to the washers and the test plate will be fixed. The test plate is looked at to see how the forces from the bolts travel through the stack to the other side of the cell. The last water gasket thickness is half due to no cutouts in the test plate. Due to the high details and small flow channels in the bipolar plates a very fine mesh had to be used. The mesh for the standard clamping bracket assembly is shown in Figure 66.

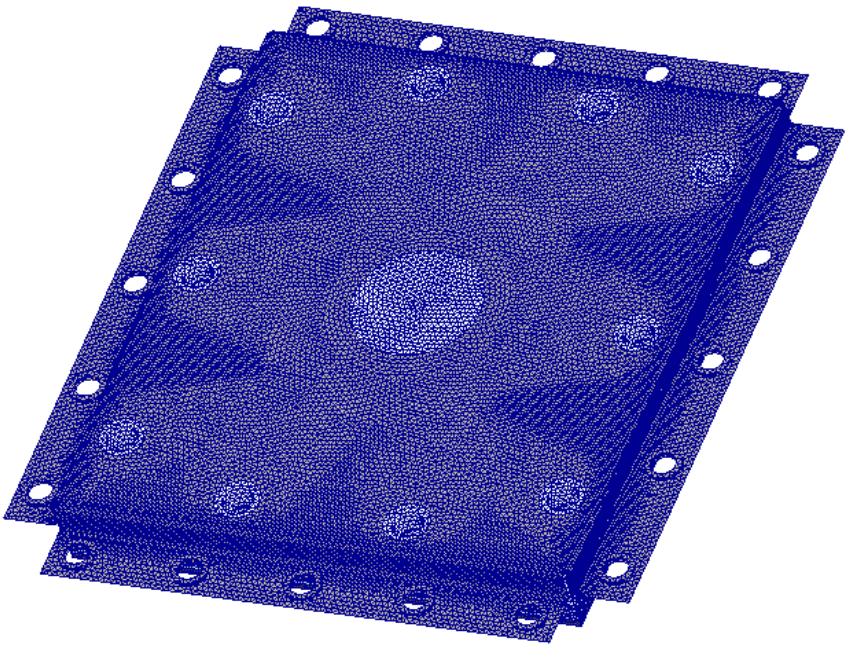

Figure 66 Mesh for the standard clamping plate.

The mesh shown in Figure 66 has minimal element size of .005 inches, 2.37 million nodes, and 1.37 million elements.

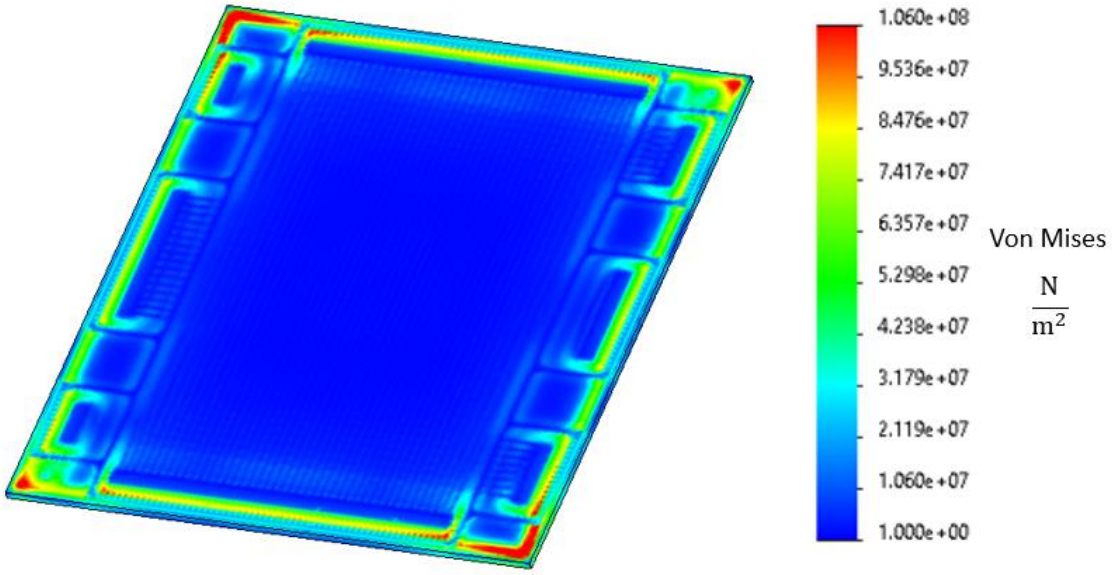

Figure 67 Stress contour plot of the one cell assembly with standard clamping plate

The stress contour plot shown in Figure 67 shows that the forces are focused around the edges which follows the forces shown in the end plate evaluation testing. Another think is found here is the high forces in spots of the plates go high which could cause failure in standard graphite plates. To solve the problem of the high forces POCO graphite plates are recommended which have a maximum compressive strength of 207 MPa (30,000 psi) *(Entegris, 2013)*.

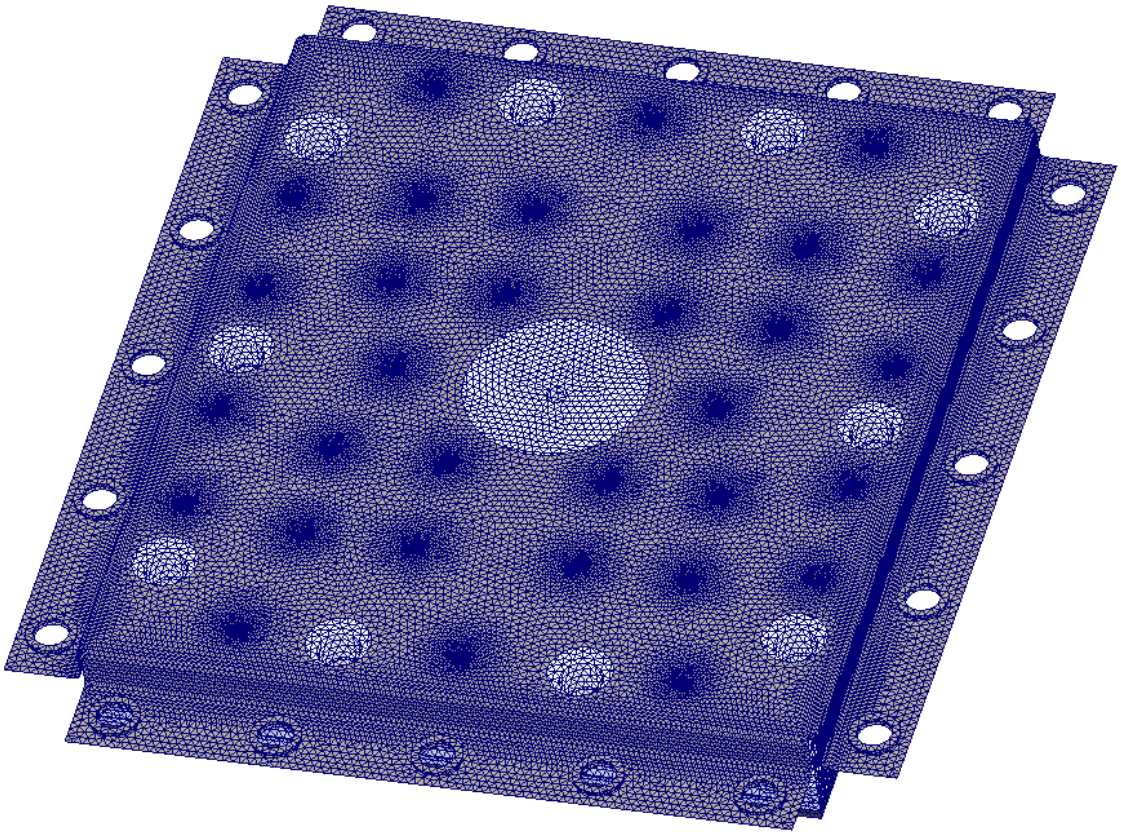

Figure 68 Dimple emboss clamping plate assembly with one cell mesh

Figure 68 shows the mesh for the one cell assembly dimple emboss clamping plate; it has minimal element size of .005 inches, 2.41 million nodes, and 1.39 million elements.

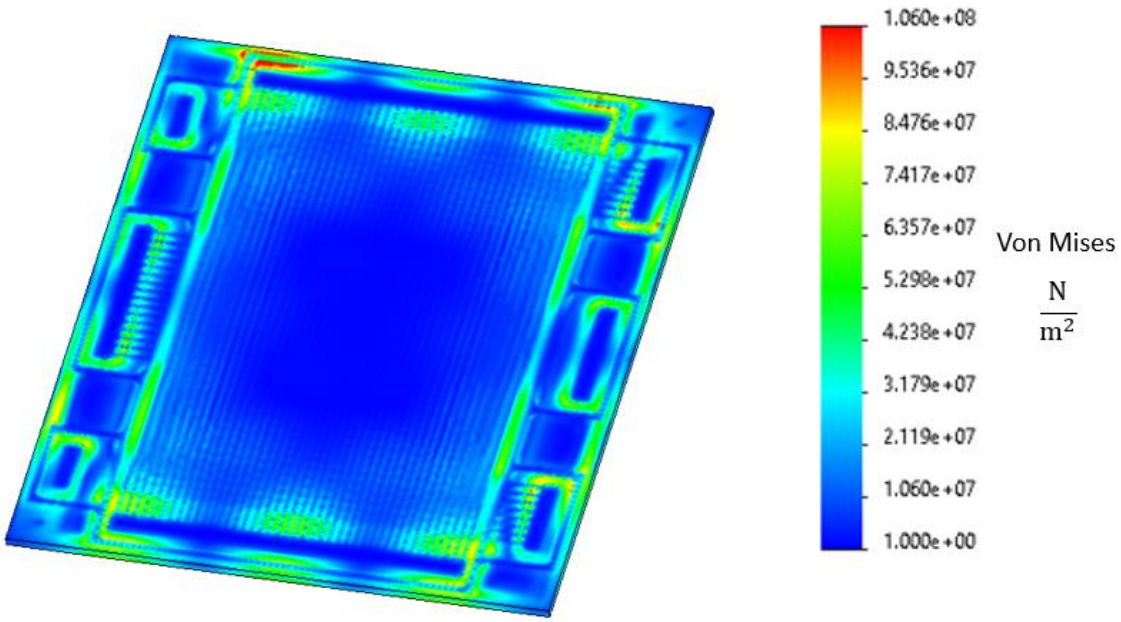

Figure 69 Stress contour plot of the one cell assembly with dimple emboss clamping plate

Figure 69 shows the stress contour plot of the one cell assembly with the dimple emboss clamping plate. The plot shows a very good force spread out over the gaskets and a little bit of coverage over the GDL edges. It does not have coverage over the middle of the GDL.

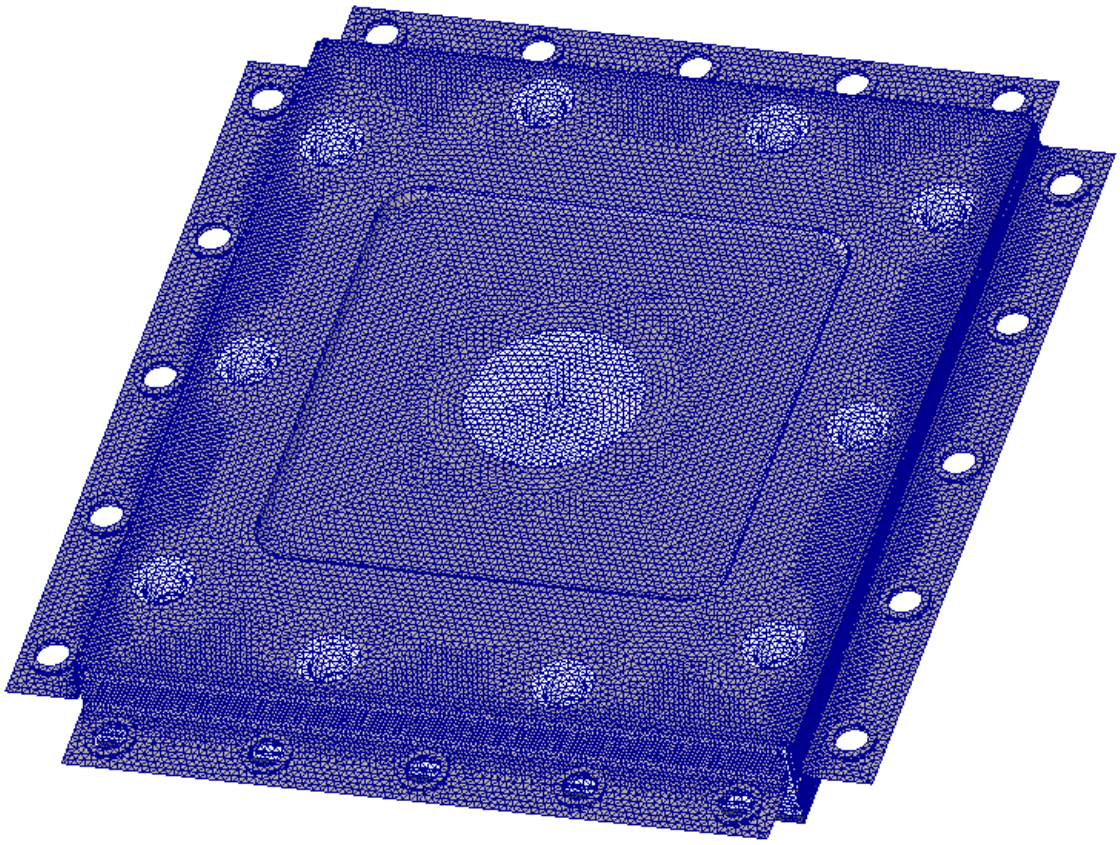

Figure 70 Square emboss plate assembly with one cell mesh

Figure 70 shows the mesh for the one cell assembly square emboss clamping plate; it has minimal element size of .005 inches, 2.37 million nodes, and 1.37 million elements.

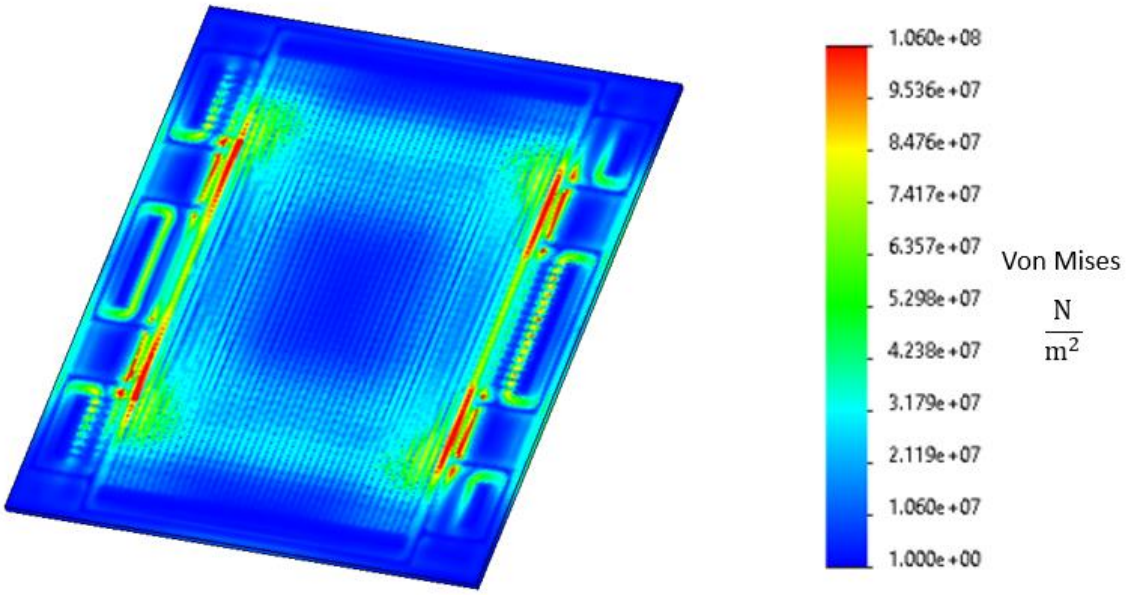

Figure 71 Stress contour plot of the one cell assembly with square emboss clamping plate

Figure 71 shows the stress contour plot of the one cell assembly with the square emboss clamping plate. The plot shows less forces in the gasket locations and more forces at the GDL location.

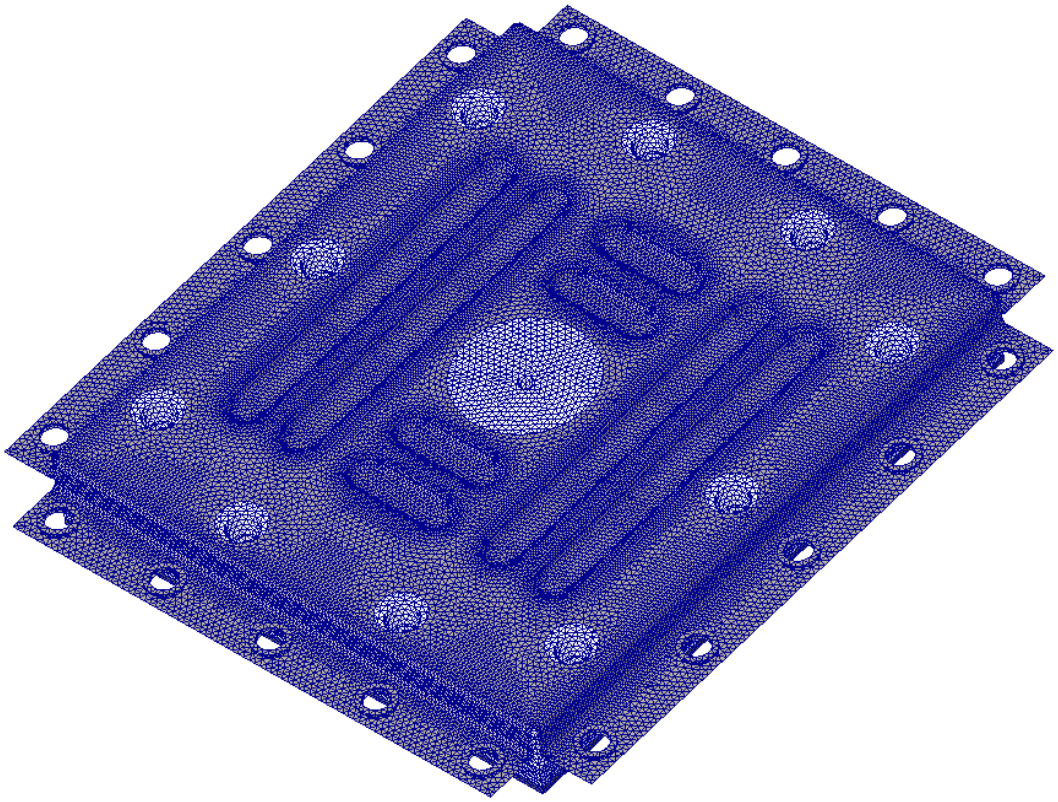

Figure 72 Bars emboss plate assembly with one cell mesh

Figure 72 shows the mesh for the one cell assembly bars emboss clamping plate; it has minimal element size of .005 inches, 2.40 million nodes, and 1.39 million elements.

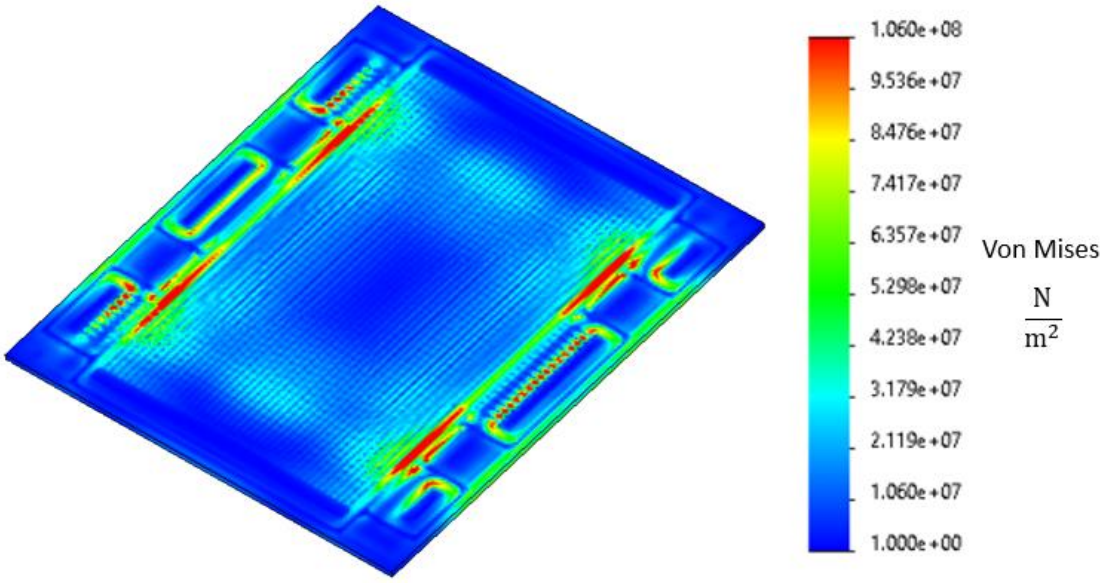

Figure 73 Stress contour plot of the one cell assembly with bars shaped emboss clamping plate

Figure 73 shows the stress contour plot of the one cell assembly with the bar shaped emboss clamping plate. The plot shows forces in the locations of the gas channels and the GDL location, but low forces at the water channels locations.

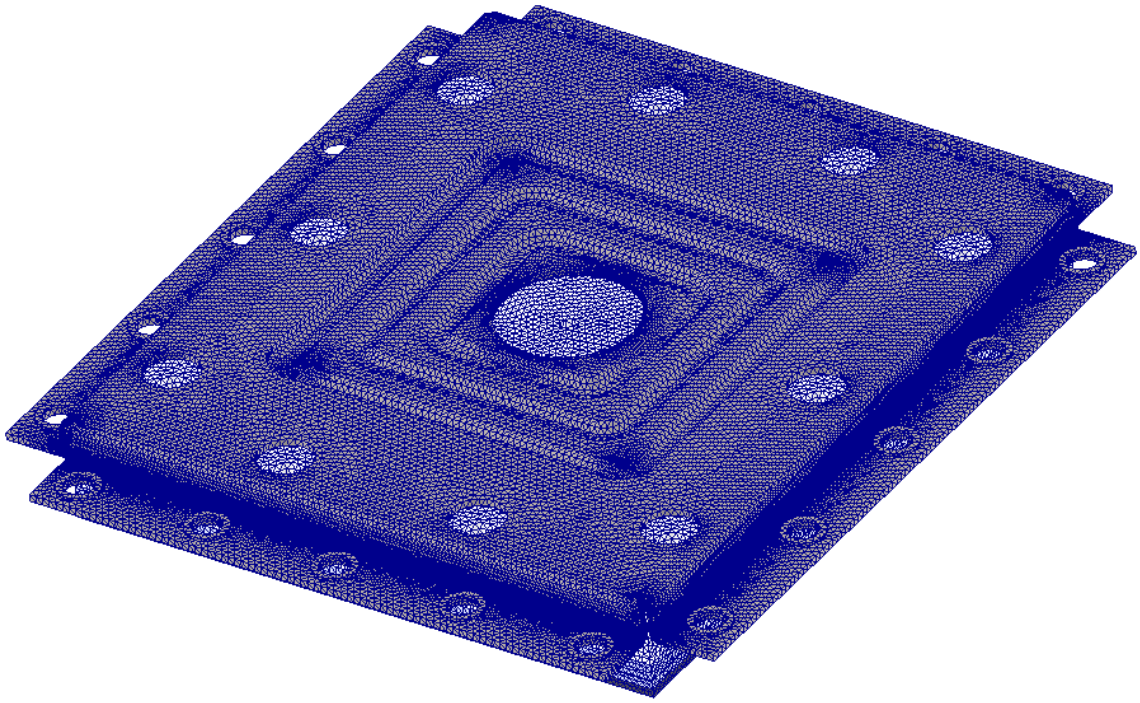

Figure 74 Layered squares emboss plate assembly with one cell mesh

Figure 74 shows the mesh for the one cell assembly layered squares clamping plate; it has minimal element size of .005 inches, 3.92 million nodes, and 2.31 million elements.

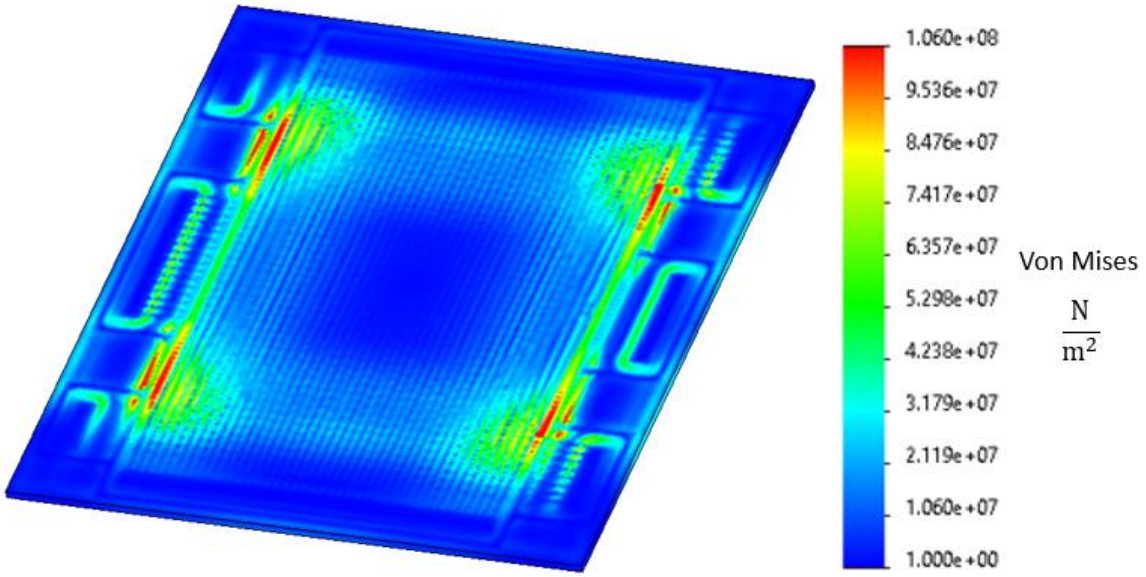

Figure 75 Stress contour plot of the one cell assembly with layered squares shaped emboss clamping plate

Figure 75 shows the stress contour plot of the one cell assembly with the layered square shaped emboss clamping plate. The plot shows forces in the locations of the gas channels and the GDL location, but low forces at the water channels locations and less on the edge of the plate compared to the bars emboss.

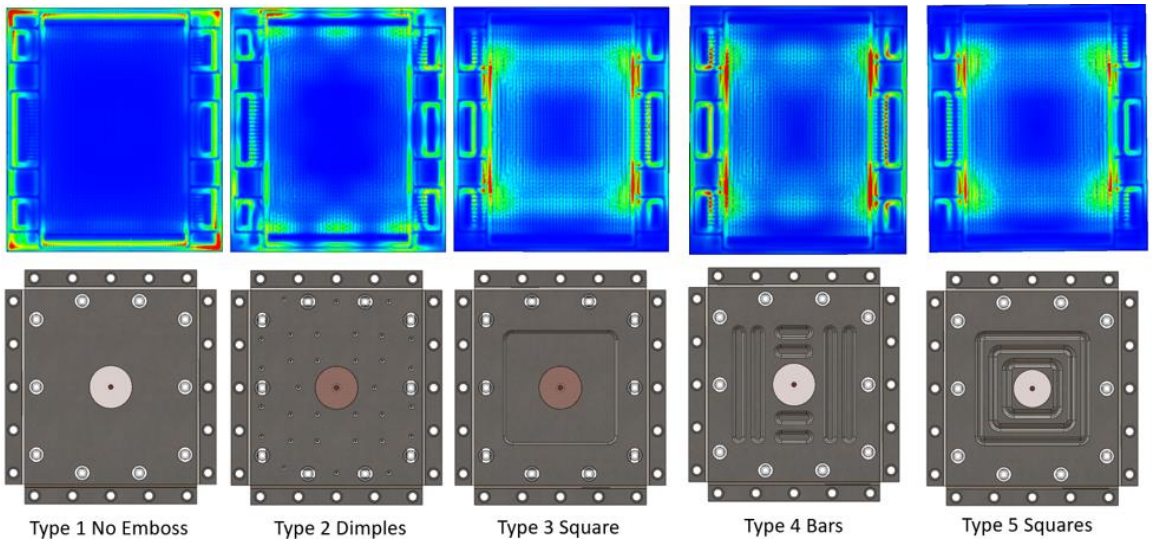

Figure 76 Stress contour plots of the one cell assemblies for comparing

Figure 76 shows the contour plots of the one cell assemblies for comparing. The no emboss plot shows all the forces around the edge with the maximum forces in the corners; this is not a good solution as the corners are a weak point and that the performance of the cell will be reduced as there are not any forces at the GDL area. The dimple emboss removes the maximum forces from the corners and has great force coverage on the gasket locations but has minimum forces at the GDL area. The square emboss plot shows more forces focused around the GDL with the maximum on the edges of the GDL but has very low forces at the water channel locations. The bars emboss plot shows results like the square but has a higher concentration of forces in the maximum areas and less focused on the center area. The layers of squares emboss has a similar plot to the square and the bars but has less of a high stress area which is faded out more over the GDL. Based on the visual inspections of the stress plots the one that is recommended will be the layered squares due to forces in the GDL and the smaller areas of high forces which will reduce the chances of cracking a bipolar plate.

CONCLUSIONS

The results from simulations and calculations done in Solidworks can influence the design of a PEMFC and the stack during the design stage. The information found in this project can help support or reject design choices in the bi-polar plate, cooling systems, end plate, and clamping force designs.

The CFD flow simulations of the gas flow channels estimated the improvements in the flow caused by utilizing the dual outlet design, which decreased the channel length by 9.37 inches. The performance of the channel not only increased flowrate by 53.95% but also increased the velocity by 15.37% with the same active area. This solution could allow larger PEMFC to be designed without the limitations of long flow channels. The radius added to the flow channel had a small improvement to the performance but could be larger if water pooling was evaluated in the design.

Evaluation of the gaskets and thickness was completed with the use of a Compression Force Deflection graph and CAD area calculations. The amount of force for the gaskets was found for each of the gaskets. During the processes of calculating the required forces, it became apparent that the area of the gasket needed to be decreased if possible. By evaluating these forces and making the changes, the overall required force was reduced by 15,754.8 lbf. Based on the large force needed to clamp the PEMFC stack assembly, larger bolts are needed than used in the original model. The force per bolt as designed is 10,042.58 lbs.

Calculating the compression thickness of the gasket can be used to set the depth of the bi-polar plate gasket cutouts to allow for the use of standard thickness material sheets for the die cut process. For low productions, die cut gaskets will save cost over the need for injection molded gaskets for custom thicknesses.

Cooling channel simulations allowed improvement in the overall system design. The cooling flowrate is important for designing a system that can cycle the minimal required amount of cooling water and potentially reuse the water. The CFD also gives the volume of water in the system, which is helpful in system design. Based on the findings, the system needs 216 mL/min. The radius in the cooling channel had a small effect.

The clamping bracket designs can greatly change the effect of the clamping force. The challenge of relocating the clamping force to the center of the end plate can be done with embossments in the bracket. The forces caused by the layered square emboss show great promise. With this design the main force is focused on the GDL, with the secondary force on the gas collector locations, and a reduced area of maximum stress in the cells.

RECOMMENDATIONS

Future work on this project should focus on building and testing the dual outlet design as the simulations show that this design should greatly increase the performance of the fuel cell. The design of embossments being used on the clamping brackets are promising as well. More emboss clamping bracket designs should be examined to improve its design to maximize the benefit of force relocating.

Another future development that could help improve PEMFC designs is to create a database with Compression Force Deflection based on material and manufacture.

REFERENCES

Alizadeh, E., Ghadimi, M., Barzegari, M., Momenifar, M., & Saadat, S. (2017). Development of contact pressur distribution of PEM fuel cell's MEA using novel clamping mechanism. *Energy 131*, 92-97.

Alrweq, A. A. (2018). Proton Exchange Membrane Fuel Cells - Design, Modelling and Performance Assessment Techniques. In A. A. Alrweq, *Proton Exchange Membrane Fuel Cells - Design, Modelling and Performance Assessment Techniques* (p. 4). Cham, Switzerland: Springer.

Atyabi, S. A., Afshari, E., Wongwises, S., Yan, W.-M., Hadjadj, A., & Shadloo, M. S. (2019). Effects of assembly pressure on PEM fuel cell performance by taking into accounts electrical and thermal contact resistances. *Energy 179*, 490-501.

Carcadea, E. I. (2020). Effects of geometrical dimensions of flow channels of a large-active-area PEM fuel cell: A CFD study. *International Journal of Hydrogen Energy*.

Dictionary.com, LLC. (2021, 12 1). *dictionary.com*. Retrieved from dictionary.com: https://www.dictionary.com/browse/emboss

Electrical Academia. (n.d.). *Fuel Cell: Types, Working, Applications, Advantages & Disadvantages*. Retrieved from Electrical Academia: https://electricalacademia.com/renewable-energy/fuel-cell-types-working-applications-advantages-disadvantages/

Engineering Toolbox. (2020, 7 29). *US Bolts - Tensile Strenght and Proof Loads*. Retrieved from Engineeringtoolbox.com: https://www.engineeringtoolbox.com/us-bolts-tensile-proof-load-d_2066.html

Entegris. (2013, May). *Properties and Characteristics of Graphite.* Retrieved from www.entegris.com: https://www.entegris.com/content/dam/web/resources/brochures/brochure-properties-and-characteristics-of-graphite-7329.pdf

Freudenberg. (2020, 7 12). *Freudenberg Gas Difussion Layers Technical Data.* Retrieved from fuelcellcomponents.freudenberg-pm.com: https://fuelcellcomponents.freudenberg-pm.com/-/media/Files/fuelcellcomponents,-d-,freudenbergpm,-d-,com/FPM_technical_data_sheet_gdl_ENG_2018-07-04.pdf

Hosch, W. L. (2020, 12 6). *Navier-Stokes Equation*. Retrieved from Britannica: https://www.britannica.com/science/Navier-Stokes-equation

Irmscher, P., Qui, D., JanBen, H., Lehnert, W., & Stolten, D. (2019). Impact of gas diffusion layer mechanics on PEM fuel cell performance. *International Journal of Hydrogen Energy 44*, 23406-23415.

James Larminie, A. D. (2003). *Fuel Cell System Explained, Second Edition.* John Wiley & Sons.

Lin, C.-W., Chien, C.-H., Tan, J., Chao, Y.-J., & Van Zee, J. W. (2011). Dynamic mechanical characteristics of five elastomeric gasket materials aged in a simulated and an accelerated PEM fuel cell environmen. *International Journal of Hydrogen Energy, Vol 36*, 6756-6767.

Mentor. (2018). *FloEFD Technical Reference Software Version 17 rev19122017.* Retrieved from www.smart-fem.de: https://www.smart-fem.de/media/floefd/TechnicalReferenceV17.pdf

NASA Glenn Research Center. (2020, 11 22). *Navier-Stokes Equation.* Retrieved from Glenn Rearch Center NASA: https://www.grc.nasa.gov/WWW/k-12/airplane/nseqs.html

National Museum of American History, S. I. (2021, 11 3). *Fuel Cells*. Retrieved from https://americanhistory.si.edu: https://americanhistory.si.edu/fuelcells/basics.htm

Office of Energy Efficiency & Renewable Energy. (2020, 2 26). *Hydrogen Production Processes*. Retrieved from Energy.gov: https://www.energy.gov/eere/fuelcells/hydrogen-production-processes

Office of Energy Efficiency & Renewable Energy. (2020, 2 26). *Hydrogen Production: Natural Gas Reforming*. Retrieved from www.energy.gov: https://www.energy.gov/eere/fuelcells/hydrogen-production-natural-gas-reforming

Parker Hannifin Corporation - TechSeal Division. (2020, 8 6). *ParFab Design Guide.* Retrieved from Parker.com: https://www.parker.com/literature/TechSeal%20Division/Literature%20PDF%20Files/TSD%205420_ParFab%20Design%20Guide_2014.pdf

Subachkin, D. A., Dumnov, D. G., & Sobachkin, D. A. (2014, February). *Numerical Basis of CAD-Embedded CFD White Paper.* Retrieved from solidworks.com:

https://www.solidworks.com/sw/docs/Flow_Basis_of_CAD_Embedded_CFD_Whitepaper.pdf#

Tan, J., Chao, Y., Li, X., & Van Zee, J. (2007). Degradation of silicone rubber under compression in a simulated PEM fuel cell environment. *Journal of Power Sources 172*, 782-789.

Tan, J., Chao, Y., Wang, H., Gong, J., & Van Zee, J. (2009). Chemical and mechanical stability of EPDM in a PEM fuel cell environment. *Polymer Degradation and Sability*, 2072-2078.

U.S. Energy Information Administration. (2020, February 11). *Short-term Energy outlook*. Retrieved from www.eia.gov: https://www.eia.gov/outlooks/steo/report/electricity.php

Wilberforce, T. H., & Ogungbemi, E. (2019). A comprehensive study of the effect of bipolar plate (BP) geometry design on the performance of proton exchange membrane (PEM) fuel cells. *Renewable and Sustainable Energy Reviews*, 236-260.

APPENDIX

A.1 CFD how it works

The CFD Solidworks software uses equations to find the solutions for fluid and heat simulations. The equations are based on the works of Claude-Louis Navier, Sir George Stokes, and Leonhard Euler and are known as the Navier-Stokes equations. (Hosch, 2020) The first equation is the Mass Continuity Equation (NASA Glenn Research Center, 2020).

$$\frac{\partial \rho}{\partial t} + \frac{\partial(\rho u)}{\partial x} + \frac{\partial(\rho v)}{\partial y} + \frac{\partial(\rho w)}{\partial w} = 0 \tag{5}$$

Equation 2 is the Mass Continuity Equation where *x*, *y*, and *z* are a directional vector or distance. The velocity vectors are *u*, *v*, and *w*. The density of the fluid is noted by ρ and *t* is time. (Subachkin, Dumnov, & Sobachkin, 2014) show a reduced equation based on the x direction and is show below as Equation 3.

$$\frac{\partial \rho}{\partial t} + \frac{d(\rho u_i)}{dx_i} = 0 \tag{6}$$

The second Navier-Strokes equation is the Momentum Equation which is broken up into the x, y, and z directions. X direction is Equation 4, y- direction is Equation 5, and z direction is Equation 6 (NASA Glenn Research Center, 2020):

$$\frac{\partial(\rho u)}{\partial t} + \frac{\partial(\rho u^2)}{\partial x} + \frac{\partial(\rho uv)}{\partial y} + \frac{\partial(\rho uw)}{\partial z} = -\frac{\partial \rho}{\partial x} + \frac{1}{Re_r}\left[\frac{\partial \tau_{xx}}{\partial x} + \frac{\partial \tau_{xy}}{\partial y} + \frac{\partial \tau_{xz}}{\partial z}\right] \tag{7}$$

$$\frac{\partial(\rho v)}{\partial t} + \frac{\partial(\rho uv)}{\partial x} + \frac{\partial(\rho v^2)}{\partial y} + \frac{\partial(\rho vw)}{\partial z} = -\frac{\partial \rho}{\partial y} + \frac{1}{Re_r}\left[\frac{\partial \tau_{xy}}{\partial x} + \frac{\partial \tau_{yy}}{\partial y} + \frac{\partial \tau_{yz}}{\partial z}\right] \tag{8}$$

$$\frac{\partial(\rho w)}{\partial t} + \frac{\partial(\rho uw)}{\partial x} + \frac{\partial(\rho vw)}{\partial y} + \frac{\partial(\rho w^2)}{\partial z} = -\frac{\partial \rho}{\partial z} + \frac{1}{Re_r}\left[\frac{\partial \tau_{xz}}{\partial x} + \frac{\partial \tau_{yz}}{\partial y} + \frac{\partial \tau_{zz}}{\partial z}\right] \quad (9)$$

Where Re is the Reynolds Number and τ is the stress. Solidworks references a modified version in the x-direction shown in Equation 6 (Subachkin, Dumnov, & Sobachkin, 2014):

$$\frac{\partial(\rho u_i)}{\partial i} + \frac{\partial}{\partial x_j}\left(\rho u_i u_j\right) + \frac{\partial P}{\partial x_i} = \frac{\partial}{\partial x_j}\left(\tau_{ij} + \tau_{ij}^R\right) + S_i \quad (10)$$

The variables information is missing in the Solidworks reference document but can be found in the Mentor FloEFD Technical Reference (Mentor, 2018) as the Solidworks CFD software is created and maintained by Mentor. Where P is pressure and S_i is a mass-distributed external force per unit mass is shown in Equation 7.

$$S_i = S_i^{porous} + S_i^{gravity} + S_i^{rotation} \quad (11)$$

Where S_i^{porous} is porous media resistance, $S_i^{rotation}$ is the coordinate system's rotation, and $S_i^{gravity}$ is a gravitational acceleration component, as shown in Equation 8.

$$S_i^{gravity} = -\rho g_i \quad (12)$$

Where g_i is the gravitational acceleration component. The last Navier-Stokes Equation is the Conservation of Energy Equation shown as Equation 9 (NASA Glenn Research Center, 2020):

$$\frac{\partial(E_T)}{\partial T}+\frac{\partial(uE_T)}{\partial x}+\frac{\partial(vE_T)}{\partial y}+\frac{\partial(wE_t)}{\partial z}=-\frac{\partial(up)}{\partial x}-\frac{\partial(vp)}{\partial y}-\frac{\partial(wp)}{\partial z}-\frac{1}{Re_rP_r}\left[\frac{\partial q_x}{\partial x}+\frac{\partial q_y}{\partial y}+\frac{\partial q_z}{\partial z}\right]+$$

$$\frac{1}{Re_r}\left[\frac{\partial}{\partial x}\left(u\tau_{xx}+v\tau_{xy}+w\tau_{xz}\right)+\frac{\partial}{\partial y}\left(u\tau_{xy}+v\tau_{yy}+w\tau_{yz}\right)+\frac{\partial}{\partial z}\left(u\tau_{xz}+v\tau_{yz}+w\tau_{zz}\right)\right] \quad (13)$$

Where q is the heat flux, E_T is total energy, and Pr is the Prandtl Number. Solidworks references a modified version in the x-direction, shown in Equation 10 (Subachkin, Dumnov, & Sobachkin, 2014):

$$\frac{\partial\rho H}{\partial t}+\frac{\partial\rho u_i H}{\partial x_i}=\frac{\partial}{\partial x_i}\left(u_j\left(\tau_{ij}+\tau_{ij}^R\right)+q_i\right)+\frac{\partial\rho}{\partial t}-\tau_{ij}^R\frac{\partial u_i}{\partial x_j}+\rho\varepsilon+S_iu_i+Q_H \quad (14)$$

Where Q_H is a heat source or sink per unit volume, q_i is the diffusive heat flux, and H is shown in Equation 11. (Mentor, 2018)

$$H=h+\frac{u^2}{2}+\frac{5}{3}k-\frac{\Omega^2r^2}{2}-\sum_m h_m^0\,y_m \quad (15)$$

Where Ω is an angular velocity, r is the distance from a point to rotation axis, h_m^0 is an individual thermal enthalpy, h is the thermal enthalpy, k is the kinetic energy of turbulence, and y_m is a concentration of the mixture component, τ_{ij} the viscous shear stress tensor for Newtonian fluids is found using Equation 12. (Mentor, 2018)

$$\tau_{ij}=\mu\left(\frac{\partial u_i}{\partial x_j}+\frac{\partial u_j}{\partial x_i}-\frac{2}{3}\delta_{ij}\frac{\partial u_k}{\partial x_k}\right) \quad (16)$$

τ_{ij}^R the Reynolds-stress tensor is found by using Equation 13.

$$\tau_{ij}^{R} = \mu_t \left(\frac{\partial u_i}{\partial x_j} + \frac{\partial u_j}{\partial x_i} - \frac{2}{3}\delta_{ij} \frac{\partial u_k}{\partial x_k} \right) - \frac{2}{3}\rho k \delta_{ij} \quad (17)$$

Where δ_{ij} is the Kronecker delta function, μ is the dynamic viscosity coefficient, k is the turbulent kinetic energy, and μ_t is the turbulent eddy viscosity coefficient, which is found using Equation 14 (Mentor, 2018):

$$\mu_t = f_\mu \frac{C_\mu \rho k^2}{\varepsilon} \quad (18)$$

Where ε is the turbulent dissipation and f_μ is the turbulent viscosity factor that is found using Equation 15 (Mentor, 2018):

$$f_\mu = \left[1 - exp\left(-0.0165 R_y\right)\right]^2 * \left(1 + \frac{20.5}{R_T}\right) \quad (19)$$

Where

$$R_T = \frac{\rho k^2}{\mu \varepsilon} \quad (20)$$

$$R_y = \frac{\rho \sqrt{k} y}{\mu} \quad (21)$$

Where y is the distance from the wall.

A.2 Part Drawings

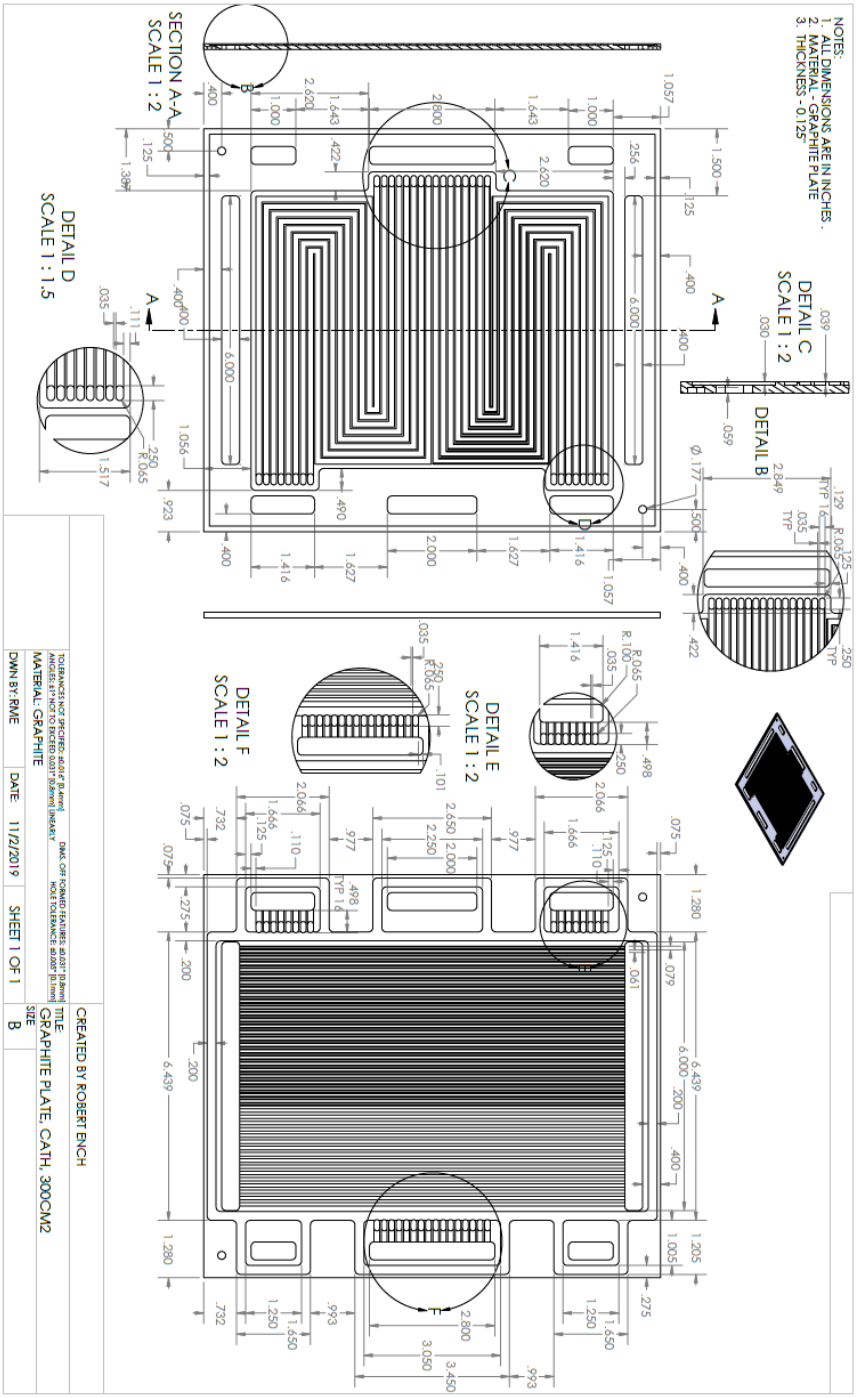

Figure 77 Cathode bipolar plate drawing

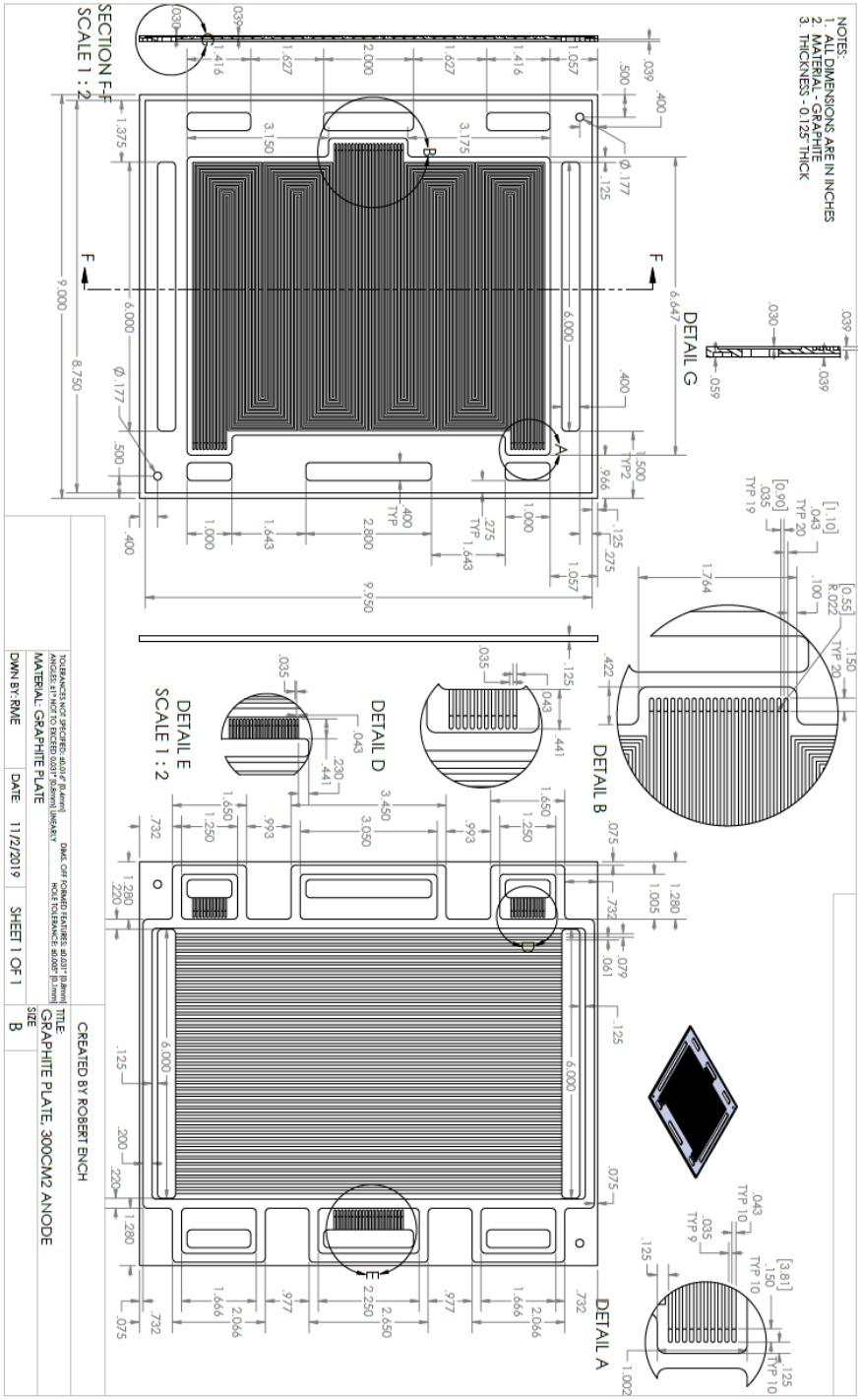

Figure 78 Anode bipolar plate drawing

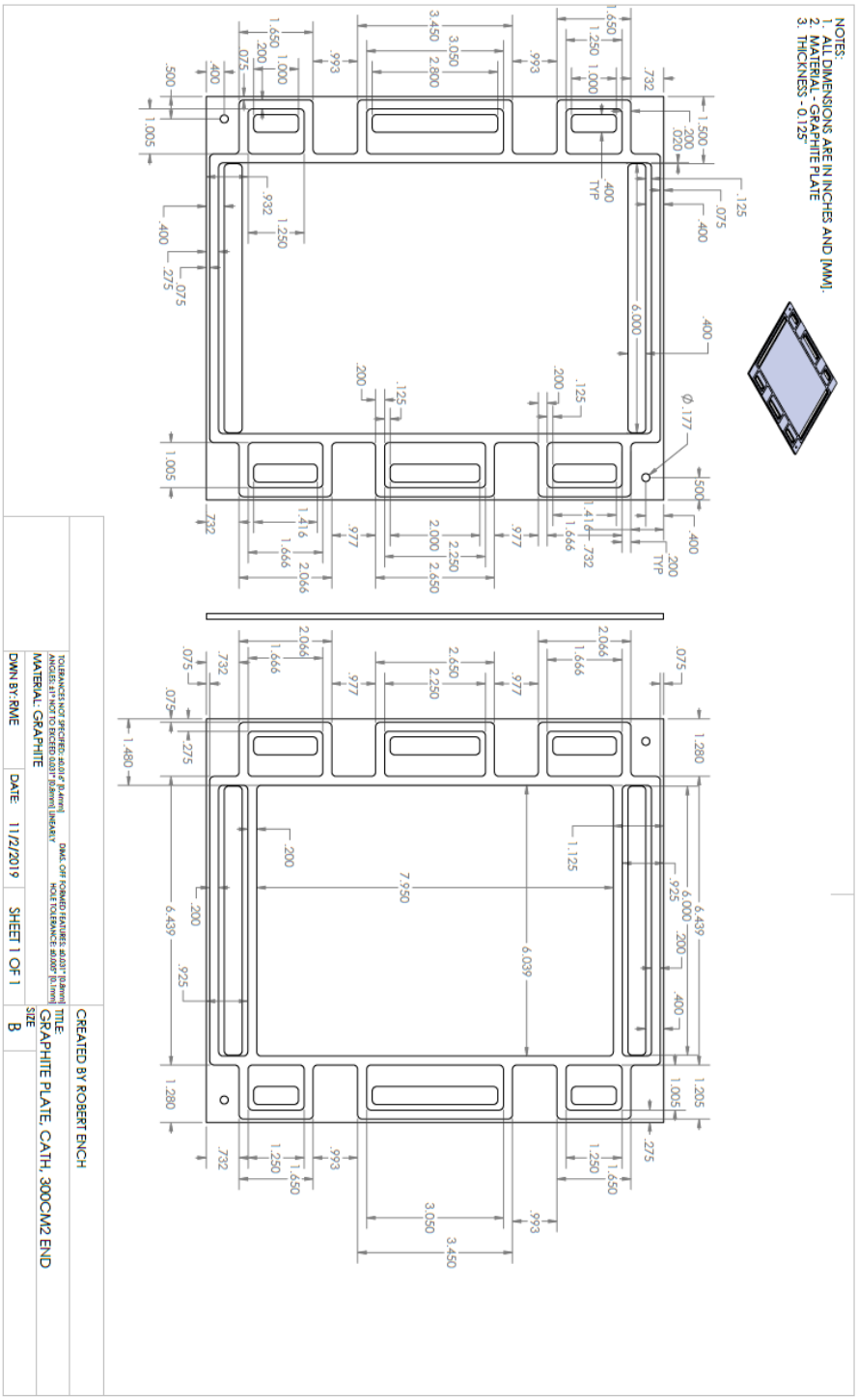

Figure 79 Graphite end plate drawing

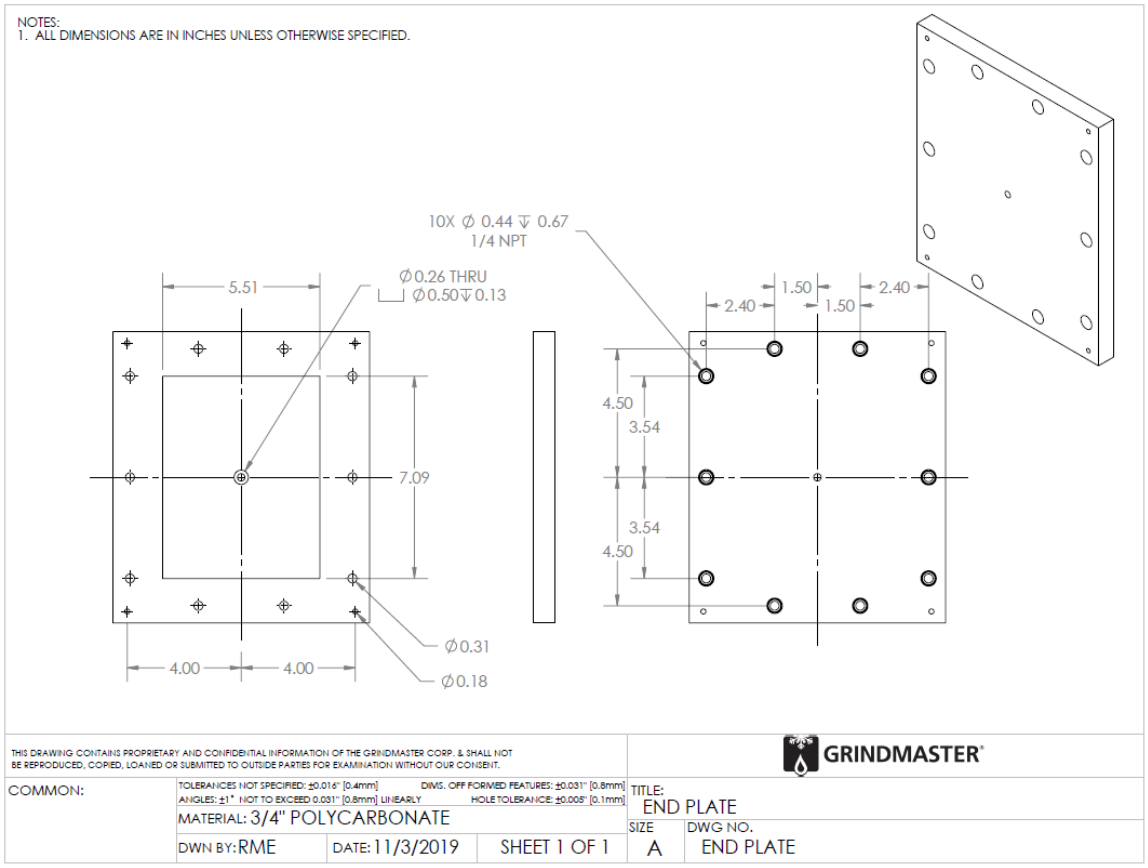

Figure 80 End plate drawing

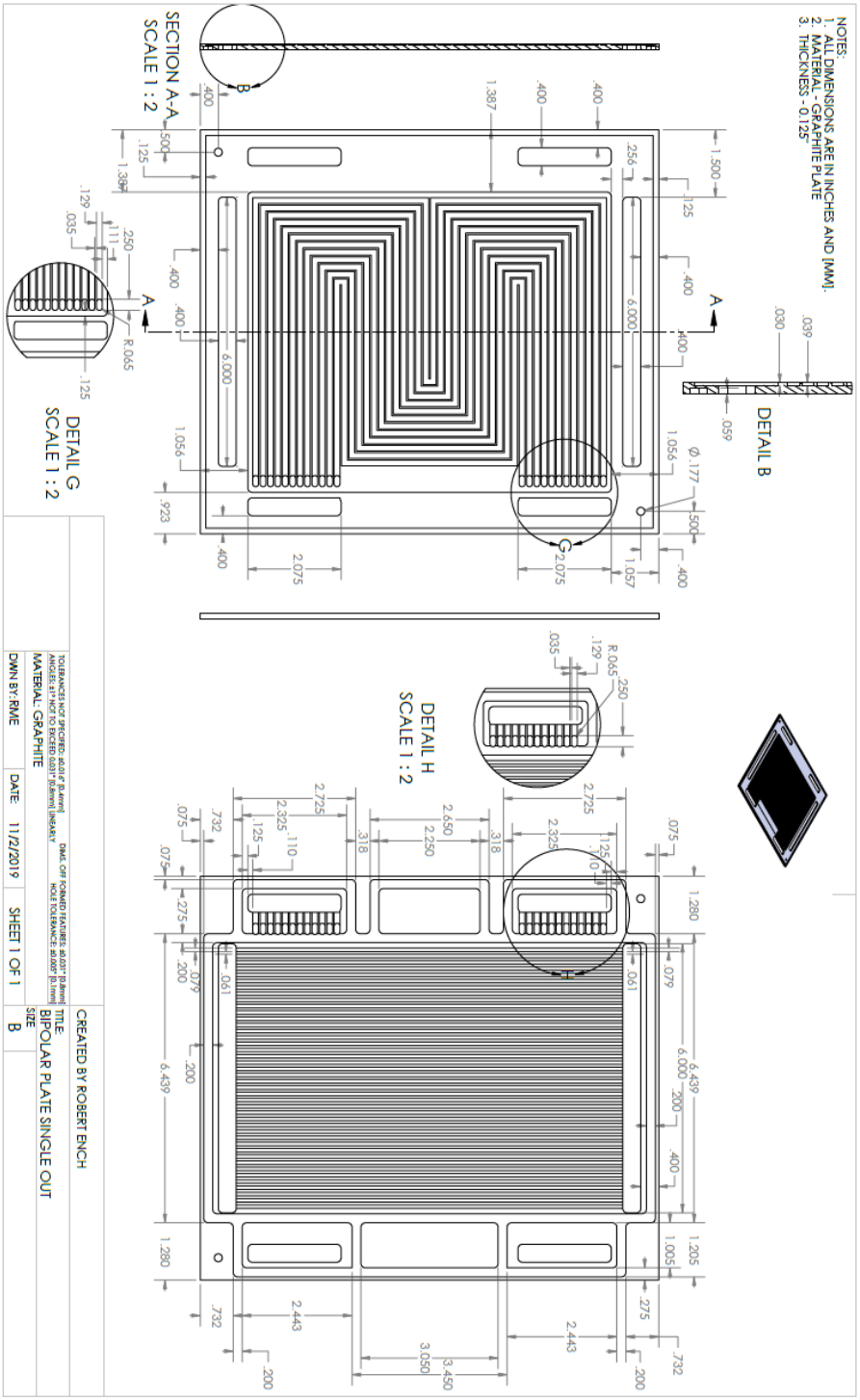

Figure 81 Single out bipolar plate drawing

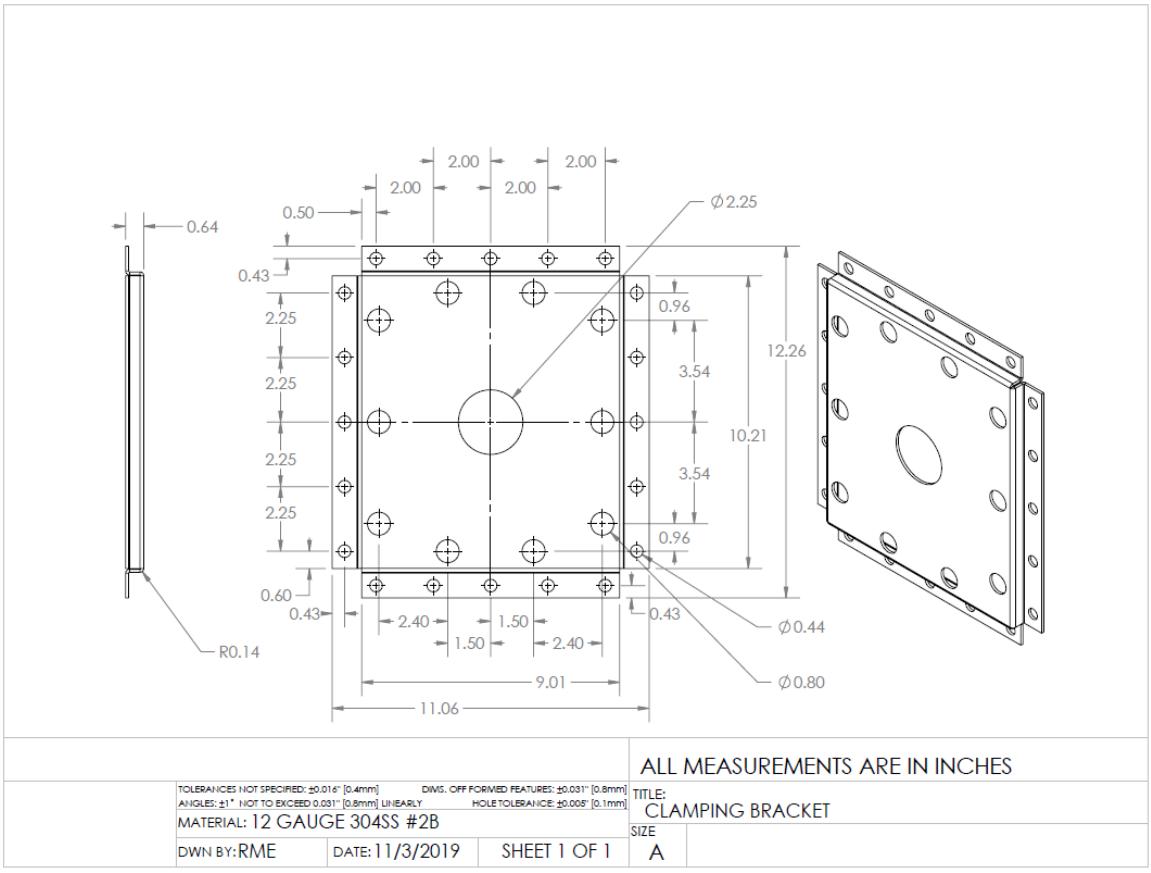

Figure 82 Clamping Bracket drawing

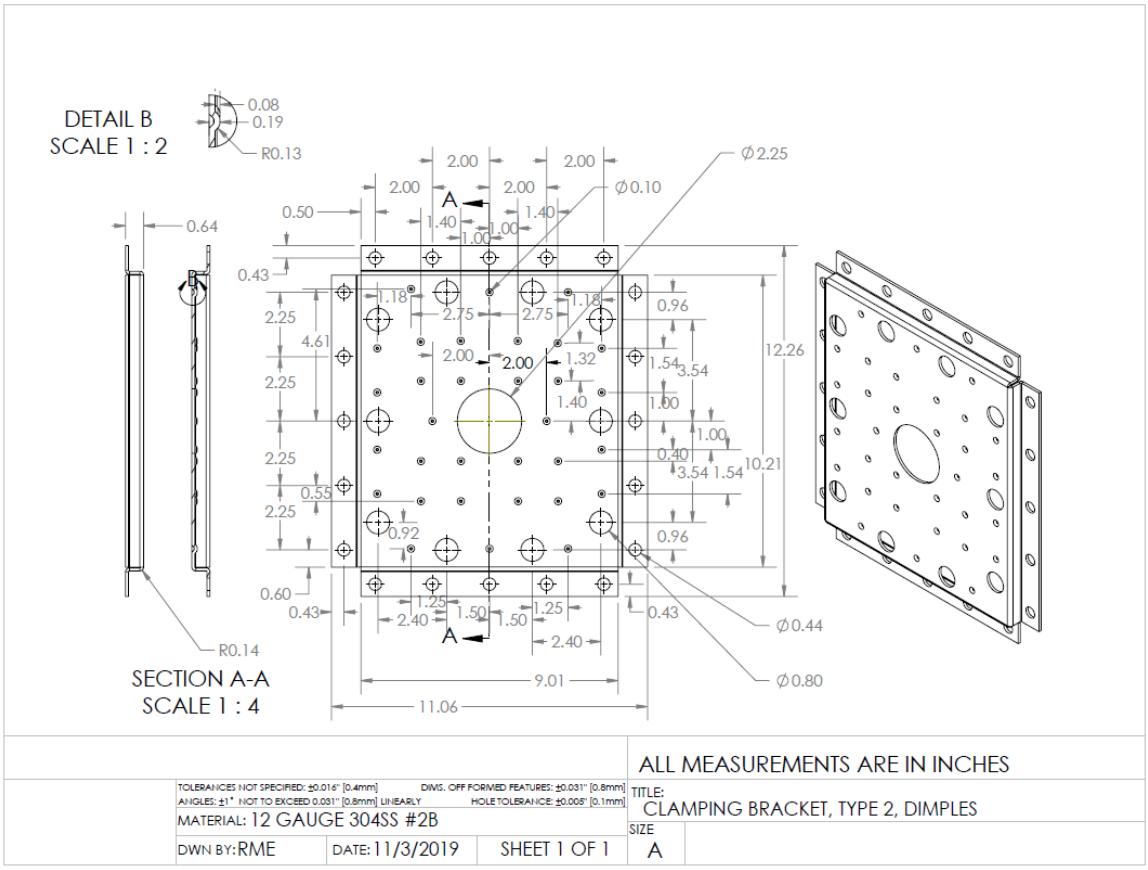

Figure 83 Clamping bracket with dimples drawing

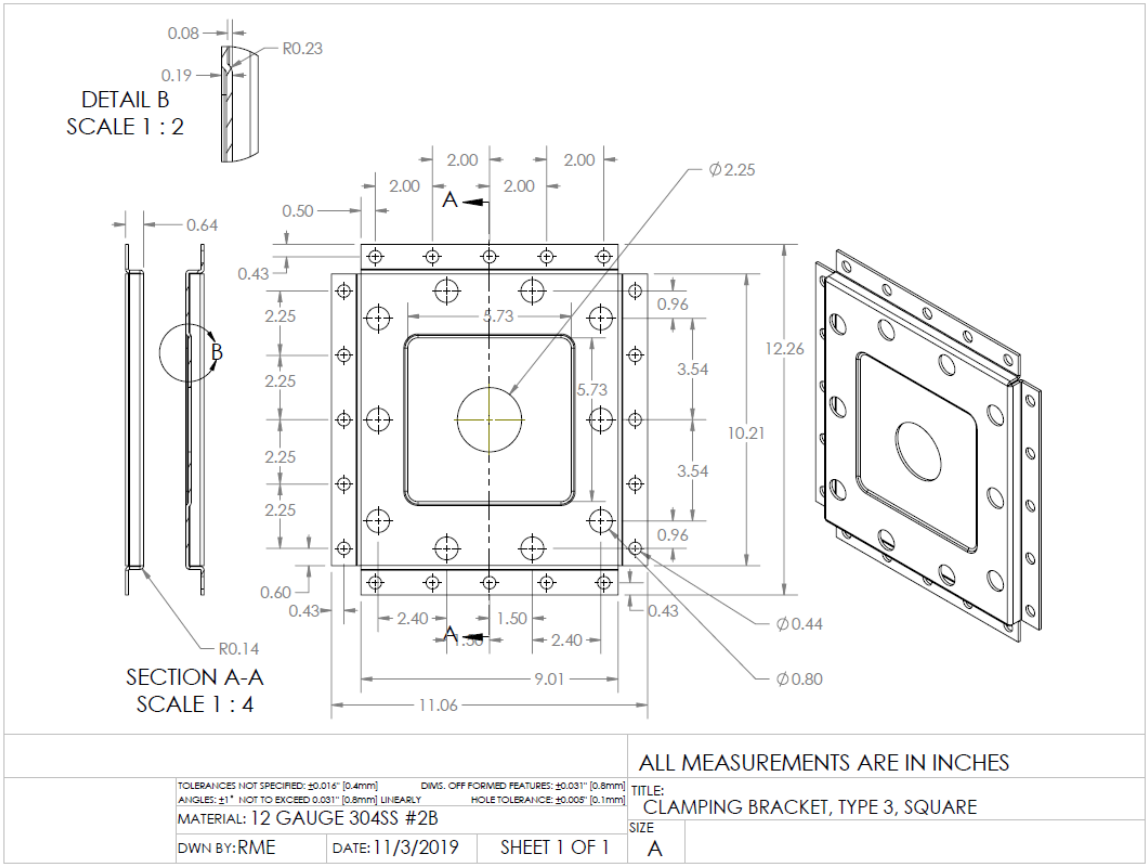

Figure 84 Clamping bracket with square emboss drawing

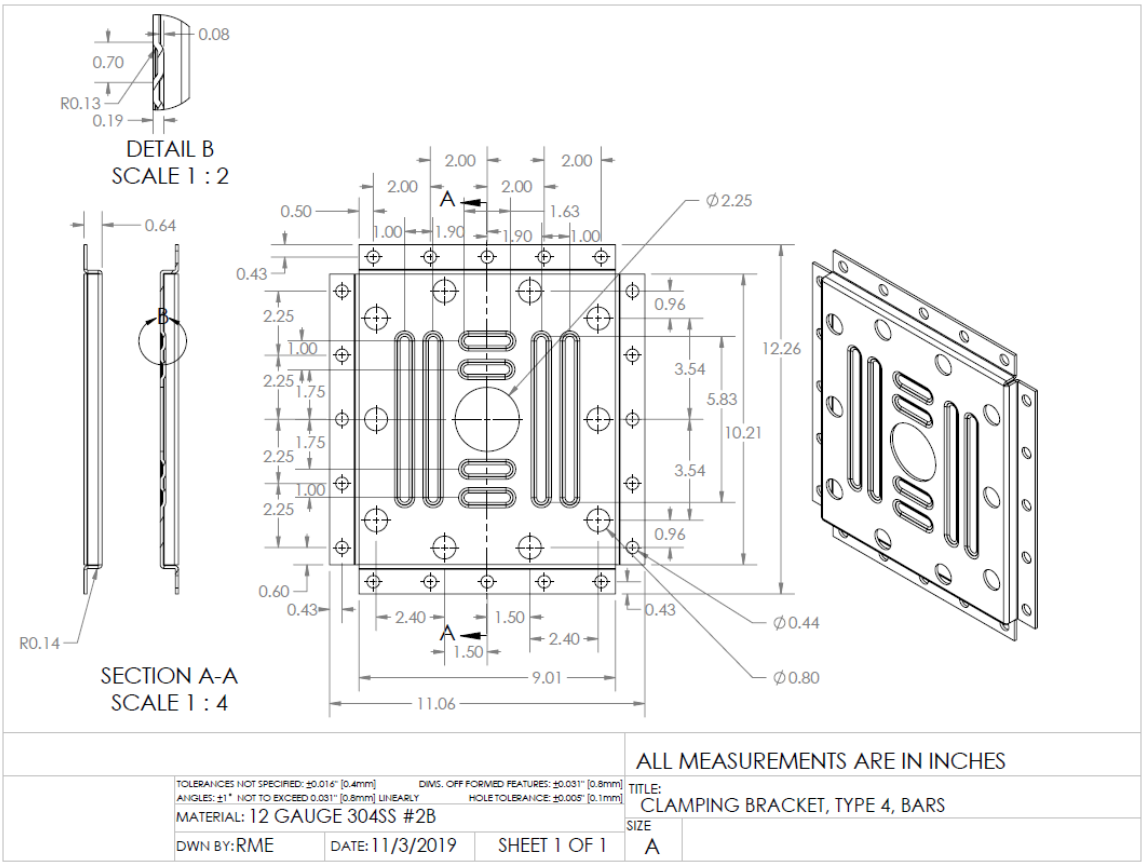

Figure 85 Clamping bracket with bar style emboss drawing

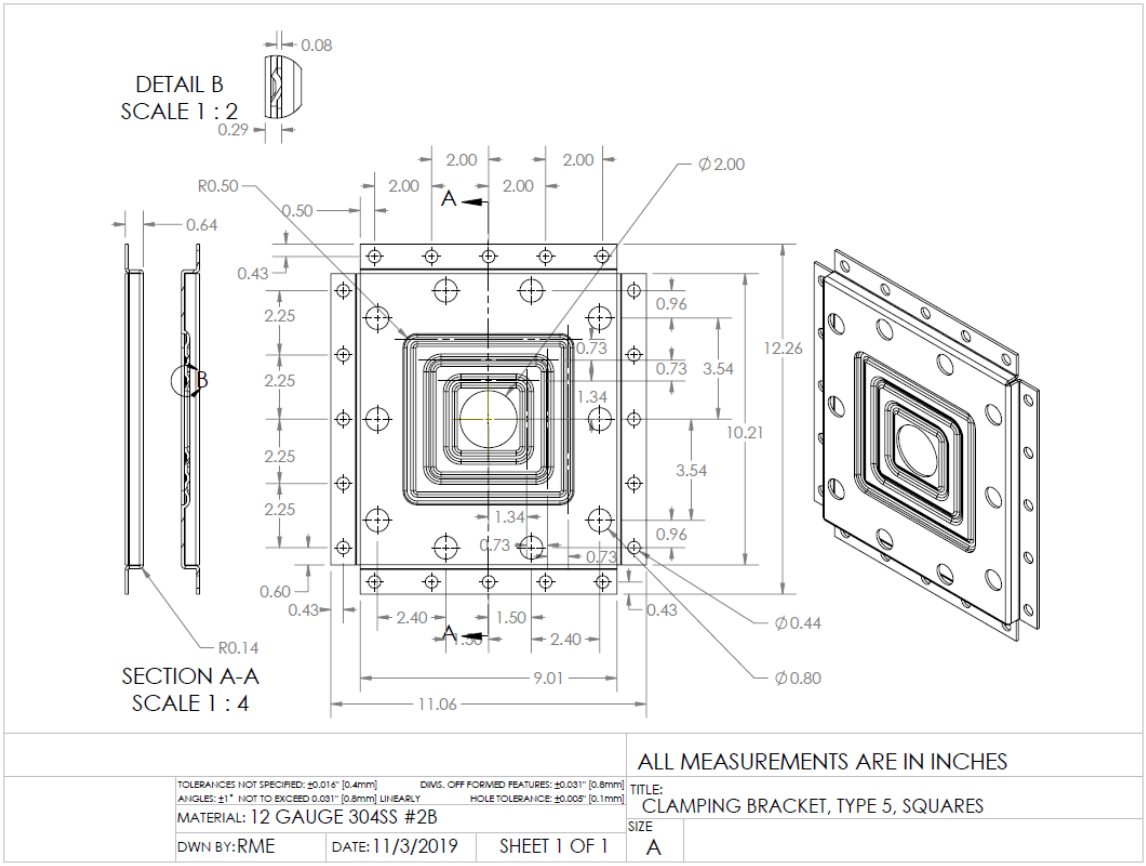

Figure 86 Clamping bracket with layered squares emboss drawing

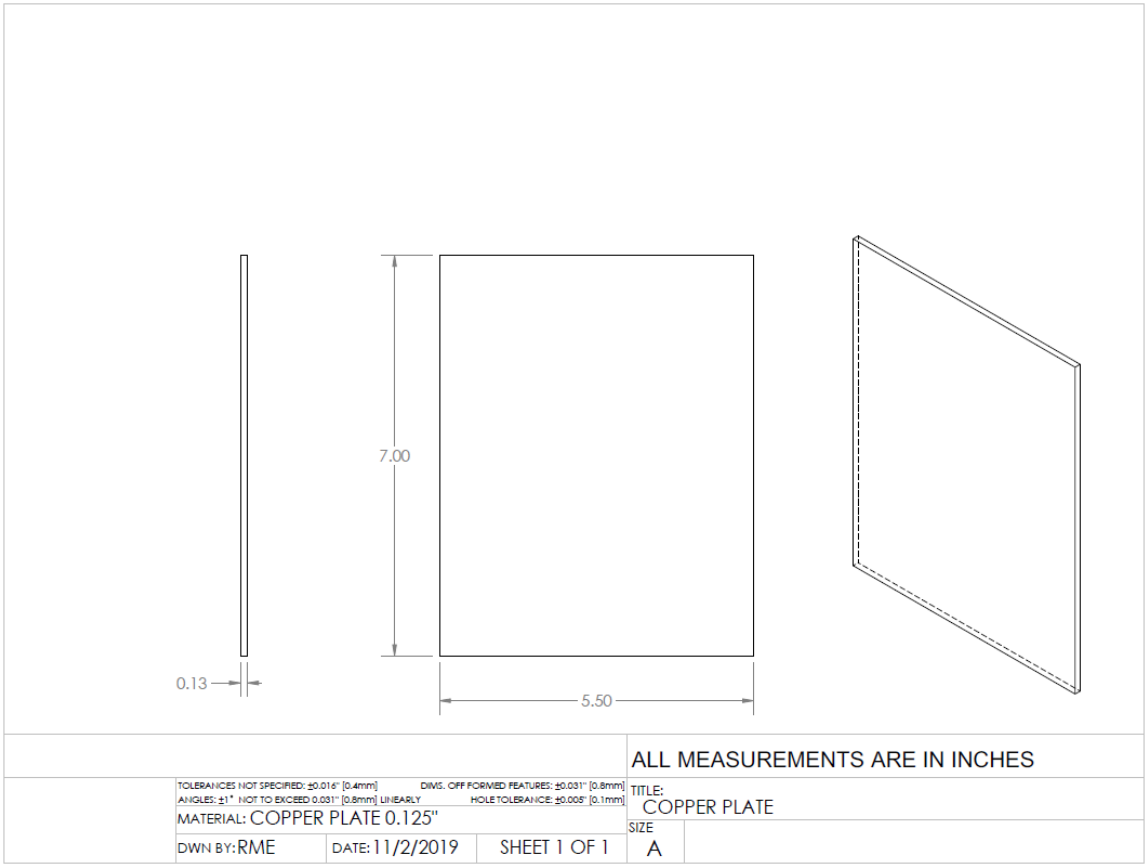

Figure 87 Copper plate drawing

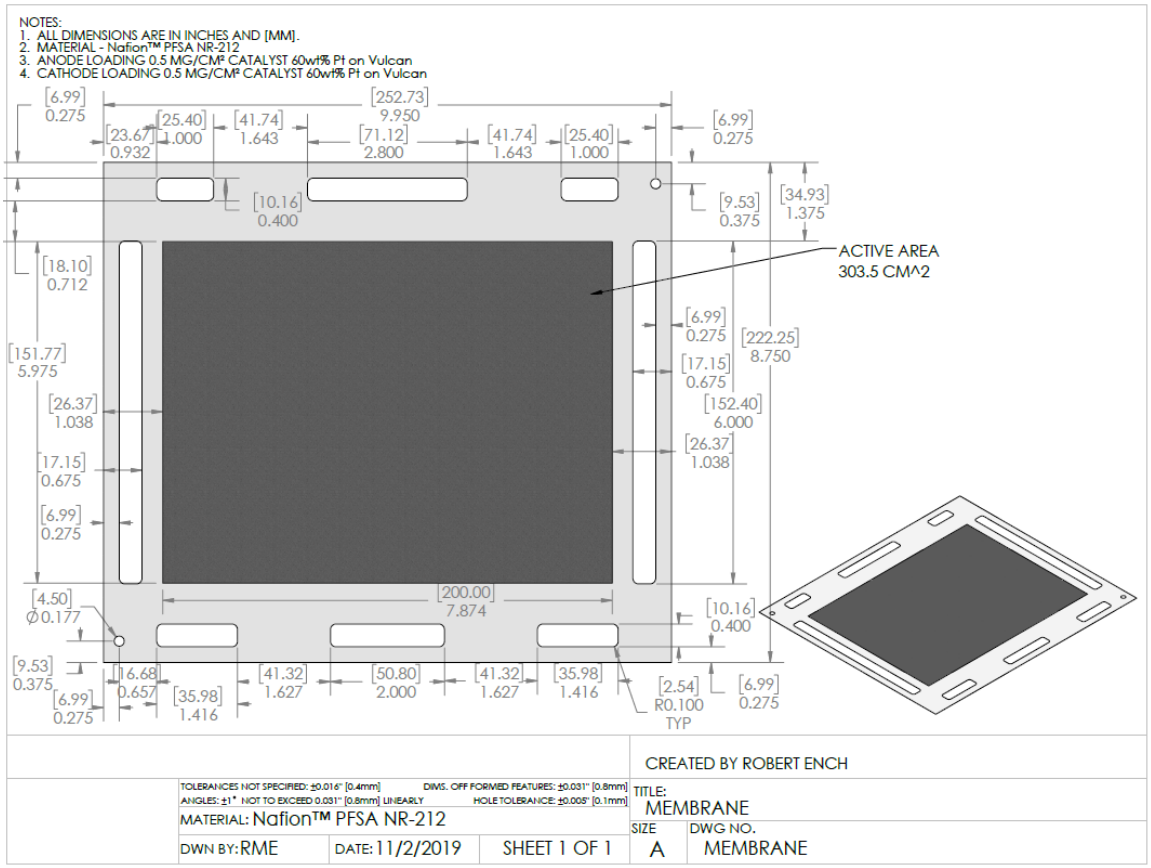

Figure 88 Membrane Drawing

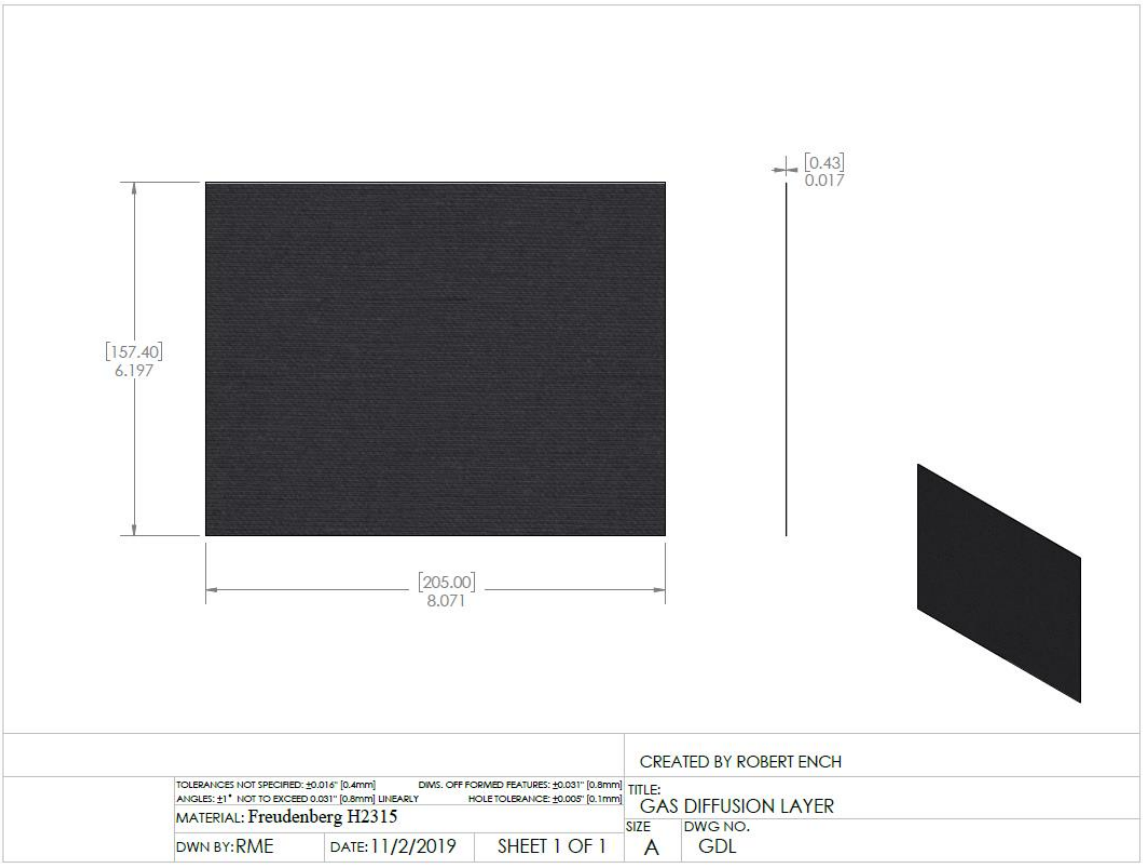

Figure 89 GDL drawing

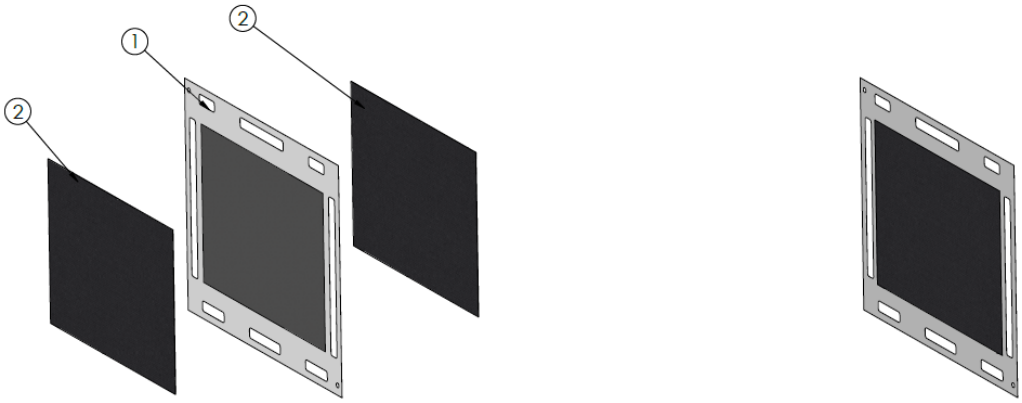

ITEM NO.	PART NUMBER	DESCRIPTION	QTY.
1	MEMBRANE	MEMBRANE	1
2	GDL	GAS DIFFUSION LAYER	2

CREATED BY ROBERT ENCH

TOLERANCES NOT SPECIFIED: ±0.016" [0.4mm] DIMS. OFF FORMED FEATURES: ±0.031" [0.8mm]
ANGLES: ±1° NOT TO EXCEED 0.031" [0.8mm] LINEARLY HOLE TOLERANCE: ±0.005" [0.1mm]

MATERIAL: NOTED

TITLE: MEA

DWN BY: RME | DATE: 11/2/2019 | SHEET 1 OF 1

SIZE A | DWG NO. MEA

Figure 90 MEA drawing

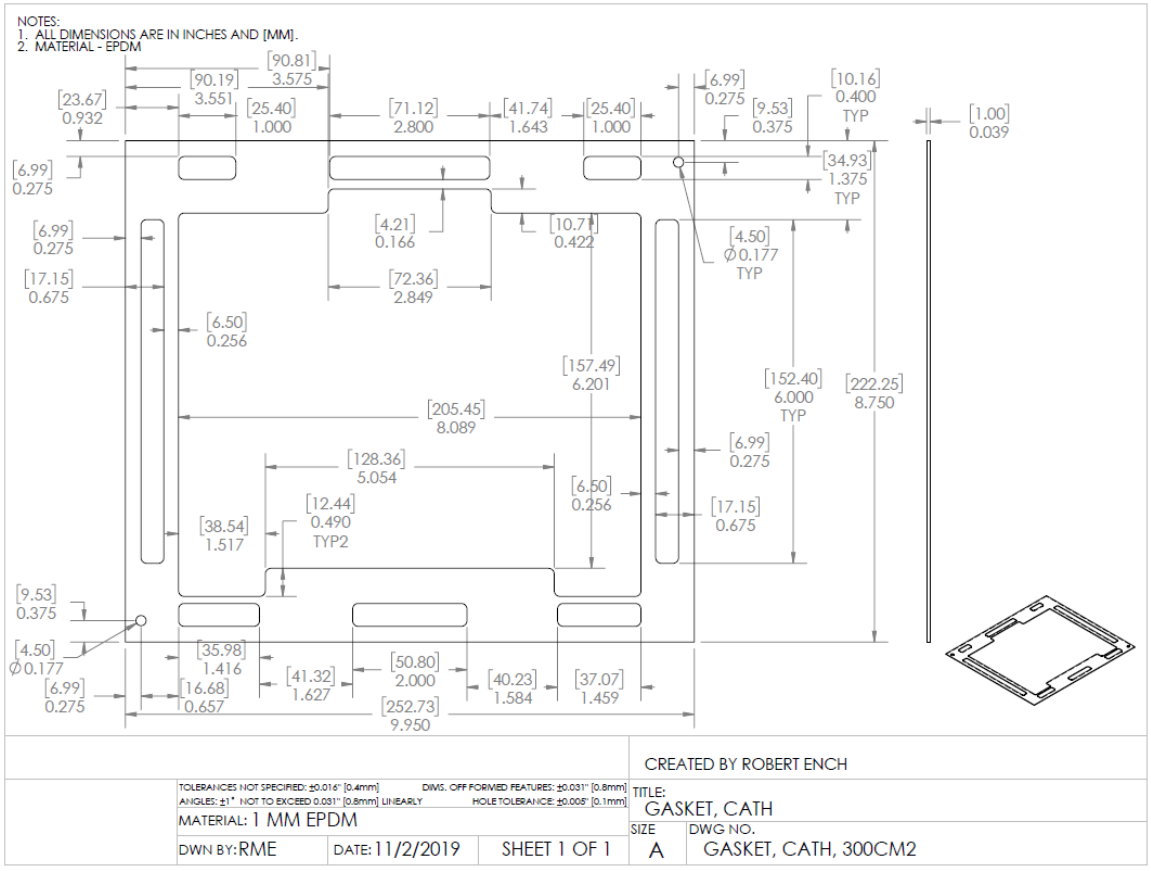

Figure 91 Cathode side gasket drawing

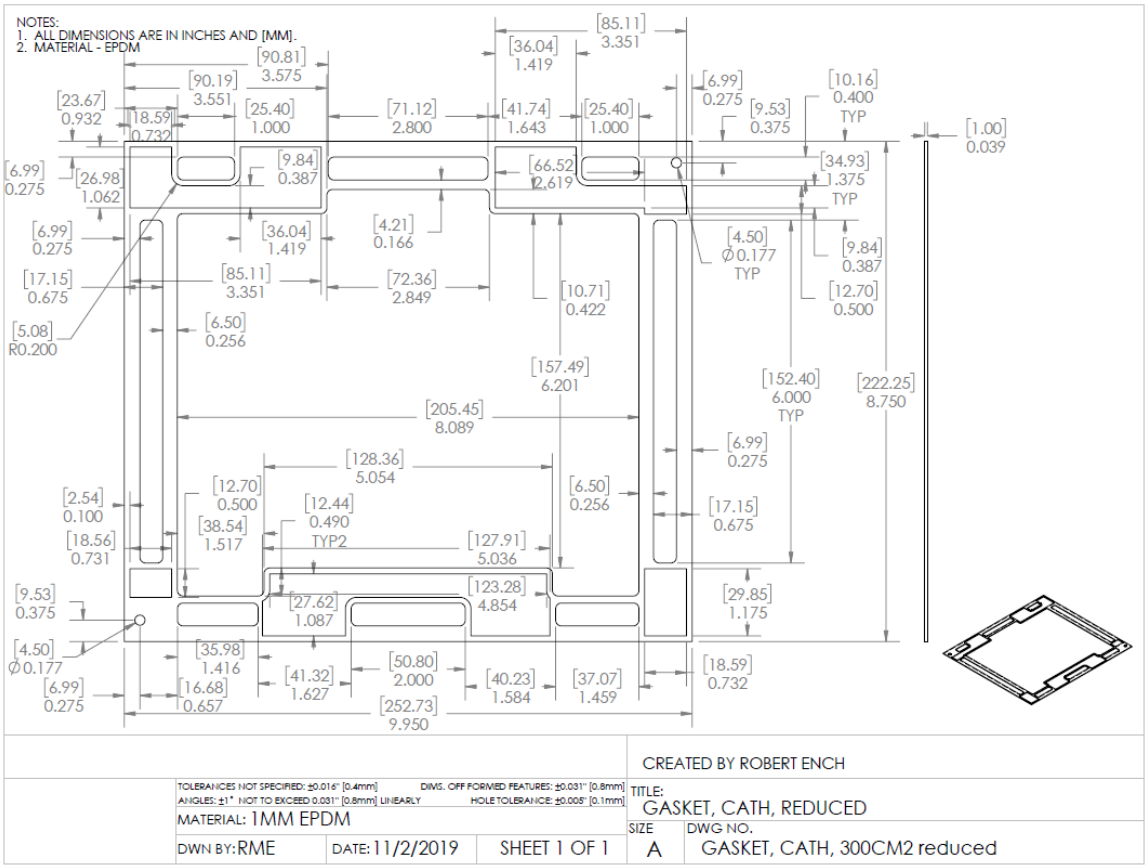

Figure 92 Cathode side gasket with reduced material drawing

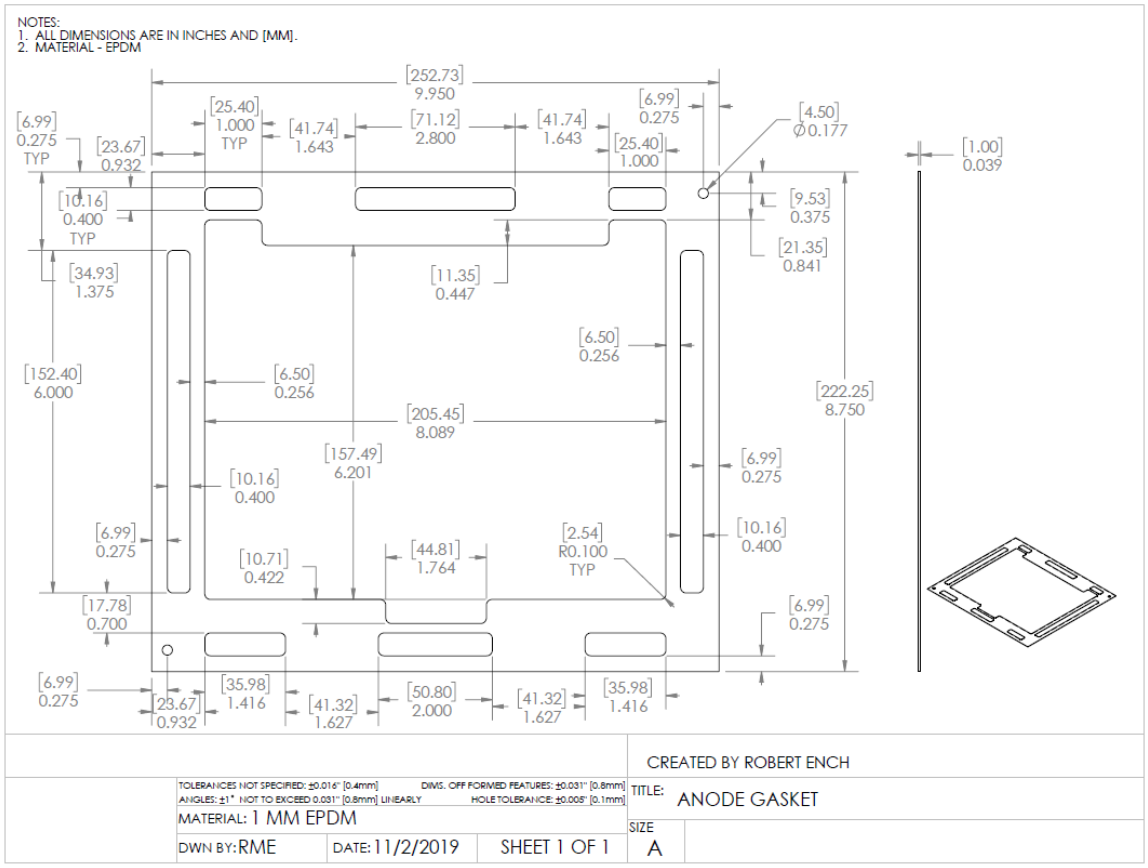

Figure 93 Anode side gasket drawing

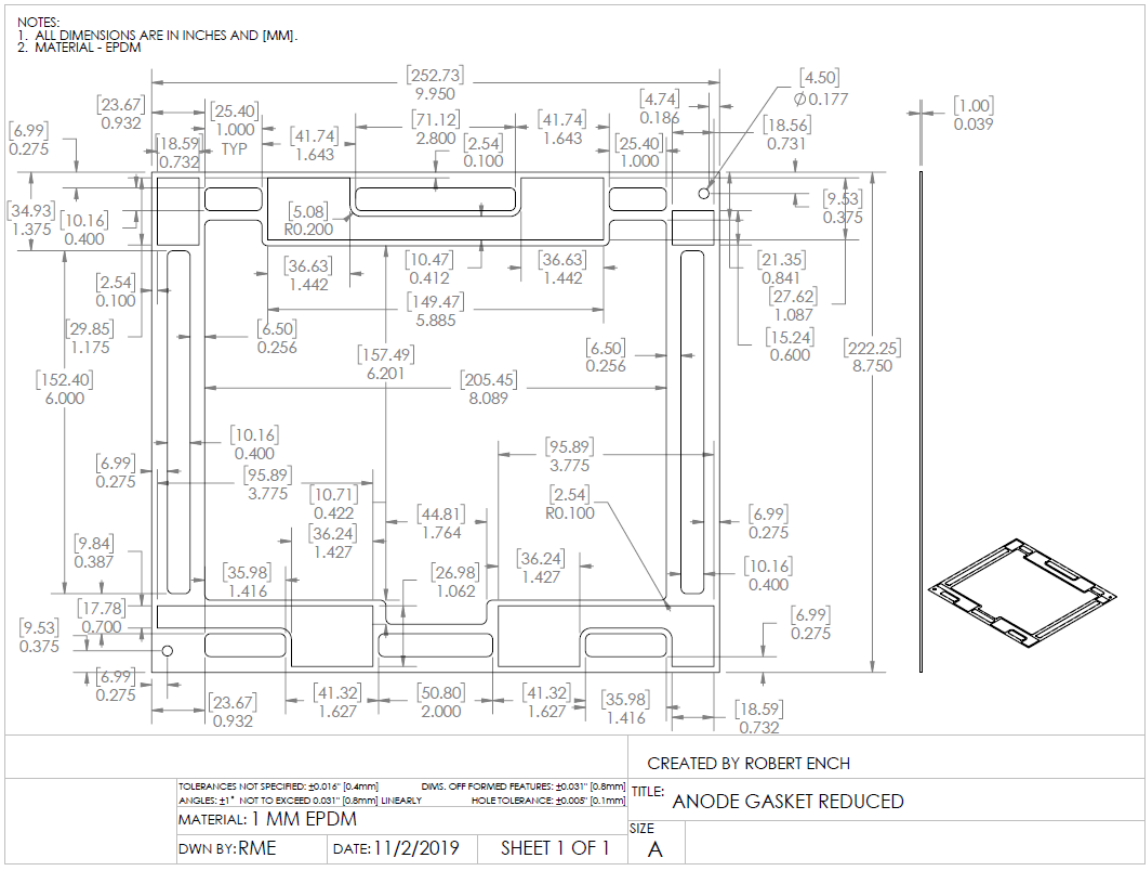

Figure 94 Anode side gasket with material removed drawing

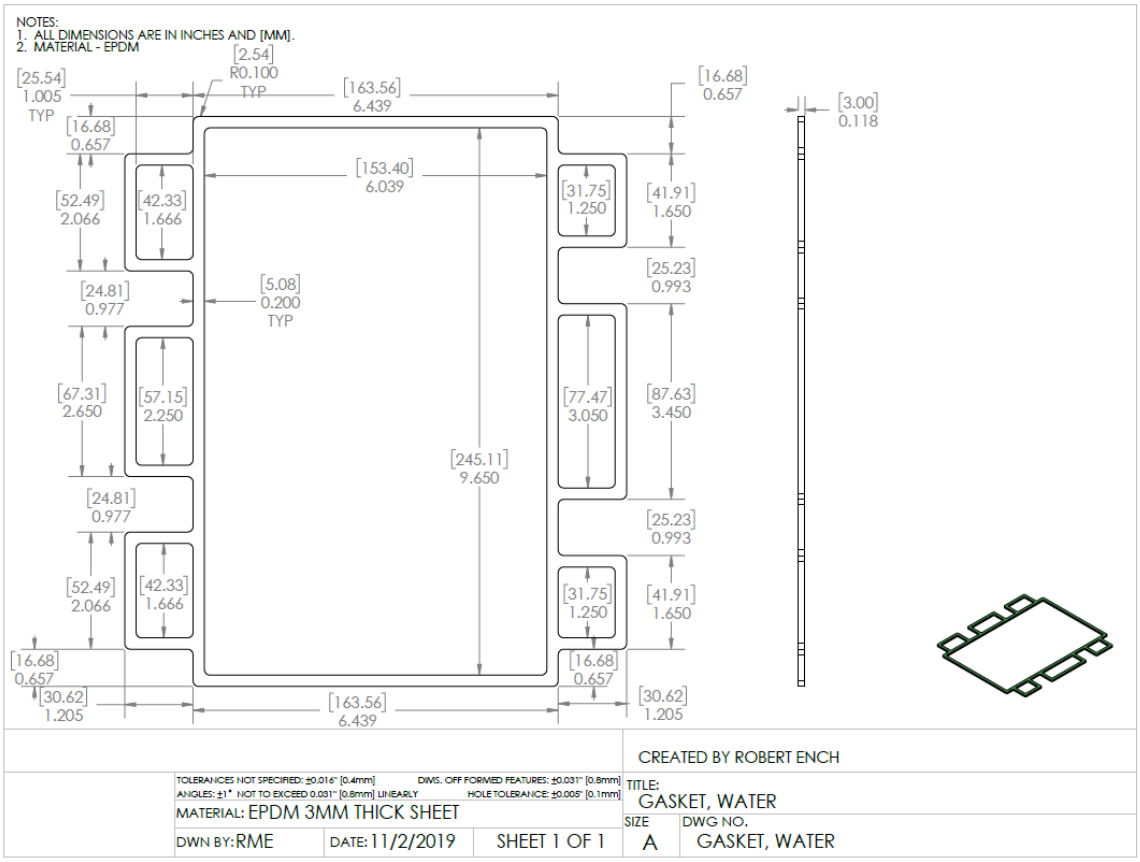

Figure 95 Water cooling side gasket drawing

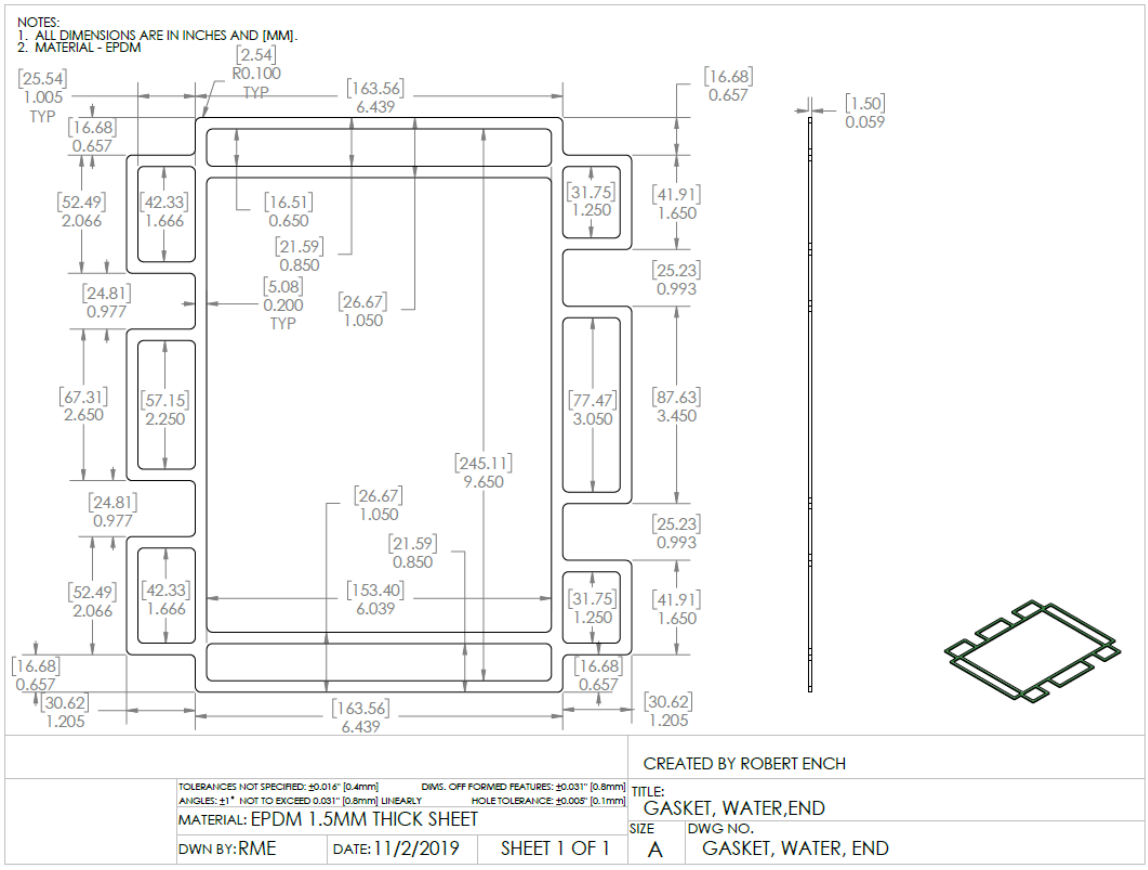

Figure 96 End plate water gasket drawing

CURRICULUM VITA

Name: Robert Michael Ench

ADDRESS: 10414 Whipps Mill Rd
Louisville, KY 40223

DOB: Raleigh, North Carolina – September 2, 1977

EDUCATION
& TRAINING: Bachelor's Degree, Mechanical Engineering
University of Louisville
2013

Master of Engineering in Engineering Management
University of Louisville
2018

AWARDS: Mechanical Engineering Department Academic Achievement Award
April 2011

Mechanical Engineering Department Academic Achievement Award
April 2012

ORGANIZATIONS: Golden Key International Honor Society
2012-Present

Pi Tau Sigma Honor Society
2012-Present

PUBLICATION

A Novel Lightweight Polymer Electrolyte Fuel Cell Stack for Robot Systems